Dynamics of Discrete Irregular Cosmological Models

Shan Williams Jolin

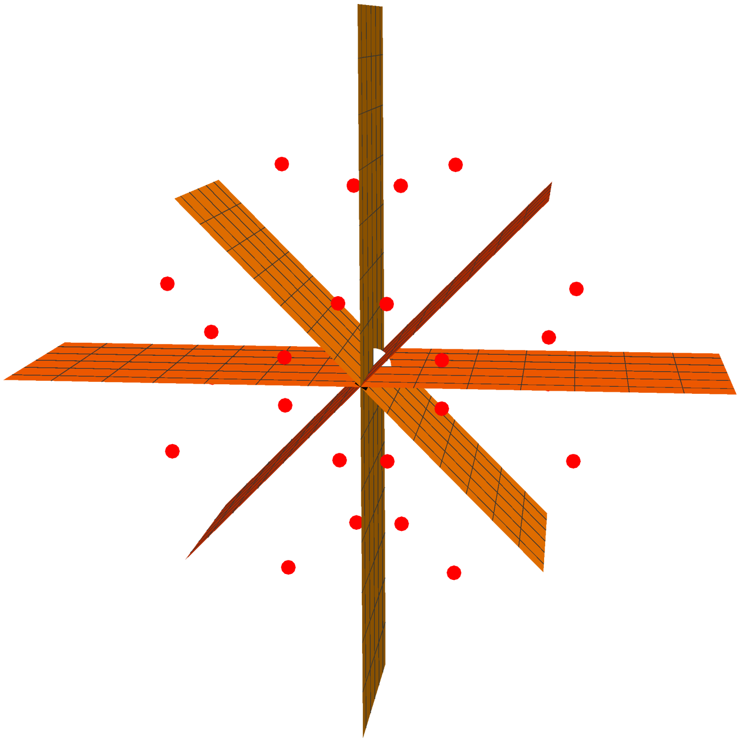

Fysikum - Department of Physics
Degree 60 HE credits
Theoretical Physics
Master's Programme in Theoretical Physics (120 credits)
Autumn 2014
Supervisor: Kjell Rosquist

Stockholms
universitet

Abstract

This thesis investigates the dynamics of a set of 8-600 Schwarzschild masses, randomly distributed inside cells which tessellate a 3-sphere. Furthermore the contents of each cell are mirror images of its neighbor. This symmetry give rise to a locally rotationally symmetric (LRS) curve, along which the Einstein field equations governing dynamics can be exactly integrated. The result is an irregular model consisting of discrete matter content, but where the dynamics is easy to calculate. We see that these local inhomogeneities will cause behavior deviating from the spherical dust-filled FLRW model. For instance, there are cases where configurations exhibit acceleration along the LRS curve, even though the content consists solely of ordinary matter with a vacuum filled exterior and no cosmological constant.

Sammanfattning

Denna avhandling undersöker konfigurationer av 8-600 Schwarzschild-massor, som är slumpmässigt utplacerade inom celler som tessellerar en 3-sfär. Utöver det är även innehållet i varje cell en spegelbild av granncellen. Denna symmetri ger upphov till en lokalt rotationssymmetrisk (LRS) kurva där Einsteins fältekvationer som beskriver dynamiken längs med är exakt integrerbara. Resultatet är en oregelbunden modell som består av diskreta massor, men vars dynamik är enkel att beräkna. Vi ser att dessa lokala inhomogeniteter ger upphov till beteenden som avviker från den sfäriska partikel-fyllda FLRW-modellen. Till exempel uppstår konfigurationer som uppvisar acceleration längs med LRS-kurvan, trots att innehållet består endast av ordinära massor med vakuum utanför och ingen kosmologisk konstant.

Contents

Chapter 1

Introduction

Cosmology is the study of the nature, origin and evolution of the universe [1]. This is a daunting task, as one can well realize by simply looking at the sky a starry night; numerous stars which agglomerate into clusters of stars, galaxies and then finally clusters of galaxies. These structures range in size from ~ 0.307 pc[1] up to ~ 9.20 Mpc [2]. The substantial amount of structures and their rich variety provide computational difficulties for any theory aiming to completely describe their gravitational interactions - the universe is too complicated. Unfortunately, for the most successful theory of gravitation, *viz.* the theory of general relativity, this becomes notoriously difficult due to the absence of any superposition principle as in electromagnetism or Newtonian theory of gravitation. Therefore to perform cosmological studies efficiently, appropriate approximations must be made. Instead of using a "bottom-up" approach, where studies of a system's properties starts with the individual components and their immediate surroundings, a "top-down" approach is adopted in cosmology.

The basis for the "top-down" approach is to start with a large-scale approximation and treat small-scale structures, or *inhomogeneities*, as perturbations on the large-scale background. Astronomical observations indicate that the universe is homogeneous and isotropic on scales of ~ 30.7 Mpc. The evidence for this comes from several sources, such as the isotropy measured in the cosmic microwave radiation and the isotropy in the distribution of radio sources. Consequentially, taking a volume of the universe centered on Earth with a side of the order of 30.7 Mpc will not look much different than any other volume centered elsewhere [2]. Therefore one assumes that the geometry of the universe is homogenous and isotropic. This is known as the *cosmological principle* [1]. This implies that any model successfully describing our neighborhood (on large enough scales where homogeneity and isotropy exists) should also work elsewhere in the universe.

Furthermore in the "top-down" approach clusters of galaxies and other large structures are treated as "particles" without any internal structure, such as stars and solar systems. These "particles" fill the universe and to simplify calculations further, are averaged as a *perfect fluid*. This fluid lacks any self-interaction and its energy density is the same everywhere in the universe. In addition, for such a fluid, there exists a co-moving frame where this fluid looks perfectly isotropic [2, 4].

Cosmological issues have been pondered at least since Ancient Greece; early commentators

---

[1] The unit *parsec* (or pc) measures distance and equals 3.2616 light years.

include Plato and Aristotle. However cosmology remained very speculative until the advent of telescopes in the 17th century when simple observations could be conducted. Although it would take until the 1920s until a more realistic cosmological worldview would emerge which we are familiar with today. Starting with Edwin Hubble's discovery of an expanding universe, the standard model of cosmology known as the *Hot Big Bang model* developed [1, 2].

The Hot Big Bang model is also known as the standard model of cosmology, a title hinting at the model's success in describing several cosmological phenomena. The Hot Big Bang model states that the universe began in a state of rapid expansion from a very nearly homogeneous, isotropic condition of very high density and temperature. Initially the universe was hot and dense; the content was dominated by high energy photons and relativistic particles. As the universe cooled and expanded, matter started to form and the universe's content became matter dominated instead. See [2, 4, 5] and references therein for details.

The geometry of the Hot Big Bang model is provided by the *Friedmann-Lemaître-Robertson-Walker model* (abbreviated FLRW model). Here the energy content of the universe is approximated by a perfect fluid and is composed of (in any combination) radiation, matter and/or vacuum energy. The FLRW model also obeys the cosmological principle. Furthermore the model permits accelerating expanding universes provided that the vacuum energy plays an important role [4].

The FLRW model has been very successful in providing a mathematical framework for the Hot Big Bang model. However currently the FLRW model requires unknown types of matter and energy *viz.* dark matter and dark energy, both of which have not been observed by terrestrial laboratories to date even though estimations suggest dark matter and dark energy are abundant [1, 4, 5]. This has therefore called for a more thorough investigation of how small-scale inhomogeneities affect the large-scale geometry, i.e. a "bottom-up" approach. However due to the absence of a superposition principle in general relativity, solving many-body problems is difficult.

A famous attempt was made by Lindquist and Wheeler [3]. In their paper, a spacelike hypersurface with the topology of a *3-sphere*[2] was tessellated into regular cells. Inside the center of each cell, identical Schwarzschild black holes were located. Everywhere else exterior to the black holes was vacuum. The dynamics at the boundary of each cell was then easily analyzed provided the approximation that each cell was spherical. This method was well known before in solid-state physics as the *Wigner-Seitz approximation.*

Lindquist and Wheeler's seminal paper has been well studied by others, whereas two are important for this thesis which is due to Clifton, Rosquist and Tavakol [6], as well due to Engström [7]. These authors took an exactly solvable approach to Lindquist and Wheeler's model by investigating similar, but static, models. Their conclusion was that the FLRW model was approached as the number of discrete Schwarzschild black holes increased (up to 600). However their dynamics were not investigated.

The dynamics of these exact models were investigated later; by Bentivegna and Korzyński [8], as well by Clifton et. al. [9]. In the former work, similarly constructed models were evolved using numerical methods while in the latter work the models were evolved using exact methods. The work of [9] will be the starting point for this thesis.

In this thesis, a topological 3-sphere is tessellated into eight cells of equal size and dimension. Inside one cell several Schwarzschild black holes (also referred to as *Schwarzschild masses*

---

[2] The 3-sphere is the set of all points (x_1, x_2, x_3, x_4) such that $x_1^2 + x_2^2 + x_3^2 + x_4^2 = r^2$, where r is the radius of the sphere. It is the 4-dimensional analogy of the regular sphere found in 3-dimensions.

or *sources*) are distributed irregularly and randomly. Everywhere exterior to these masses is vacuum and the cosmological constant is set to zero. Thereafter the remaining cells, which are empty, are filled with Schwarzschild masses in such a way that every cell is a mirror image of its neighbors. This will result in an overall configuration which is locally irregular, but contain discrete rotational symmetries around certain curves. These curves are referred to as locally rotationally symmetric curves or LRS curves. Assuming the 3-sphere is initially instantaneously static, the dynamics of the model can then be solved for exactly along the LRS curves by using the tools developed in [9]. We will see that this model initially shows similarities to the FLRW model, particularly for many sources, however when dynamics are considered significant deviations from the FLRW model start to arise.

The thesis is divided up as follows: the next chapter introduces fundamental concepts and ideas which will facilitate future discussions and analysis in this thesis. This is followed by a presentation of the equations governing the dynamics of the model and their following simplification upon imposing certain symmetry constraints. The ensuing chapter then explains how these symmetry constraints are introduced into the model, while the final part contains measurements of the initial state and time-dependent quantities as a function of time.

Chapter 2

Fundamentals

This chapter introduces notions and concepts which are important in order to grasp the fundamentals in the subsequent discussions. For further details I refer the interested readers to the references cited herein. The first section is more involved and focuses on the choice of coordinate system and how it leads up to the 3+1 splitting of the equations. The second section introduces some useful concepts from the field of conformal geometry. The final section introduces the Weyl tensor; since the gravito-electric and gravito-magnetic tensors which stem from the Weyl tensor are very important for the dynamics of my models.

2.1 Constructing an Appropriate Reference System

Throughout this work the following sign convention on the metric is employed (- + + +). Moreover the following index convention is used: spacetime coordinate indices are taken to run over the second half of the Greek alphabet(μ, ν, $\rho ... = 0 - 3$), while spatial coordinates are taken to run over the second half of the Latin alphabet (i, j, $k ... = 1 - 3$). Orthonormal frame indices are taken over the first half of the Latin alphabet (a, b, $c ... = 0 - 3$), while their spatial counterparts will run over the first half of the Greek alphabet (α, β, $\gamma ... = 1 - 3$).

2.1.1 Synchronous Coordinate Systems

Suppose we have a hypersurface (a three-dimensional "surface") $\mathscr{B}_I$ embedded in spacetime. This hypersurface is chosen in such a manner that all normals to this hypersurface (to any event lying on it), have a timelike direction. We then say that such a hypersurface is spacelike, since all intervals on such a hypersurface will be spacelike. Furthermore a grid (in any manner) is placed on this hypersurface, labeling all events on the hypersurface with the spatial coordinates (x^1, x^2, x^3). In addition, all events on the same hypersurface are assigned the same time coordinate $x^0 = t_I$. Then if we allow the spatial coordinates to be "propagated" off the hypersurface $\mathscr{B}_I$ throughout spacetime by means of the world lines of each event on $\mathscr{B}_I$ (alternatively, the spatial coordinates are "lifted" off the hypersurface in the direction of the timelike normals), the spatial coordinates become merely labels for the world lines. This setup allows for the following: whenever only spatial coordinates are provided, the *world line of one event* is singled out. However this single world line contains all information regarding that one event throughout its entire history and future. If we only want to know what happens at a certain time along this

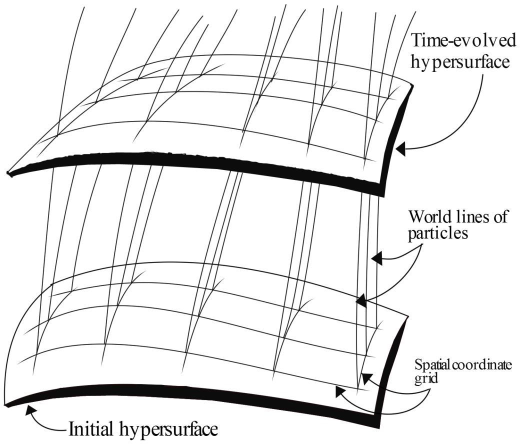

Figure 2.1: Schematic diagram for how the synchronous coordinate could look like. The grid on the surfaces indicate the spatial coordinates, while the vertical world lines are time like and their lengths provide the time coordinate.

world line, the time coordinate needs to be specified. Conversely, if we initially only provided the time coordinate instead, then *one hypersurface* will be singled out, which contains all events occurring at the specified time, with their respective world lines "piercing" orthogonally through the hypersurface. To find a particular event at the specified time, the spatial coordinates need to be specified. This will single out one event on the already chosen hypersurface. To summarize, we have "sliced up" spacetime into several hypersurfaces, where each hypersurface is labeled by the time coordinate t, and all world lines permeating spacetime are labeled by $(x^1, x^2, x^3,)$. These world lines are all timelike and normal to the hypersurfaces, in addition they are also geodesics. Furthermore any interval on the hypersurface is spacelike. Such a coordinate system is known as *synchronous*. Another name is *Gaussian normal coordinate system* [2, 10].

The synchronous coordinate system is synchronous in the sense that every observer on the same hypersurface will have synchronous clocks. To find the time coordinate for an event P on another hypersurface $\mathscr{B}_F$, simply use [2]

$$t(P) = t_I + \left(\int_{\mathscr{B}_I}^{\mathscr{B}_F} d\tau \right)_{\text{along world line of } P} \tag{2.1}$$

Since time is constant across the hypersurface and spatial coordinates are constant along world lines, the basis vector $\partial/\partial t$ must be tangent to the world lines and orthogonal to the hypersurface. Consequently, this guarantees [2]

$$(\partial/\partial t) \cdot (\partial/\partial x^i) = 0 \text{ for } i = 1, 2, 3. \tag{2.2}$$

Therefore a 4-velocity u^μ with the properties [10]

$$u^\mu = d\mathrm{x}^\mu / d\tau \tag{2.3}$$

$$u_\mu u^\mu = -1 \tag{2.4}$$

will be parallel to the world line x^1, x^2, $x^3 = const.$ and have the components $u^0 = 1$, $u^i = 0$. Furthermore, the 4-velocity will also automatically satisfy the geodesic equation. u^μ can be considered the 4-velocity with which the hypersurface travels through spacetime.

Then constructing a metric $g_{\mu\nu} = (\partial/\partial x^\mu) \cdot (\partial/\partial x^\nu)$ and the resulting line element will have the form

$$ds^2 = -(dx^0)^2 + h_{ij} dx^i dx^j. \tag{2.5}$$

Any coordinate system with a line element of this form is said to be synchronous. The tensor h_{ij} is the metric intrinsic to the hypersurface [2, 10]. Notice that the relationship between the determinants, h and g, of each tensor is simply $g = -h$.

An important point to make is that in order for a vector or tensor to be physically measurable, it must lie on the hypersurface. That is because measurements of events are performed not in the event's past or future, but in its present. Therefore the observer and event must lie on the same hypersurface. Such a vector or tensor is then considered *spatial* in this work. This implies that the tensor (or vector) is orthogonal to the 4-velocity u^μ. An important example is the hypersurface metric h_{ij} which is spatial. Furthermore, indices manipulation and covariant derivation of spatial vectors and tensors can be done by using the metric h_{ij} instead of g_{ij}.

Suppose now that we take the partial time derivative of the hypersurface metric h_{ij} and introduce the notation [10]:

$$\kappa_{ij} := \frac{\partial h_{ij}}{\partial t}. \tag{2.6}$$

These quantities will also form a three-dimensional tensor. All operations of shifting indices and covariant derivation of κ_{ij} will be done in three-dimensional space by using the metric h_{ij}. Furthermore the sum ${\kappa^i}_i$ is the logarithmic derivative of the determinant[1] $h = -g$:

$${\kappa^i}_i = h^{ij} \frac{\partial h_{ji}}{\partial t} = \frac{\partial}{\partial t} \ln(h). \tag{2.7}$$

The Christoffel symbols are calculated according to

$${\Gamma^\mu}_{\nu\rho} = \frac{1}{2} g^{\mu\tau} (g_{\tau\nu,\rho} + g_{\tau\rho,\nu} - g_{\nu\rho,\tau}) \tag{2.8}$$

and inserting the hypersurface metric one obtains the expressions

$$\begin{gathered} {\Gamma^0}_{00} = {\Gamma^i}_{00} = {\Gamma^0}_{0i} = 0, \\ {\Gamma^0}_{ij} = \tfrac{1}{2}\kappa_{ij}, \qquad {\Gamma^i}_{0j} = \tfrac{1}{2}{\kappa^i}_j, \qquad {\Gamma^i}_{jk} = {\lambda^i}_{jk}, \end{gathered} \tag{2.9}$$

where ${\lambda^i}_{jk}$ are the three-dimensional Christoffel symbols formed when substituting the metric $g_{\alpha\beta}$ with h_{ij} in equation (2.8).

The Ricci tensor is calculated according to

$$R_{\mu\nu} = {\Gamma^\rho}_{\mu\nu,\rho} - {\Gamma^\rho}_{\mu\rho,\nu} + {\Gamma^\rho}_{\tau\rho}{\Gamma^\tau}_{\mu\nu} - {\Gamma^\rho}_{\tau\nu}{\Gamma^\tau}_{\mu\rho}. \tag{2.10}$$

---

[1] See for instance [12] page 12-13 for justification.

Using the Christoffel components in (2.9), the components for $R_{\mu\nu}$ are then

$$\begin{aligned} R_{00} &= -\frac{1}{2}\frac{\partial}{\partial t}\kappa^i{}_i - \frac{1}{4}\kappa^j{}_i\kappa^i{}_j, \\ R_{0i} &= \frac{1}{2}(\nabla_j\kappa^j{}_i - \nabla_i\kappa^j{}_j), \\ R_{ij} &= \frac{1}{2}\frac{\partial}{\partial t}\kappa_{ij} + \frac{1}{4}(\kappa_{ij}\kappa^k{}_k - 2\kappa^k{}_i\kappa_{jk}) + {}^*R_{ij}. \end{aligned} \tag{2.11}$$

Here ${}^*R$ is the three-dimensional Ricci tensor which is expressed in terms of h_{ij} and $\lambda^i{}_{jk}$ instead of $g_{\mu\nu}$ and $\Gamma^\mu{}_{\nu\rho}$.

The Einstein equation in mixed components and expressed in the alternative form is

$$R^\mu{}_\nu = 8\pi(T^\mu{}_\nu - \frac{1}{2}T\delta^\mu{}_\nu). \tag{2.12}$$

where$\delta^\mu{}_\nu$ is the Kronecker delta. Taking the 00-component of this equation, we have

$$R^0{}_0 = \frac{1}{2}\frac{\partial}{\partial t}\kappa^i{}_i + \frac{1}{4}\kappa^j{}_i\kappa^i{}_j = 8\pi(T^0{}_0 - \frac{1}{2}T). \tag{2.13}$$

Now using the 4-velocity of the hypersurface, the right hand side of equation (2.13), for any matter distribution in a synchronous coordinate system, can be expressed as:

$$\begin{aligned} (T^0{}_0 - \frac{1}{2}T) &= (p+\rho)u^0u_0 + p - \frac{1}{2}(p+\rho)u^\mu u_\mu - 2p \\ &= -\frac{1}{2}(p+\rho) - p \\ &= -\frac{1}{2}(3p+\rho). \end{aligned} \tag{2.14}$$

where p and ρ are the pressure and energy density of the matter respectively. Provided that $(T^0{}_0 - \frac{1}{2}T) \leq 0$[2], then this must also be true for $R^0{}_0$

$$R^0{}_0 = \frac{1}{2}\frac{\partial}{\partial t}\kappa^i{}_i + \frac{1}{4}\kappa^j{}_i\kappa^i{}_j \leq 0 \tag{2.15}$$

With the algebraic inequality

$$\kappa^i{}_j\kappa^j{}_i \geq \frac{1}{3}(\kappa^i{}_i)^2 \tag{2.16}$$

we can rewrite equation (2.15) into

$$\frac{\partial}{\partial t}\kappa^i{}_i + \frac{1}{6}(\kappa^i{}_i)^2 \leq 0$$

or equivalently

---

[2] This places constraints on the type of matter that is included in the space. Matter with negative pressure (such as dark energy) would violate this inequality and such spaces would thereby avoid the following consequences.

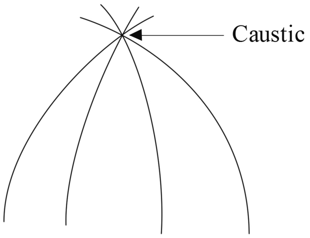

Figure 2.2: Geodesics converging into a caustic. These will appear as coordinate singularities in the synchronous coordinate system. It must be emphasized that these singularities are fictitious.

$$\frac{\partial}{\partial t}\Big(\frac{1}{\kappa^i{}_i}\Big) \geq \frac{1}{6}. \tag{2.17}$$

Let us investigate the consequences of equation (2.17). Suppose that, at a certain initial time, $\kappa^i{}_i > 0$. Since the derivative of the quantity $1/\kappa^i{}_i$ is positive, this implies that as time progresses, $1/\kappa^i{}_i$ must also increase. Conversely, if time would be rewinded, the quantity $1/\kappa^i{}_i$ must instead decrease towards zero in a finite amount of time, or equivalently, $\kappa^i{}_i \to +\infty$ as time is rewinded. This in turn implies, by equation (2.6), that $h \to 0$ as time is rewinded. Similar reasoning yields the same result if $\kappa^i{}_i < 0$ initially, but for increasing times [10].

Because of the above argument, the determinant of a metric in a synchronous coordinate system will necessarily go to zero in a finite length of time. This gives rise to singularities, which might be of a real physical origin or not. Generally though, these singularities are fictitious and will vanish when we change to another (non-synchronous) coordinate system. The origin of these fictitious (or coordinate) singularities are of a geometric origin. As mentioned earlier, the synchronous coordinate system consists of a family of timelike geodesics intersecting orthogonally spacelike hypersurfaces. However geodesics of an arbitrary family will, in general, converge at some point. The point at which some of the geodesics come together is known as *caustics* [12]. These are analogues to caustics in geometrical optics. Because these timelike geodesics are also coordinate lines, caustics are therefore coordinate singularities. It is important to realize that appearance of caustics are inevitable in synchronous coordinate systems with the curvature property $R^0{}_0 \leq 0$ [10], as will be the case in my models. This will have important consequences, since this places constraints on how far into time the models can be observed using synchronous coordinates.

2.1.2 3+1 Splitting

The synchronous coordinate system leads naturally to the 3+1 splitting of the Einstein field equations and subsequent orthonormal frame formalism. The 3+1 splitting is a term referring to the method of dividing (or splitting) of spacetime into a space and time part. This allows for a more intuitive way to study dynamical processes in general relativity, initial conditions can be used and kinematic quantities are studied as functions of time [7, 11].

Once a synchronous coordinate system has been set up, the timelike 4-velocity u^μ will be used to split spacetime into a space and time part. Using u^μ, one can construct tensors $U^\mu{}_\nu$ and

$h^{\mu}{}_{\nu}$ which decomposes the metric $\delta^{\mu}{}_{\nu}$ into a parallel and orthogonal part respectively, defined by [11, 12]

$$U^{\mu}{}_{\nu} := -u^{\mu}u_{\nu}, \qquad h^{\mu}{}_{\nu} := \delta^{\mu}{}_{\nu} - U^{\mu}{}_{\nu}. \tag{2.18}$$

Notice that $h_{\mu\nu}$ is orthogonal to u^{μ}

$$\begin{aligned} u^{\mu}h_{\mu\nu} &= u^{\mu}g_{\mu\nu} - u^{\mu}U_{\mu\nu} \\ &= u_{\nu} + u^{\mu}u_{\mu}u_{\nu} \\ &= u_{\nu} - u_{\nu} \\ &= 0 \end{aligned} \tag{2.19}$$

An important property of projection operators is that for any projection operator P

$$P^2 = P.$$

This is also the case for $h_{\mu\nu}$, since by contracting $h^{\mu}{}_{\nu}$ with itself results in

$$\begin{aligned} h^{\mu}{}_{\nu}h^{\nu}{}_{\rho} &= (\delta^{\mu}{}_{\nu} - U^{\mu}{}_{\nu})(\delta^{\nu}{}_{\rho} - U^{\nu}{}_{\rho}) \\ &= \delta^{\mu}{}_{\rho} - 2U^{\mu}{}_{\rho} + U^{\mu}{}_{\nu}U^{\nu}{}_{\rho} \\ &= \delta^{\mu}{}_{\rho} - U^{\mu}{}_{\rho} \\ &= h^{\mu}{}_{\rho}. \end{aligned}$$

Therefore, in addition to being the metric tensor on the hypersurface, $h_{\mu\nu}$ can also be called the *projection tensor* since it also projects any vector or tensor onto the hypersurface orthogonal to u^{μ}. Only the spatial components are non-zero and appears in (2.5) [2, 10, 12].

From the definition of $U^{\mu}{}_{\nu}$, it is visible that $u_{\mu}U^{\mu}{}_{\nu} = u_{\nu}$. Therefore the two tensors $U_{\mu\nu}$ and $h_{\mu\nu}$ are considered, respectively, as the time and spatial components of the metric $g_{\mu\nu}$.

Due to the extra structure imposed by u^{μ}, all geometrical quantities of physical interest can be decomposed into a 3+1 formalism. This will be done for the covariant derivative $\nabla_{\mu}u_{\nu}$, which is decomposed into several irreducible parts. The 4-acceleration of the hypersurface is [2]:

$$\dot{u}^{\mu} := u^{\nu}\nabla_{\nu}u^{\mu} \tag{2.20}$$

This is essentially a time derivative since u^{μ} points in the direction time develops. Therefore in resemblance with ordinary derivatives with respect to time, a dot will be used to denote covariant differentiation along u^{μ}, such that $\dot{X} = u^{\mu}\nabla_{\mu}X$. Notice also that since

$$\begin{aligned} u^{\nu}\nabla_{\nu}(-1) &= u^{\nu}\nabla_{\nu}(u^{\mu}u_{\mu}) \\ &= u^{\nu}(u_{\mu}\nabla_{\nu}u^{\mu} + u^{\mu}\nabla_{\nu}u_{\mu}) \\ &= u^{\nu}(u^{\mu}\nabla_{\nu}u_{\mu} + u^{\mu}\nabla_{\nu}u_{\mu}) \\ &= 2u^{\nu}u^{\mu}\nabla_{\nu}u_{\mu} \end{aligned}$$

However because

$$\nabla_\nu(-1) = 0$$

implies that

$$u^\nu u^\mu \nabla_\nu u_\mu = u^\mu \dot{u}_\mu = 0 \tag{2.21}$$

In conclusion, the 4-acceleration and the 4-velocity are orthogonal [13].

Then define the *expansion scalar*

$$\Theta := \nabla_\mu u^\mu \tag{2.22}$$

which measures the fractional change of volume per unit time of the hypersurface.

The *shear tensor* $\sigma_{\mu\nu}$ describes the shearing and is defined according to

$$\sigma_{\mu\nu} := \frac{1}{2}(h^\rho{}_\nu \nabla_\rho u_\mu + h^\rho{}_\mu \nabla_\rho u_\nu) - \frac{1}{3}\Theta h_{\mu\nu} \tag{2.23}$$

Finally, the *rotation tensor* $\omega_{\mu\nu}$ (or *vorticity tensor*) is defined as

$$\omega_{\mu\nu} := \frac{1}{2}(h^\rho{}_\nu \nabla_\rho u_\mu - h^\rho{}_\mu \nabla_\rho u_\nu) \tag{2.24}$$

The rotation tensor contains information about the rotation [2, 12].

By using these definitions, it is clear that [2, 9]

$$\nabla_\mu u_\nu = -\omega_{\mu\nu} + \sigma_{\mu\nu} + \frac{1}{3}\Theta h_{\mu\nu} - u_\mu \dot{u}_\nu \tag{2.25}$$

We see also that contracting with u^μ results in the expression

$$u^\mu \nabla_\mu u_\nu = -u^\mu \omega_{\mu\nu} + u^\mu \sigma_{\mu\nu} + \frac{1}{3}\Theta u^\mu h_{\mu\nu} - u^\mu u_\mu \dot{u}_\nu. \tag{2.26}$$

From the definitions (2.23), (2.24) and by using the orthogonality property of $h_{\mu\nu}$ (2.19) one obtains equation (2.20).

Furthermore we can divide equation (2.26) into two parts, one parallel and one orthogonal to u^μ [9]

$$\nabla_\mu u_\nu = -u_\mu \dot{u}_\nu + \theta_{\mu\nu} \tag{2.27}$$

where the tensor $\theta_{\mu\nu}$ is defined as

$$\theta_{\mu\nu} := -\omega_{\mu\nu} + \sigma_{\mu\nu} + \frac{1}{3}\Theta h_{\mu\nu} \tag{2.28}$$

Thus $\theta_{\mu\nu}$ is the spatial projection of $\nabla_\mu u_\nu$. The quantities Θ, $\sigma_{\mu\nu}$ and $\omega_{\mu\nu}$ correspond to the trace, symmetric trace-free and anti-symmetric parts of $\theta_{\mu\nu}$ respectively.

Notice that equation 2.20 is the geodesic equation. Due to construction, u^μ is the 4-velocity of the hypersurface. This implies that u^μ is parallel to a geodesic and through a proper choice of affine parameters, the geodesic equation can always be set to zero, i.e. $\dot{u}^\mu = 0$ [12]. I will henceforth do so, and thus equation (2.26) is also equal to zero.

In addition $u^\nu \nabla_\mu u_\nu = \frac{1}{2}\nabla_\mu(u^\nu u_\nu) = 0$ due to equation (2.4). This implies, together with the previous result, that $\nabla_\mu u_\nu$ is orthogonal to u^μ and thus spatial[12].

For convenience, the following quantities are defined as well [11, 9]

$$\sigma^2 := \frac{1}{2}\sigma_{\mu\nu}\sigma^{\mu\nu} \tag{2.29}$$

which is the magnitude of the shear tensor, and

$$\omega^\mu := \frac{1}{2}\eta^{\mu\nu\rho\sigma}\omega_{\nu\rho}u_\sigma \qquad \Leftrightarrow \qquad \omega_{\mu\nu} = \eta_{\mu\nu\rho\sigma}\omega^\rho u^\sigma \tag{2.30}$$

which is the *rotation vector*. Here $\eta^{\mu\nu\rho\sigma}$ is the totally anti-symmetric tensor, with the sign convention $\eta^{0123} = 1/\sqrt{-g}$ and $\eta_{0123} = -\sqrt{-g}$, where g is the determinant of the metric tensor. Furthermore the magnitude of the rotation tensor is defined as

$$\omega^2 := \omega_\mu\omega^\mu = \omega_{\mu\nu}\omega^{\mu\nu}. \tag{2.31}$$

Before moving on, we will direct our attention back to the rotation tensor $\omega_{\mu\nu}$ for a moment. Recalling that $\dot{u}^\mu = 0$, one can express the rotation tensor as $\omega_{\mu\nu} = \nabla_{[\nu}u_{\mu]}$. Since u^μ is hypersurface orthogonal, then $u_\mu = -k\Phi,_\mu$ where k and Φ are scalar functions. This allows for an expression of $\omega_{\mu\nu}$ in terms of scalar functions. Applying the symmetry $\nabla_{[\mu}\Phi,_{\nu]} = 0$, the new expression for $\omega_{\mu\nu}$ is

$$\omega_{\mu\nu} = \Phi_{[,\mu}\, k,_{\nu]} = -\frac{1}{k}u_{[\mu}k,_{\nu]}\,. \tag{2.32}$$

In any case, $\omega_{\mu\nu}$ is still orthogonal to u^μ and therefore the contraction $\omega_{\mu\nu}u^\nu = 0$ implies that

$$-\frac{1}{k}u_{[\mu}k,_{\nu]}\, u^\nu = 0 \iff k,_\mu = -u_\mu k,_\nu\, u^\nu$$

whereas this in turn, if substituted into (2.32) establishes that the rotation tensor vanishes: $\omega_{\mu\nu} = 0$, in synchronous coordinate systems [12]. This is fortunate as this will simplify our evolution equations as we will see further on.

2.1.3 3+1 Orthonormal Frame Approach

In the orthonormal frame approach, one chooses at each point in spacetime a set of four linearly independent 1-forms $\{\boldsymbol{\omega}^a\}$ causing the line element of a metric to look locally as

$$\mathbf{g} = \eta_{ab}\boldsymbol{\omega}^a \otimes \boldsymbol{\omega}^b \tag{2.33}$$

where $\eta_{ab} = \mathrm{diag}(-1,1,1,1)$ is the constant Minkowski metric. The vectors $\{\mathbf{e}_a\}$ dual to the 1-forms $\{\boldsymbol{\omega}^a\}$ must satisfy the relation

$$\boldsymbol{\omega}^a\mathbf{e}_a = 1 \tag{2.34}$$

In the 3+1 orthonormal frame approach, $\boldsymbol{e}_0$ is aligned parallel to the preferred timelike direction u^μ [11]. We will do this by setting $u^\mu = e_0^\mu$, and then choose three additional set of vectors $\{e_\alpha^\mu\}$ where $\alpha = 1-3$ label the vectors individually. These additional vectors must be orthogonal spacelike unit vectors, i.e. $e_\mu^\alpha e_\beta^\mu = \delta_\beta^\alpha$ and $e_\alpha^\mu e_\mu^0 = 0$. Together these four vectors form an orthonormal tetrad $\{e_a^\mu\}$, where $a = 0 - 3$. These vectors can be used to convert any tensor from any arbitrary coordinate basis to an orthonormal frame [2, 12],

$$T^{ab\ldots}{}_{cd\ldots} = e^a_\mu e^b_\nu \cdots e^\rho_c e^\sigma_d \cdots T^{\mu\nu\ldots}{}_{\rho\sigma\ldots}. \tag{2.35}$$

In conjunction with the orthonormal basis vectors, one can also introduce the spatial commutation functions $\gamma^\alpha{}_{\beta\gamma}$, defined by the commutator $[\boldsymbol{e}_\beta, \boldsymbol{e}_\gamma] = \gamma^\alpha{}_{\beta\gamma}\boldsymbol{e}_\alpha$, where $\boldsymbol{e}_a$ are understood to be differential operators $\boldsymbol{e}_a = e^\mu_a \partial_\mu$. According to [9, 11] (see also references therein) these commutation functions can be decomposed into a 1-index object a_α and a symmetric 2-index object $n_{\alpha\beta}$

$$\gamma^\alpha{}_{\beta\gamma} = 2a_{[\beta}\delta^\alpha{}_{\gamma]} + \epsilon_{\beta\gamma\delta}n^{\delta\alpha}, \tag{2.36}$$

where $\epsilon_{\alpha\beta\gamma}$ is the totally anti-symmetric tensor with $\epsilon_{123} = \epsilon^{123} = 1$.

One remaining parameter that can now be defined is the local angular velocity of the spatial frame vectors

$$\Omega^\alpha = \frac{1}{2}\epsilon^{\alpha\beta\gamma}e^\mu_\beta \dot{e}_{\gamma\mu}. \tag{2.37}$$

2.2 Conformal Geometry and the 3-Sphere

2.2.1 Conformal Geometry: Terminology

Suppose we have two Riemann spaces U_n and V_n, with the same dimension n and with the metrics $\boldsymbol{g}$ and $\boldsymbol{h}$ respectively. If the metrics $\boldsymbol{g}$ and $\boldsymbol{h}$ are related by

$$\boldsymbol{g} = \phi^2\boldsymbol{h}, \tag{2.38}$$

where ϕ^2 is a scalar function, referred to as the *conformal factor*, then the Riemann spaces U_n and V_n are said to be *conformally related.* A special case is when a space U_n is conformally related to the flat Euclidean space, in which case U_n is said to be *conformally flat* [14]. This has a few nifty implications which will be used diligently throughout this thesis and is therefore worth introducing.

2.2.2 Stereographic Projection

When looking at a map of our world, what we see is a *projection* of our globe, which can be considered spherical for our purposes and is called a 2-sphere[3]. A map is a projection of our globe on a two-dimensional Euclidean surface. However the intrinsic geometry of the Euclidean surface and the 2-sphere is different and therefore distances on the globe will not be the same as on the flat map [13], i.e. all flat maps will contain distortions. Cartographers must therefore choose a projection which suits the intended reader the best. For instance in geography; an area-preserving mapping is common, whereas for navigating a cartographer might opt for a

---

[3] A note on terminology. A 2-sphere is the *surface* of an “ordinary” sphere, such as our globe. The number 2 comes from the number of parameters required to parametrize the surface. To talk about not only the surface, then a globe would be called a 3-ball. This is usually the case in physics. In mathematics the naming convention is different. The surface of our globe would be called a 3-sphere, since it is embedded in three dimensional space.

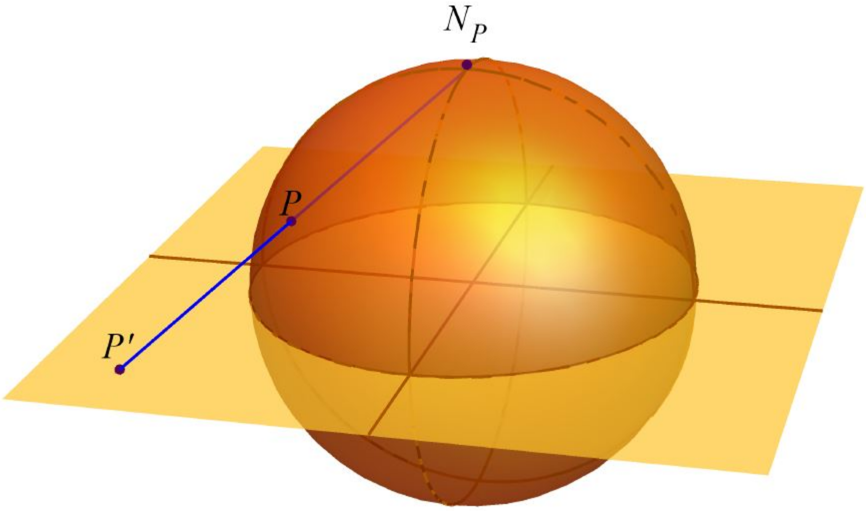

Figure 2.3: Stereographic projection for the 2-sphere from the north pole onto the plane $z = 0$.

geodesic mapping; which maps geodesics onto each other (thus the great circles on the 2-sphere are represented as straight lines on the two-dimensional Euclidean surface). A third option is to use a *conformal* mapping, which preserves angles between vectors on the space [15].

One such conformal mapping is the stereographic projection [15]. The principle idea behind stereographic projection is illustrated by figure 2.3. The north pole N_P is chosen as a reference point. Then a line is drawn between N_P and a point P on the 2-sphere until it intersects the plane $z = 0$. The point P is then said to be mapped onto the point P' on the plane. The sphere's southern hemisphere will be mapped onto the circular disk inside the sphere, while the northern hemisphere will be mapped onto all the points outside the sphere. However there will be no point on the plane corresponding to the north pole; it is said to be mapped to infinity. Thus curves crossing the north pole will be mapped into lines stretching towards infinity.

For the case of a 2-sphere with coordinates $(\theta,\, \phi)$ projected onto the plane with coordinates $(r,\, \phi)$, the mapping from the 2-sphere to the plane is given by $\theta \mapsto r = \cot(\theta/2)$, while the inverse is $r \mapsto \theta = 2\arctan(1/r)$.

The stereographic projection can be generalized to any n-sphere, such as the unit 3-sphere (or *hypersphere*) which is of utmost importance in this thesis. The unit 3-sphere is, analogously to other n-spheres, the set of points $S^3 = \{(w,\, x,\, y,\, z) \,|\, w^2 + x^2 + y^2 + z^2 = 1\}$. Thus the 3-sphere can be parametrized by the three *hyperspherical coordinates* $(\chi,\, \theta,\, \phi)$ where $\chi \in [0,\, \pi]$, $\theta \in [0,\, \pi]$ and $\phi \in [0,\, 2\pi[$. The relationship between the Cartesian and hyperspherical coordinates on the 3-sphere is

$$\begin{aligned} w &= \cos\chi \\ x &= \sin\chi\sin\theta\cos\phi \\ y &= \sin\chi\sin\theta\sin\phi \\ z &= \sin\chi\cos\theta \end{aligned}$$

and the 3-sphere metric is [2, 7]

$$S_3 = d\chi^2 + \sin^2\chi(d\theta^2 + \sin^2\theta d\phi^2). \tag{2.39}$$

Notice that the metric determinant $\sin^4\chi\sin^2\theta$ is zero at $\chi = 0$ and $\chi = \pi$. These points are thus coordinate singularities and will be referred to as the north and south pole respectively.

Since the 3-sphere is embedded in a four-dimensional space, imagining the object is very difficult. Therefore a projection of the 3-sphere onto the more familiar three-dimensional Euclidean space is helpful. Using stereographic projection, the transformation is given by transforming the χ-coordinate on the 3-sphere by a radial coordinate r in the Euclidean 3-space:

$$\chi \longmapsto r = \cot\frac{\chi}{2} \text{ with the inverse } r \longmapsto \chi = 2\arctan\frac{1}{r}.$$

First of all this implies that, in the Euclidean space, the south pole lies at the origin while the north pole lies at infinity. Thus all lines and surfaces stretching out to infinity in the Euclidean space are actually not infinitely long, but ends at the north pole on the 3-sphere. In addition since the stereographic projection is a conformal mapping, spheres and circles on the 3-sphere will remain a sphere or circle respectively on the Euclidean 3-space, unless the object contains the north pole. If that is the case, then circles will become curves stretching out to infinity while spheres become surfaces stretching out to infinity in the 3-space. This is well illustrated by Hilbert and Cohn-Vossen in [15] for the 2-sphere.

2.2.3 Conformal Flatness of the 3-Sphere

Since stereographic projection is a conformal mapping the 3-sphere is conformally flat. This becomes clear if we perform the inverse stereographic projection (see above) on the Euclidean metric $\boldsymbol{e_3} = dr^2 + r^2(d\theta^2 + \sin^2\theta d\phi^2)$:

$$\begin{aligned} E_3 &= \frac{1}{4\sin^4\frac{\chi}{2}}d\chi^2 + \cot^2\frac{\chi}{2}(d\theta^2 + \sin^2\theta d\phi^2) \\ &= \frac{1}{4\sin^4\frac{\chi}{2}}\left[d\chi^2 + 4\cos^2\frac{\chi}{2}\sin^2\frac{\chi}{2}(d\theta^2 + \sin^2\theta d\phi^2)\right] \\ &= \frac{1}{4\sin^4\frac{\chi}{2}}\left[d\chi^2 + \sin^2\chi(d\theta^2 + \sin^2\theta d\phi^2)\right] \\ &= \frac{1}{4\sin^4\frac{\chi}{2}}S_3 \end{aligned} \tag{2.40}$$

where the conformal factor is $1/4\sin^4\frac{\chi}{2}$. Of course there are other transformations with other conformal factors, but the point is the conformal flatness of the 3-sphere. From this and (2.38) we can also conclude that any metric conformally related to the 3-sphere must also be conformally flat.

2.3 The Weyl Tensor

Due to the many symmetries of the Riemann tensor, there are only $\frac{1}{12}n^2\left(n^2-1\right)$ algebraically independent quantities, where n is the dimension of the manifold the Riemann tensor describes. Out of these, $\frac{1}{2}n(n+1)$ quantities are contained in the Ricci tensor (for $n \geq 3$). Thus for $n=1$, space is flat and the Riemann tensor is identically zero. For $n=2$, there is only one quantity which is essentially the curvature scalar. For $n=3$ the Riemann tensor is completely determined by the Ricci tensor. However for $n>3$, there are quantities that can be represented by the Weyl tensor, defined as [16]

$$C_{\mu\nu\rho\sigma} := R_{\mu\nu\rho\sigma} + \frac{2}{n-2}(g_{\mu[\sigma}R_{\rho]\nu} + g_{\nu[\rho}R_{\sigma]\mu}) + \frac{2}{(n-1)(n-2)}Rg_{\mu[\rho}g_{\sigma]\nu}. \tag{2.41}$$

The Weyl tensor is identically zero if $n \leq 3$.

The Weyl tensor inherits all the symmetries of the Riemann tensor. In addition to that, it is also traceless [16]

$$C^{\mu}{}_{\nu\mu\sigma} = 0 \tag{2.42}$$

It is common to use the Weyl tensor when formulating gravito-electromagnetism: a gravitational analogy to Maxwell´s theory.

The Maxwell tensor $F_{\mu\nu}$ can be decomposed into electric and magnetic fields as measured by an observer u^μ

$$E_\mu = F_{\mu\nu}u^\nu \qquad H_\mu = \frac{1}{2}\epsilon_{\mu\nu\rho}F^{\nu\rho} := {}^*F_{\mu\nu}u^\nu \tag{2.43}$$

where $\epsilon_{\mu\nu\rho}$ is the completely anti-symmetric tensor. Due to the anti-symmetric nature of the Maxwell tensor, E_μ and H_μ are spatial tensors:

$$\begin{aligned} u^\mu E_\mu = u^\mu F_{\mu\nu}u^\nu &= -u^\nu F_{\nu\mu}u^\mu = -u^\nu E_\nu \\ \implies u^\mu E_\mu &= 0 \end{aligned}$$

and similarly for the magnetic field H_μ. These spatial and physically measurable vectors completely determine the Maxwell tensor since [17]

$$F_{\mu\nu} = 2u_{[\mu}E_{\nu]} + \epsilon_{\mu\nu\rho}H^\rho. \tag{2.44}$$

By replacing the Maxwell tensor with the Weyl tensor, one obtains the electric and magnetic gravitational analogies

$$E_{\mu\nu} = C_{\mu\rho\nu\sigma}u^\rho u^\sigma \qquad H_{\mu\nu} = {}^*C_{\mu\rho\nu\sigma}u^\rho u^\sigma. \tag{2.45}$$

Here ${}^*C_{\mu\rho\nu\sigma} := \frac{1}{2}\eta_{\mu\rho}{}^{\tau\phi}C_{\tau\phi\nu\sigma}$ is the dual of the Weyl tensor, where $\eta^{\mu\nu\rho\sigma}$ is the completely anti-symmetric tensor [17].

Due to the properties of the Weyl tensor and its dual, the tensors $E_{\mu\nu}$ and $H_{\mu\nu}$ obtain the properties of symmetry and tracelessness: $E_{\nu\mu} = C_{\nu\rho\mu\sigma}u^\rho u^\sigma = C_{\mu\sigma\nu\rho}u^\rho u^\sigma = E_{\mu\nu}$ proves symmetry while $E^\mu{}_\mu = C^\mu{}_{\rho\mu\sigma}u^\rho u^\sigma = 0$ proves tracelessness.

Just like the electric and magnetic fields are spatial, so are the gravitational analogies $E_{\mu\nu}$ and $H_{\mu\nu}$:

$$u^{\mu}E_{\mu\nu} = u^{\mu}C_{\mu\rho\nu\sigma}u^{\rho}u^{\sigma} = 0$$

The last equality follows since we are contracting a symmetric tensor ($u^{\mu}u^{\rho}$) with an anti-symmetric one ($C_{\mu\rho\nu\sigma}$). The conclusion is that gravito-electric/magnetic tensors are spatial, just like their Maxwell counterparts. In the frame of comoving observers are the gravito-electric/magnetic tensors physically measurable, and in $n = 4$ do these tensors completely specify the Weyl tensor through [17]

$$C_{\mu\nu}{}^{\rho\sigma} = 4(u_{[\mu}u^{[\rho} + h_{[\rho}{}^{[\rho})E_{\nu]}{}^{\sigma]} + 2\epsilon_{\mu\nu\xi}u^{[\rho}H^{\sigma]\xi} + 2u_{[\mu}H_{\nu]\xi}\epsilon^{\rho\sigma\xi}. \tag{2.46}$$

Equation (2.46) is the gravito-electromagnetic analogy of equation (2.44). The analogy is further reinforced by $E_{\mu\nu}$ and $H_{\mu\nu}$ covariantly (and gauge-invariantly) describing gravitational waves on a FLRW background. Also similar to the electromagnetic case, in which there are no monopole charge sources for H_{μ} only multipole charge sources, there are no monopole sources for the gravito-magnetic field. The dipole charge source for the gravito-magnetic field $H_{\mu\nu}$ is $(\rho+p)\omega^{\mu}$, also known as *angular momentum density*. However, the presence of the angular momentum density does not always imply the presence of a gravito-magnetic field [17].

The Weyl tensor is also known as the *conformal curvature tensor*. The Weyl tensor is actually the same for any two metrics which are conformally related[4]. This implies for instance that for any conformally flat space, the Weyl tensor is identically zero (since the Weyl tensor is zero in flat Euclidean space) [14]. Therefore the Weyl tensor is then identically zero in spherical FLRW spaces, since these are conformally flat (by being conformally related to the 3-sphere).

However this does *not* imply that every three-dimensional metric is conformally flat just because the Weyl tensor is identically zero in three dimensions. For three dimensions, the necessary and sufficient condition for a metric to be conformally flat is the vanishing of the *Cotton-York tensor*. Although in two dimensions, even though the Weyl tensor is undetermined, all two-dimensional metrics are conformally flat [14].

---

[4] The proof of this statement is provided for instance in [14] on p. 58.

Chapter 3

The Kinematic Quantities

This chapter presents the equations governing dynamics, the constraint equations and several kinematic quantities. Fortunately, we will se that applying several symmetry conditions will greatly simplify the equations and several kinematic quantities will vanish.

3.1 Evolution Equations

The vacuum field equations, Jacobi identities and Bianchi identities can be expressed in terms of the frame vectors $\{e_a^\mu\}$ and the quantities $\{\Theta,\, \dot{u}_\alpha,\, \sigma_{\alpha\beta},\, \omega_\alpha,\, \Omega_\alpha,\, a_\alpha,\, n_{\alpha\beta},\, E_{\alpha\beta},\, H_{\alpha\beta}\}$. For a fuller account, see [11] and references therein. In vacuum, absence of cosmological constant and setting $\dot{u}^\mu = 0$, the evolution equations become [9]:

$$\boldsymbol{e}_0(\Theta) = -\frac{1}{3}\Theta^2 - 2\sigma^2 + 2\omega^2 \tag{3.1}$$

$$\boldsymbol{e}_0(\sigma^{\alpha\beta}) = -\Theta\sigma^{\alpha\beta} + 2\omega^{(\alpha}\Omega^{\beta)} - {}^*S^{\alpha\beta} - \frac{2}{3}\delta^{\alpha\beta}\omega_\gamma\Omega^\gamma + 2\epsilon^{\gamma\delta(\alpha}\Omega_\gamma\sigma^{\beta)}{}_\delta \tag{3.2}$$

$$\boldsymbol{e}_0(\omega^\alpha) = -\frac{2}{3}\Theta\omega^\alpha + \sigma^\alpha{}_\beta\omega^\beta - \epsilon^{\alpha\beta\gamma}\omega_\beta\Omega_\gamma \tag{3.3}$$

$$\begin{aligned}\boldsymbol{e}_0(E^{\alpha\beta}) = {} & -\Theta E^{\alpha\beta} + 3\sigma^{(\alpha}{}_\gamma E^{\beta)\gamma} + \frac{1}{2}n^\gamma{}_\gamma H^{\alpha\beta} - 3n^{(\alpha}{}_\gamma H^{\beta)\gamma} \\ & -\delta^{\alpha\beta}[\sigma_{\gamma\delta}E^{\gamma\delta} - n_{\gamma\delta}H^{\gamma\delta}] + \epsilon^{\gamma\delta(\alpha}[(\boldsymbol{e}_\gamma - a_\gamma)(H^{\beta)}{}_\delta) \\ & -(\omega_\gamma - 2\Omega_\gamma)E^{\beta)}{}_\delta]\end{aligned} \tag{3.4}$$

$$\begin{aligned}\boldsymbol{e}_0(H^{\alpha\beta}) = {} & -\Theta H^{\alpha\beta} + 3\sigma^{(\alpha}{}_\gamma H^{\beta)\gamma} - \frac{1}{2}n^\gamma{}_\gamma E^{\alpha\beta} + 3n^{(\alpha}{}_\gamma E^{\beta)\gamma} \\ & -\delta^{\alpha\beta}[\sigma_{\gamma\delta}H^{\gamma\delta} + n_{\gamma\delta}E^{\gamma\delta}] - \epsilon^{\gamma\delta(\alpha}[(\boldsymbol{e}_\gamma - a_\gamma)(E^{\beta)}{}_\delta) \\ & +(\omega_\gamma - 2\Omega_\gamma)H^{\beta)}{}_\delta]\end{aligned} \tag{3.5}$$

$$\begin{aligned}\boldsymbol{e}_0(a^\alpha) = &-\frac{1}{3}(\delta^{\alpha\beta}\boldsymbol{e}_\beta + a^\alpha)(\Theta) + \frac{1}{2}(\boldsymbol{e}_\beta - 2a_\beta)(\sigma^{\alpha\beta}) \\ &-\frac{1}{2}\epsilon^{\alpha\beta\gamma}(\boldsymbol{e}_\beta - 2a_\beta)(\omega_\gamma - \Omega_\gamma)\end{aligned} \tag{3.6}$$

$$\begin{aligned}\boldsymbol{e}_0(n^{\alpha\beta}) = &-\frac{1}{3}\Theta n^{\alpha\beta} - \delta^{\gamma(\alpha}\boldsymbol{e}_\gamma(\omega^{\beta)} - \Omega^{\beta)}) + 2\sigma^{(\alpha}{}_\gamma n^{\beta)\gamma} + \delta^{\alpha\beta}\boldsymbol{e}_\gamma(\omega^\gamma - \Omega^\gamma) \\ &-\epsilon^{\gamma\delta(\alpha}[\boldsymbol{e}_\gamma(\sigma^{\beta)}{}_\delta) - 2n^{\beta)}{}_\gamma(\omega_\delta - \Omega_\delta)]\end{aligned} \tag{3.7}$$

with the relevant constraints

$$0 = -\frac{1}{3}\Theta^2 + \sigma^2 - \omega^2 - 2\omega_\alpha\Omega^\alpha - \frac{1}{2}{}^*R \tag{3.8}$$

$$\begin{aligned}0 = &-E_{\alpha\beta} + \frac{1}{3}\Theta\sigma_{\alpha\beta} - \sigma_{\alpha\gamma}\sigma^\gamma{}_\beta - \omega_\alpha\omega_\beta - 2\omega_{(\alpha}\Omega_{\beta)} \\ &+\frac{1}{3}\delta_{\alpha\beta}[2\sigma^2 + \omega^2 + 2\omega_\gamma\Omega^\gamma] + {}^*S_{\alpha\beta}\end{aligned} \tag{3.9}$$

$$\begin{aligned}0 = &-H_{\alpha\beta} + (\boldsymbol{e}_{[\alpha} + a_{(\alpha})(\omega_{\beta)}) + \frac{1}{2}n^\gamma{}_\gamma\sigma_{\alpha\beta} - 3n^\gamma{}_{(\alpha}\sigma_{\beta)\gamma} - \frac{1}{3}\delta_{\alpha\beta}[(\boldsymbol{e}_\gamma + a_\gamma)(\omega^\gamma) \\ &-3n_{\gamma\delta}\sigma^{\gamma\delta}] + \epsilon^{\gamma\delta}{}_{(\alpha}[(\boldsymbol{e}_{|\gamma|} - a_{|\gamma|})(\sigma_{\beta)\delta}) - n_{\beta)\gamma}\omega_\delta]\end{aligned} \tag{3.10}$$

$$\begin{aligned}0 = &-\frac{2}{3}\delta^{\alpha\beta}\boldsymbol{e}_\beta(\Theta) + (\boldsymbol{e}_\beta - 3a_\beta)(\sigma^{\alpha\beta}) + n^\alpha{}_\beta\omega^\beta \\ &-\epsilon^{\alpha\beta\gamma}[(\boldsymbol{e}_\beta - a_\beta)(\omega_\gamma) + n_{\beta\delta}\sigma^\delta{}_\gamma]\end{aligned} \tag{3.11}$$

$$0 = (\boldsymbol{e}_\beta - 2a_\beta)(n^{\alpha\beta}) - \frac{2}{3}\Theta\omega^\alpha - 2\sigma^\alpha{}_\beta\omega^\beta + \epsilon^{\alpha\beta\gamma}[\boldsymbol{e}_\beta(a_\gamma) + 2\omega_\beta\Omega_\gamma] \tag{3.12}$$

$$0 = (\boldsymbol{e}_\alpha - 2a_\alpha)(\omega^\alpha) \tag{3.13}$$

$$0 = (\boldsymbol{e}_\beta - 3a_\beta)(E^{\alpha\beta}) + 3\omega_\beta H^{\alpha\beta} - \epsilon^{\alpha\beta\gamma}[\sigma_{\beta\delta}H^\delta{}_\gamma + n_{\beta\delta}E^\delta{}_\gamma] \tag{3.14}$$

$$0 = (\boldsymbol{e}_\beta - 3a_\beta)(H^{\alpha\beta}) - 3\omega_\beta H^{\alpha\beta} + \epsilon^{\alpha\beta\gamma}[\sigma_{\beta\delta}E^\delta{}_\gamma - n_{\beta\delta}H^\delta{}_\gamma] \tag{3.15}$$

where

$${}^*R = 2(2\boldsymbol{e}_\alpha - 3a_\alpha)(a^\alpha) - \frac{1}{2}b^\alpha{}_\alpha \tag{3.16}$$

$$^*S_{\alpha\beta} = e_{(\alpha}(a_{\beta)}) + b_{\alpha\beta} - \frac{1}{3}\delta_{\alpha\beta}[\boldsymbol{e}_\gamma(a^\gamma) + b^\gamma{}_\gamma] - \epsilon^{\gamma\delta}{}_{(\alpha}(\boldsymbol{e}_{|\gamma|} - 2a_{|\gamma|})(n_{\beta)\delta}) \tag{3.17}$$

$$b_{\alpha\beta} = 2n_{\alpha\gamma}n^\gamma{}_\beta - n^\gamma{}_\gamma n_{\alpha\beta} \tag{3.18}$$

If $\omega^\alpha = 0$ the $^*R$ and $^*S_{\alpha\beta}$ correspond respectively to the trace and trace-free parts of the Ricci tensor of the hypersurface, $^*R_{\alpha\beta}$, defined by u^μ:s orthogonality. If $\omega^\alpha \neq 0$ then $^*R$ and $^*S_{\alpha\beta}$ correspond to no particular curvature tensor.

Since $\sigma_{\alpha\beta}$, $E_{\alpha\beta}$ and $H_{\alpha\beta}$ all share the properties of tracelessness, symmetry and "spatialness", we can define another set of five variables [9]:

$$\sigma_+ = -\frac{3}{2}\sigma_{11} \tag{3.19}$$

$$\sigma_- = \frac{\sqrt{3}}{2}(\sigma_{22} - \sigma_{33}) \tag{3.20}$$

$$\sigma_1 = \sqrt{3}\sigma_{23} \tag{3.21}$$

$$\sigma_2 = \sqrt{3}\sigma_{31} \tag{3.22}$$

$$\sigma_3 = \sqrt{3}\sigma_{12} \tag{3.23}$$

these enable the magnitude to be alternatively expressed as $\sigma^2 = \frac{1}{3}[(\sigma_+)^2 + (\sigma_-)^2 + (\sigma_1)^2 + (\sigma_2)^2 + (\sigma_3)^2]$. By replacing the σ by E or H, analogous definitions for these other tensors can be obtained as well.

3.2 Initial Data and Time-Reversal Symmetry

3.2.1 Simplifying the Constraint Equations

The initial data will be constructed on spacelike hypersurfaces where u^μ is orthogonal and *time-reversal symmetry* exist. Time-reversal symmetry correspond to the moment when the first order time derivative of the metric is zero, which are maximum/minimum points in the expansion (these are considered instantaneously static). Such hypersurfaces must be time-symmetric and therefore all time-dependent quantities on this hypersurface must also be symmetric around this point in time [6, 7]. This simplifies the evolution equations since any quantities changing sign under the transformation $u^\mu \to u'^\mu = -u^\mu$ must vanish (since the only value which is equal to its negative counterpart is zero). Quantities changing sign are Θ, $\sigma_{\mu\nu}$, $\omega_{\mu\nu}$, Ω^α and $H_{\mu\nu}$ [9].

For Θ, $\sigma_{\mu\nu}$ and $\omega_{\mu\nu}$ this becomes clear by using their definitions (2.28), (2.23), (2.24) since they transform as,

$$\Theta \longmapsto \Theta' = \nabla_\mu u'^\mu = -\nabla_\mu u^\mu = -\Theta \tag{3.24}$$

$$\begin{aligned}\sigma_{\mu\nu} \longmapsto \sigma'_{\mu\nu} &= \frac{1}{2}\left(\nabla_\rho u'_\mu h^\rho{}_\nu + \nabla_\rho u'_\nu h^\rho{}_\mu\right) - \frac{1}{3}\Theta' h_{\mu\nu} \\ &= -\frac{1}{2}\left(\nabla_\rho u_\mu h^\rho{}_\nu + \nabla_\rho u_\nu h^\rho{}_\mu\right) + \frac{1}{3}\Theta h_{\mu\nu} \\ &= -\sigma_{\mu\nu} \end{aligned} \tag{3.25}$$

$$\begin{aligned}\omega_{\mu\nu} \longmapsto \omega'_{\mu\nu} &= \frac{1}{2}\left(\nabla_\rho u'_\mu h^\rho{}_\nu - \nabla_\rho u'_\nu h^\rho{}_\mu\right) \\ &= -\frac{1}{2}\left(\nabla_\rho u_\mu h^\rho{}_\nu - \nabla_\rho u_\nu h^\rho{}_\mu\right) \\ &= -\omega_{\mu\nu} \end{aligned} \tag{3.26}$$

For the spatial rotation vector Ω^α defined by (2.37), it contains a derivative along u^μ and performing the transformation will change the direction of the derivative as well as change the sign of the derivative itself. This results in an overall minus sign and Ω^α must therefore vanish.

Continuing the same line of reasoning, it can be shown that $H_{\mu\nu}$ must be zero as well. To see this clearly, we need to understand how the volume element behaves under transformation. The spacetime volume element is given by $dV = \sqrt{-g}dx^0dx^1dx^2dx^3 = \eta_{0123}dx^0dx^1dx^2dx^3$ [12, 13]. Thus the spatial volume element is $\eta_{\mu\nu\rho\sigma}u^\sigma$, since $\eta_{\mu\nu\rho\sigma}u^\sigma u^\rho = 0$. The last equality occurs since contracting an anti-symmetric tensor with a symmetric tensor results in zero. During transformation, if the spatial volume element is to preserve its positive sign, the anti-symmetric tensor must transform as $\eta_{\mu\nu\rho\sigma} \mapsto -\eta_{\mu\nu\rho\sigma}$ and by (2.45), implies that $H_{\mu\nu} \mapsto -H_{\mu\nu}$ and therefore $H_{\mu\nu} = 0$ for it to be invariant. However, this is not the case for the electric part since: $E_{\mu\nu} \mapsto E'_{\mu\nu} = C_{\mu\nu\rho\sigma}(-u^\rho)(-u^\sigma) = E_{\mu\nu}$.

Inserting these results into the constraint equation (3.8) yields

$$^*R = 0 \tag{3.27}$$

Now using these results and inserting (3.27) into (3.9) results in

$$0 = -E_{\alpha\beta} + {}^*S_{\alpha\beta}. \tag{3.28}$$

Furthermore, the Ricci tensor $R_{\alpha\beta}$ is described completely by both $^*R$ and $^*S_{\alpha\beta}$ (when $\omega^\alpha = 0$), but due to (3.27), equation (3.28) is equivalent to

$$E_{\alpha\beta} = {}^*R_{\alpha\beta}. \tag{3.29}$$

All constraint equations vanish under these circumstances except (3.12), (3.14), (3.27) and (3.29). However equation (3.12) reduces to constraints on the commutation functions of the spatial frame vectors while (3.14) together with (3.29) are automatically satisfied by the contracted Bianchi identity on the 3-space. Therefore the only constraint requiring a solution is (3.27) [9].

3.2.2 Solving the Constraint Equation

Solving the constraint equations on a hypersurface with time-reversal symmetry reduces to solving equation (3.27). This has already been solved for spherical spaces, for instance in [6, 7].

I will summarize the most important points of this solution. For details, please see references [7, 6] and other references therein.

The first step towards a spherical solution of equation (3.27) is to make the following ansatz for the spatial component of the metric:

$$dl^2 = \psi^4 \hat{h}_{ij} dx^i dx^j, \tag{3.30}$$

where $\psi = \psi(x^i)$ and $\hat{h}_{ij}$ is the metric of the 3-sphere with constant curvature $\hat{R}$. We say the spatial component of the metric is conformally related to the 3-sphere with ψ^4 as the conformal factor. Equation (3.27) is then satisfied as long as ψ obeys the Helmholtz equation:

$$\hat{\nabla}^2 \psi = \frac{1}{8} \hat{R} \psi \tag{3.31}$$

where $\hat{\nabla}^2$is the Laplacian corresponding to $\hat{h}_{ij}$ [6].

Case 1: A Single Schwarzschild Mass

Since the Helmholtz equation is linear, a multisource solution can be generated by superposing several solution for single sources. This motivates a look into how the solution for a single Schwarzschild source is found.

The Schwarzschild spacetime geometry is given by

$$ds^2 = -\Big(1 - \frac{2M}{r}\Big) dt^2 + \frac{dr^2}{1 - 2M/r} + r^2(d\theta^2 + \sin^2\theta \, d\phi^2). \tag{3.32}$$

Since this geometry is spherically symmetric and static we can use isotropic coordinates. In these coordinates the Schwarzschild geometry is instead expressed as

$$ds^2 = -\Big(\frac{1 - M/2\tilde{r}}{1 + M/2\tilde{r}}\Big)^2 dt^2 + \Big(1 + \frac{M}{2\tilde{r}}\Big)^4 [d\tilde{r}^2 + \tilde{r}(d\theta^2 + \sin^2\theta \, d\phi^2)] \tag{3.33}$$

where the relationship between the two different radial coordinates is $r = \tilde{r}(1 + M/2\tilde{r})^2$ [2]. We are only interested in the spatial part (as time is constant) of (3.33) and will be denoted dl^2. Notice that if we drop $\sim$, the spatial part consists of a factor multiplied by the flat metric (in square brackets). dl^2 is then said to be conformally related to the flat metric, and the space described by dl^2 is said to be conformally flat [12]. The proportionality factor is called the conformal factor.

If now perform the transformation $\tilde{r} = K \tan(\chi/2)$ on the spatial part of (3.33) we obtain:

$$dl^2 = \frac{K^2}{4}\Big(\frac{1}{\cos\frac{\chi}{2}} + \frac{M}{2K\sin\frac{\chi}{2}}\Big)^4 [d\chi^2 + \sin^2\chi(d\theta^2 + \sin^2\theta \, d\phi^2)]. \tag{3.34}$$

The part in square brackets is the metric for the 3-sphere, thus dl^2 is also said to be conformally related to the 3-sphere. We see that (3.34) is on the same form as (3.30) and solves equation (3.31), with $\hat{R} = 6$ and

$$\psi = \sqrt{\frac{K}{2}}\Big(\frac{1}{\cos\frac{\chi}{2}} + \frac{M}{2K\sin\frac{\chi}{2}}\Big). \tag{3.35}$$

Due to the linearity of Helmholtz equation, (3.35) can be considered as a superposition of the two individually valid solutions $A(\chi) := (\sin\frac{\chi}{2})^{-1}$ and $B(\chi) := (\cos\frac{\chi}{2})^{-1}$[6].

Thus the source $2M/r$ source in (3.33) corresponds to the term in (3.35) which is proportional to $A(\chi)$ (due to M). However the term proportional to $B(\chi)$ can also be treated as a source. This becomes clear once a coordinate transformation is performed. Currently the origin lies at $\chi = 0$ which corresponds to one of the poles of the 3-sphere. Now performing the transformation $\chi \to \pi - \chi$ and the origin lies now at the antipode, in addition the roles of the two terms in (3.35) are now interchanged (i.e. $A(\chi) \to B(\chi)$ and $B(\chi) \to A(\chi)$). In addition, if the gauge parameter is set to $K = M/2$, the two sources are joined at their horizons.

It now appears as if placing one Schwarzschild source on the 3-sphere induces a mirror source at the antipode. One can therefore consider that as $\chi \to \pi$ one approaches either the asymptotic region where $\tilde{r} \to \infty$ or another Schwarzschild mass. As these two situations are geometrically identical, there is no difference between the one mass and two mass solutions, as long as the point $\chi = \pi$ can be added to the manifold [6].

Case 2: Several Schwarzschild Masses

Previously we could obtain a solution for two sources by rotating the 3-sphere. By using rotations we should be able to modify the conformal factor in such a way that it can encompass an arbitrary number of sources.

Since $A(\chi)$ is a solution, so is

$$f = \sin\frac{\chi}{2} = \sqrt{\frac{1-\cos\chi}{2}} = \sqrt{\frac{1-n\cdot n_0}{2}}. \tag{3.36}$$

Here we have used that the scalar product in euclidean four space between an arbitrary vector,

$$n = (\cos\chi, \sin\chi\sin\theta\cos\phi, \sin\chi\sin\theta\sin\phi, \sin\chi\cos\theta) \tag{3.37}$$

and one vector pointing at the north pole $n_0 = (1, 0, 0, 0)$, is given by

$$n \cdot n_0 = \cos\chi. \tag{3.38}$$

Since a coordinate transformation can be made to take any point on the 3-sphere to the north pole, equation (3.36) is then valid for any point, not only the north pole. We call this vector n_s and designates the coordinate of one source:

$$n_s = (\cos\chi_s, \sin\chi_s\sin\theta_s\cos\phi_s, \sin\chi_s\sin\theta_s\sin\phi_s, \sin\chi_s\cos\theta_s). \tag{3.39}$$

Therefore the contribution from one source is $\sqrt{M}/2f_s(\chi, \theta, \phi)$ where $f_s(\chi, \theta, \phi) = \sqrt{1 - n\cdot n_s}/\sqrt{2}$. Superposing the solutions, the conformal factor for any configuration containing N masses is [7, 6]

$$\psi(\chi,\, \theta,\, \phi) = \sum_{i=1}^{N} \frac{\sqrt{\tilde{m}_i}}{2f_i(\chi,\, \theta,\, \phi)}. \tag{3.40}$$

Thus the metric for an arbitrary number of Schwarzschild sources on a 3-sphere is the conformal factor (3.40) inserted into (3.30). The metric determinant is then given by

$$|g_{ij}| = (\psi^4)^3 \sin^4 \chi \sin^2 \theta. \tag{3.41}$$

When considering the original single source Schwarzschild solution, the parameter $\tilde{m}_i$ are equal to the Schwarzschild mass $\tilde{m}_1 = \tilde{m}_2 = M$ (with the gauge $K = M/2$). However when multiple masses are present the interpretation of $\tilde{m}_i$ will be that of an effective mass, which includes the binding energies with respect to all the other objects in the universe. We will return to this later on.

3.2.3 Simplifying the Evolution Equations

On this time-symmetric hypersurface, the evolution equations instead take the form

$$\boldsymbol{e}_0(\Theta) = 0 \tag{3.42}$$

$$\boldsymbol{e}_0(\sigma^{\alpha\beta}) = -{}^*S^{\alpha\beta} = -E^{\alpha\beta} \tag{3.43}$$

$$\boldsymbol{e}_0(\omega^{\alpha}) = 0 \tag{3.44}$$

$$\boldsymbol{e}_0(E^{\alpha\beta}) = 0 \tag{3.45}$$

$$\boldsymbol{e}_0(H^{\alpha\beta}) = -\frac{1}{2}n^{\gamma}{}_{\gamma}E^{\alpha\beta} + 3n^{(\alpha}{}_{\gamma}E^{\beta)\gamma} - \delta^{\alpha\beta}n_{\gamma\delta}E^{\gamma\delta} - \epsilon^{\gamma\delta(\alpha}(\boldsymbol{e}_{\gamma} - a_{\gamma})(E^{\beta)}{}_{\delta}) \tag{3.46}$$

$$\boldsymbol{e}_0(a^{\alpha}) = 0 \tag{3.47}$$

$$\boldsymbol{e}_0(n^{\alpha\beta}) = 0 \tag{3.48}$$

The spatial derivatives are zero since the quantities are zero everywhere on the time-symmetric hypersurface.

Initially it appears as if $\boldsymbol{e}_0(H^{\alpha\beta})$ is non-zero. However (3.46) can be written in terms of the *Cotton-York tensor*, which is defined as

$${}^*C^{\alpha\beta} := 2\epsilon^{\alpha\gamma\delta}\left(\nabla_{\delta}R^{\beta}_{\gamma} - \frac{1}{4}\delta^{\beta}_{\gamma}R_{,\delta}\right) \tag{3.49}$$

There is also an important theorem associated with this tensor already mentioned in section 2.3: for a three dimensional Riemannian space, the necessary and sufficient condition of conformal flatness is the vanishing of the *Cotton-York tensor* [14]. In our orthonormal frame where $u^{\mu} = e^{\mu}_0$, the Cotton-York tensor can be expressed as [11]

$${}^*C^{\alpha\beta} = \epsilon^{\gamma\delta(\alpha}(e_{|\gamma|} - a_{|\gamma|})({}^*S^{\beta)}{}_{\delta}) - 3n^{(\alpha}{}_{\gamma}{}^*S^{\beta)\gamma} + \frac{1}{2}n^{\gamma}{}_{\gamma}{}^*S^{\alpha\beta} + \delta^{\alpha\beta}n_{\gamma\delta}{}^*S^{\gamma\delta}. \tag{3.50}$$

(3.50) can be expressed in terms of $E_{\alpha\beta}$ by using (3.28). The resulting equation turns out to simply be (equation (3.46) is used)

$$^{*}C^{\alpha\beta} = -\boldsymbol{e}_0(H^{\alpha\beta}) \tag{3.51}$$

Since our space is conformally flat by construction, it follows from the theorem that the Cotton-York tensor vanishes and, by equation (3.51), that [9]

$$\boldsymbol{e}_0(H^{\alpha\beta}) = 0. \tag{3.52}$$

3.3 Dynamics Along Locally Rotationally Symmetric Curves

3.3.1 The Difference Between Local Rotational Symmetry and Locally Rotationally Symmetric Curves

The concept of locally rotationally symmetric (LRS) curves will be introduced here since it is very important for our theory. However, this is easily confused with the more common notion local rotational symmetry (also abbreviated LRS). However LRS curves is not identical to LRS, but the notions are very similar.

Suppose in an open neighborhood $\boldsymbol{U}$ around some point $\boldsymbol{p}_0$ there exist a set of continuous rotations which leave all curvature tensors and all its derivatives, up to 3rd order, invariant. Then the open set $\boldsymbol{U}$ is said to be locally rotationally symmetric (LRS) [18]. A set $\boldsymbol{U} \subseteq \Re^n$ is called a neighborhood of point $\boldsymbol{x} \in \Re^n$ if there exist a real number $\epsilon > 0$ such that $B_\epsilon\left(x\right) \subseteq U$, where $B_\epsilon\left(x\right) = \{\boldsymbol{y} \in \Re^n |\ |\boldsymbol{y} - \boldsymbol{x}| < \epsilon\}$. Furthermore the set $\boldsymbol{U}$ is open if $\boldsymbol{U}$ is also a neighborhood of every point within it [19]. This implies that $\boldsymbol{U}$ contains no "holes" or disjunctions of any kind.

Suppose now we have a curve $\mathbf{x} = \mathbf{x}(t)$ (where t is some parameter) along which there exists a set of rotations which leaves all curvature tensors and all its derivatives, up to 3rd order, invariant. The curve $\mathbf{x} = \mathbf{x}(t)$ is then said to be an LRS curve. This curve $\mathbf{x} = \mathbf{x}(t)$ is not an open neighborhood, and it is here the distinction lies. Whereas LRS requires invariance among all the points in a set, LRS curve is a "weaker" requirement in that it only requires invariance among points on a line. Henceforth, only the notion of *LRS curves* will be used.

3.3.2 Properties of the LRS Curve

Suppose we have a spacelike curve, and on this curve introduce an orthonormal tetrad where $u^\mu = e_0^\mu$ and set $\boldsymbol{e}_1$ parallel with the curve. Suppose there exists an n-fold symmetry under a set of discrete rotations $\boldsymbol{R}$ around the said curve, which leaves all covariantly defined quantities that are picked out by the geometry and expressed in terms of the orthonormal tetrad invariant. The rotation $\boldsymbol{R}$ transform the basis vectors as

$$\begin{aligned}
\tilde{\boldsymbol{e}}_0 &= \boldsymbol{e}_0 \\
\tilde{\boldsymbol{e}}_1 &= \boldsymbol{e}_1 \\
\tilde{\boldsymbol{e}}_2 &= \boldsymbol{e}_2 \cos\phi_m - \boldsymbol{e}_3 \sin\phi_m \\
\tilde{\boldsymbol{e}}_3 &= \boldsymbol{e}_3 \cos\phi_m + \boldsymbol{e}_2 \sin\phi_m
\end{aligned} \tag{3.53}$$

where a tilde denotes the basis vectors after transformation and $\phi_m \in [0,\, 2\pi]$. Due to symmetry assumed to exist around the curve, all covariantly defined quantities picked out by the geometry must remain identical after the transformation:

$$T^{\tilde{a}\tilde{b}\tilde{c}\dots}{}_{\tilde{d}\tilde{e}\tilde{f}\dots} = T^{abc\dots}{}_{def\dots} \tag{3.54}$$

where T is a tensor and indices with a tilde denote components in the transformed basis [9, 18]. We will see in the subsequent paragraphs how this set of discrete symmetries eventually become continuous and our curve can therefore be considered a LRS curve. This will have several interesting consequences which will simplify our evolution equations even further.

Since the rotation symmetry is discrete, there are only a discrete set of angles available for ϕ_m if equation (3.54) is to hold,

$$\phi_m = \frac{2\pi m}{n} \tag{3.55}$$

where $n \geq 3$ is an integer, and $m = 1, ..., n-1$ [9] [1].

Suppose we now choose a vector in the orthonormal basis T^α at any point $\boldsymbol{x}$ on the great circle. We will from now on ignore the time component (but remember that it still exists!). The following calculations can be treated as being performed in a synchronous coordinate system at a fixed time t. Now performing the rotation $\boldsymbol{R}$ at point $\boldsymbol{x}$ will transform the vector according to, ignoring the time component,

$$T^{\tilde{\alpha}} = \Lambda^{\tilde{\alpha}}{}_{\alpha} T^{\alpha}. \tag{3.56}$$

From (3.53) we can derive the components for the transformation matrix

$$\Lambda^{\tilde{1}}{}_2 = \Lambda^{\tilde{1}}{}_3 = \Lambda^{\tilde{2}}{}_1 = \Lambda^{\tilde{3}}{}_1 = 0 \tag{3.57}$$

$$\Lambda^{\tilde{1}}{}_1 = 1 \tag{3.58}$$

$$\Lambda^{\tilde{2}}{}_3 = \Lambda^{\tilde{3}}{}_3 = \cos\phi_m \tag{3.59}$$

$$\Lambda^{\tilde{2}}{}_3 = -\sin\phi_m \tag{3.60}$$

$$\Lambda^{\tilde{3}}{}_2 = \sin\phi_m \tag{3.61}$$

Then inserting equations (3.57) - (3.61) into (3.56)

$$\begin{cases} T^{\tilde{1}} &= T^1 \\ T^{\tilde{2}} &= \cos\phi_m T^2 - \sin\phi_m T^3 \\ T^{\tilde{3}} &= \sin\phi_m T^2 + \cos\phi_m T^3 \end{cases} \tag{3.62}$$

and, due to symmetry (see (3.54)), the equations (3.62) can be written as

$$\begin{cases} 0 &= T^1 - T^1 \\ 0 &= (\cos\phi_m - 1)T^2 - \sin\phi_m T^3 \\ 0 &= \sin\phi_m T^2 + (\cos\phi_m - 1)T^3 \end{cases} \tag{3.63}$$

which are set of $2(n-1)$ equations (since there are $n-1$ possible values of ϕ_m and there are only two equations, as the first one is redundant) constraining the possible values on T^2 and T^3 (T^1 is arbitrary). Solving for T^2 and T^3:

---

[1] In [9] $n \geq 2$ and the case when $n = 2$ is considered. However the justification is incomplete and therefore curves with only $n = 2$ can not be considered LRS.

$$\begin{cases} T^3 &= \frac{\cos\phi_m - 1}{\sin\phi_m} T^2 \qquad (i) \\ T^2 &= \frac{-\cos\phi_m + 1}{\sin\phi_m} T^3 \qquad (ii) \end{cases} \tag{3.64}$$

Inserting (3.64) (ii) into (i) yields:

$$\begin{aligned} T^3 &= -\frac{(\cos^2\phi_m - 2\cos\phi_m + 1)}{\sin^2\phi_m} T^3 \\ \Rightarrow\ 0 &= \frac{-\cos^2\phi_m + 2\cos\phi_m - 1 - \sin^2\phi_m}{\sin^2\phi_m} T^3 \\ \Rightarrow\ 0 &= 2\frac{\cos\phi_m - 1}{\sin^2\phi_m} T^3 \end{aligned} \tag{3.65}$$

And similarly for T^2:

$$0 = 2\frac{\cos\phi_m - 1}{\sin^2\phi_m} T^2. \tag{3.66}$$

Equations (3.65) and (3.66) hold true if and only if $\phi_m = 0$ or $T^2 = T^3 = 0$. However $\phi_m = 0$ means there is no rotation symmetry and therefore no spatial rotation performed on the vectors, which contradicts our initial assumption. Therefore (3.65) and (3.66) must always imply

$$T^2 = T^3 = 0. \tag{3.67}$$

This is a remarkable result! All vectors along the curve have spacelike components parallel to it, provided that there are discrete rotational symmetries. In addition, for vectors, the symmetry is not discrete anymore, it is now continuous since all vectors only have components parallel with the axis of rotation. We can therefore say that the curve is LRS [9].

Similar constraints occur for rank-2 tensors. Suppose we have instead of vector T^α, we have a rank-2 tensor $T^{\alpha\beta}$ undergoing rotation $\boldsymbol{R}$ at point $\boldsymbol{x}$ on the same curve (which is LRS):

$$T^{\tilde{\alpha}\tilde{\beta}} = \Lambda^{\tilde{\alpha}}{}_{\alpha}\Lambda^{\tilde{\beta}}{}_{\beta} T^{\alpha\beta}. \tag{3.68}$$

Due to (3.57), it follows that $T^{\tilde{1}\tilde{s}} = T^{\tilde{s}\tilde{1}} = 0$, $s = 2, 3$. Then by the invariance condition (3.54)

$$T^{1s} = T^{s1} = 0, \text{ for } s = 1, 2, 3. \tag{3.69}$$

Similarly, due to (3.58)

$$T^{\tilde{1}\tilde{1}} = T^{11}. \tag{3.70}$$

The remaining components of (3.68) are

$$\begin{aligned} T^{\tilde{3}\tilde{2}} &= \Lambda^{\tilde{3}}{}_{2}\Lambda^{\tilde{2}}{}_{2}T^{22} + \Lambda^{\tilde{3}}{}_{3}\Lambda^{\tilde{2}}{}_{2}T^{32} + \Lambda^{\tilde{3}}{}_{2}\Lambda^{\tilde{2}}{}_{3}T^{23} + \Lambda^{\tilde{3}}{}_{3}\Lambda^{\tilde{2}}{}_{3}T^{33} \\ &= \sin\phi_m\cos\phi_m T^{22} + \cos^2\phi_m T^{32} - \sin^2\phi_m T^{23} \\ &\quad - \cos\phi_m\sin\phi_m T^{33} \end{aligned} \tag{3.71}$$

$$\begin{aligned}T^{\tilde{2}\tilde{3}} &= \Lambda^{\tilde{2}}{}_{2}\Lambda^{\tilde{2}}{}_{2}T^{22} + \Lambda^{\tilde{3}}{}_{3}\Lambda^{\tilde{2}}{}_{2}T^{32} + \Lambda^{\tilde{3}}{}_{2}\Lambda^{\tilde{2}}{}_{3}T^{23} + \Lambda^{\tilde{3}}{}_{3}\Lambda^{\tilde{2}}{}_{3}T^{33} \\ &= \cos\phi_m \sin\phi_m T^{22} - \sin^2\phi_m T^{32} + \cos^2\phi_m T^{23} \\ &\quad - \sin\phi_m \cos\phi_m T^{33} \end{aligned} \tag{3.72}$$

$$\begin{aligned}T^{\tilde{2}\tilde{2}} &= \Lambda^{\tilde{2}}{}_{2}\Lambda^{\tilde{2}}{}_{2}T^{22} + \Lambda^{\tilde{2}}{}_{3}\Lambda^{\tilde{2}}{}_{2}T^{32} + \Lambda^{\tilde{2}}{}_{2}\Lambda^{\tilde{2}}{}_{3}T^{23} + \Lambda^{\tilde{2}}{}_{3}\Lambda^{\tilde{2}}{}_{3}T^{33} \\ &= \cos^2\phi_m T^{22} - \sin\phi_m \cos\phi_m T^{32} - \cos\phi_m \sin\phi_m T^{23} \\ &\quad + \sin^2\phi_m T^{33} \end{aligned} \tag{3.73}$$

$$\begin{aligned}T^{\tilde{3}\tilde{3}} &= \Lambda^{\tilde{3}}{}_{2}\Lambda^{\tilde{3}}{}_{2}T^{22} + \Lambda^{\tilde{3}}{}_{3}\Lambda^{\tilde{3}}{}_{2}T^{32} + \Lambda^{\tilde{3}}{}_{2}\Lambda^{\tilde{3}}{}_{3}T^{23} + \Lambda^{\tilde{3}}{}_{3}\Lambda^{\tilde{3}}{}_{3}T^{33} \\ &= \sin^2\phi_m T^{22} + \cos\phi_m \sin\phi_m T^{32} + \sin\phi_m \cos\phi_m T^{23} \\ &\quad + \cos^2\phi_m T^{33} \end{aligned} \tag{3.74}$$

By using (3.54), the equations (3.71)-(3.74) can be expressed as

$$\begin{aligned}0 &= \sin\phi_m \cos\phi_m T^{22} + \left(\cos^2\phi_m - 1\right) T^{32} - \sin^2\phi_m T^{23} \\ &\quad - \cos\phi_m \sin\phi_m T^{33} \end{aligned} \tag{3.75}$$

$$\begin{aligned}0 &= \cos\phi_m \sin\phi_m T^{22} - \sin^2\phi_m T^{32} + \left(\cos^2\phi_m - 1\right) T^{23} \\ &\quad - \sin\phi_m \cos\phi_m T^{33} \end{aligned} \tag{3.76}$$

$$\begin{aligned}0 &= \left(\cos^2\phi_m - 1\right) T^{22} - \sin\phi_m \cos\phi_m T^{32} - \cos\phi_m \sin\phi_m T^{23} \\ &\quad + \sin^2\phi_m T^{33} H \end{aligned} \tag{3.77}$$

$$\begin{aligned}0 &= \sin^2\phi_m T^{22} + \cos\phi_m \sin\phi_m T^{32} + \sin\phi_m \cos\phi_m T^{23} \\ &\quad + \left(\cos^2\phi_m - 1\right) T^{33} \end{aligned} \tag{3.78}$$

Due to the trigonometric identity $\cos^2\phi_m + \sin^2\phi_m = 1$, the equations (3.75) and (3.76) are identical. Thus we are no longer able to determine all the components uniquely given the available information. To remedy this, we will henceforth assume the tensor in question is symmetric, i.e. $T^{23} = T^{32}$. Later the case for an anti-symmetric tensor will be considered.

For the symmetric rank-2 tensor $T^{\alpha\beta}$ we have the following three equations describing the relationship between its components (obtained from (3.76)-(3.78))

$$\begin{cases} \cos\phi_m \sin\phi_m T^{33} & = \sin\phi_m \cos\phi_m T^{22} - 2\sin^2\phi_m T^{23} \qquad (i) \\ \sin^2\phi_m T^{22} & = \sin^2\phi_m T^{33} - 2\sin\phi_m \cos\phi_m T^{23} \qquad (ii) \\ \sin^2\phi_m T^{33} & = \sin^2\phi_m T^{22} + 2\sin\phi_m \cos\phi_m T^{23} \qquad (iii) \end{cases} \tag{3.79}$$

Provided that $\sin\phi_m \neq 0$, inserting (iii) into the LHS of (i) yields

$$\begin{aligned} \frac{\cos\phi_m}{\sin\phi_m}\left(\sin^2\phi_m T^{22} + 2\sin\phi_m\cos\phi_m T^{23}\right) &= \sin\phi_m\cos\phi_m T^{22} - 2\sin^2\phi_m T^{23} \\ \Leftrightarrow\ \cos\phi_m\sin\phi_m T^{22} + 2\cos^2\phi_m T^{23} &= \sin\phi_m\cos\phi_m T^{22} - 2\sin^2\phi_m T^{23} \\ \Leftrightarrow\ 2T^{23} &= 0 \end{aligned}$$

Inserting $T^{23} = 0$ into any of equations belonging to the system of equations (3.79) yields $T^{22} = T^{33}$. An immediate consequence is that σ_-, E_- and H_- are identically zero.

To summarize, a symmetric rank-2 tensor at an LRS curve is diagonal, with the component T^{11} arbitrary while the remaining two diagonal elements are equal $T^{22} = T^{33}$, provided that $\sin\phi_m \neq 0$. This implies that $\phi_m \neq \pi k$ (where k is a positive integer) and furthermore by looking at equation (3.55), we see why $n \geq 3$ is a necessary requirement [9].

Now turning our attention to an anti-symmetric rank-2 tensor $S^{\alpha\beta}$. If our curve is the intersection of three or more surfaces which admits reflection symmetry (two consecutive reflections correspond to a rotation)[2], then the anti-symmetric tensor must vanish. From earlier it is established already that $S^{12} = S^{13} = 0$. Now choosing that $\boldsymbol{e}_2$ lies in one of the plane of symmetry, all quantities must remain invariant under the transformation $\boldsymbol{e}_3 \mapsto -\boldsymbol{e}_3$. The component $S^{23} = -S^{32}$ then transforms into $S^{\tilde{2}\tilde{3}} = -S^{23}$. However, due to invariance, $S^{\tilde{2}\tilde{3}} = S^{23}$ and implies that $S^{23} = S^{32} = 0$. So $S^{\alpha\beta}$ is identically zero for all α and β.

To summarize the result; provided that $\boldsymbol{e}_1$ is parallel to the LRS curve, $\boldsymbol{e}_2$ lies in the plane of symmetry and is orthogonal to $\boldsymbol{e}_1$, and $\boldsymbol{e}_3$ is orthogonal to both $\boldsymbol{e}_1$ and $\boldsymbol{e}_2$, all symmetric rank-2 tensors are diagonal, where for the diagonal terms: T^{11} is arbitrary while $T^{22} = T^{33}$. Meanwhile all anti-symmetric rank-2 tensors vanishes. However, since any rank-2 tensor can be split uniquely into symmetric and anti-symmetric parts, these results hold for all rank-2 tensors [9]. This will greatly simplify our evolution and constraint equations as we will see below.

3.3.3 Consequences of the LRS Curves

The results obtained in subsection 3.3.2 for vectors and rank-2 tensors have implications for our kinematic quantities and their evolution equations. Looking at the kinematic quantities, the only non-zero quantities remaining are [9]

$$\Theta,\ \sigma_+,\ E_+ \text{ and } H_+.$$

Due to this, equation (3.10) reduces to

$$H_{\alpha\beta} = 0$$

---

[2] Two intersecting surfaces are sufficient to define a curve. However if these admit reflection symmetry, then there would only be a rotation symmetry for $\phi_m = \pi$ which is excluded. That is why the minimum number of intersecting surfaces are three, in order for there to be LRS. Thus one could say that n is the number of intersecting surfaces. I will return to this when laying out the details for my model.

and therefore implying that even H_+ vanishes.

Simplifications can also be made on the evolution equations now. Equation (3.1) is reduced to

$$\mathbf{e}_0(\Theta) = -\frac{1}{3}\Theta^2 - 2\sigma^2$$

or, alternatively, by using the quantities introduced by equations (3.19)-(3.23)

$$\mathbf{e}_0(\Theta) = -\frac{1}{3}\Theta^2 - \frac{2}{3}(\sigma_+)^2. \tag{3.80}$$

Similarly, the equations (3.2) and (3.4) are reduced to [9]:

$$\mathbf{e}_0(\sigma_+) = -\frac{1}{3}(2\Theta - \sigma_+)\sigma_+ - E_+ \tag{3.81}$$

$$\mathbf{e}_0(E_+) = -(\Theta + \sigma_+)E_+ \tag{3.82}$$

These equations can be decoupled if we define a new set of variables:

$$\mathcal{H}_{||} := \theta_{11} = \frac{1}{3}\Theta + \sigma_{11} = \frac{1}{3}(\Theta - 2\sigma_+) \tag{3.83}$$

$$\mathcal{H}_{\perp} := \theta_{22} = \frac{1}{3}\Theta + \sigma_{22} = \frac{1}{3}(\Theta + \sigma_+) \tag{3.84}$$

The second equality of both (3.83) and (3.84) follows from (2.28). The third equality in (3.84) follows from the tracelessness of $\sigma_{\mu\nu}$. Proceeding to decouple the equations result in:

$$\mathbf{e}_0(\mathcal{H}_{\perp}) + \mathcal{H}_{\perp}^2 = -\frac{1}{3}E_+ \tag{3.85}$$

$$\mathbf{e}_0(E_+) + 3\mathcal{H}_{\perp}E_+ = 0 \tag{3.86}$$

$$\mathbf{e}_0(\mathcal{H}_{||}) + \mathcal{H}_{||}^2 = \frac{2}{3}E_+ \tag{3.87}$$

Here $\mathcal{H}_{\perp}$ and $\mathcal{H}_{||}$ are the rates of expansion perpendicular to and parallel with the LRS curve respectively [9]. The three above partial differential equations are fundamentally what governs the dynamics of along the LRS curve. They will be solved in section 6.1.

Chapter 4

The Discrete-Irregular Model

So far we have seen how the equations governing dynamics look like. As they are very involved, an exact solution is expected to be just as involved. However by exploiting the opportunities offered by LRS curves, these equations are greatly simplified. What remains is to construct a model where a LRS curve exists.

4.1 The Regular Model

In simplifying the equations in the previous chapter, we used two properties of the universe (or model) which they govern. These properties need to be incorporated. In [7, 6, 9] a model where the discrete masses are regularly arranged is studied. I will briefly summarize the principal idea here, as it it works as a good stepping stone to understand my models. In addition these regular models will be frequently referred to later on.

The first property is related to the initial state: the initial hypersurface must possess time-reversal symmetry. In order for a vacuum universe (with zero cosmological constant) to have time-reversal symmetry, the curvature must be positive (a spherical universe) [2]. Therefore a (unit) 3-sphere will be chosen as it possesses positive curvature. Furthermore, if Schwarzschild masses are chosen as our sources of curvature and placed on the 3-sphere, the metric is then given by equation (3.30) together with (3.40). Thus the initial hypersurface is a 3-sphere at the moment of time-reversal symmetry.

The second property is the presence of LRS curves. To understand how these arise, we must first understand how to distribute our Schwarzschild masses. In reference [9] models where the Schwarzschild sources are regularly distributed on the 3-sphere, i.e. the distance between every source is the same, are studied. This is done by dividing the universe into lattices, or *cells*, and placing a Schwarzschild source at the center of each cell. The cells are polyhedral (all the cells must be the same polyhedron for regularity) which are thereafter used to tessellate the entire 3-sphere. There are however only a limited number of ways, *viz.* six ways, to tessellate a 3-sphere so the vertex of each polyhedron is equidistant to its nearest neighbors. These tessellation gives rise to 5, 8, 16, 24, 120 or 600 cells, and an equal number of Schwarzschild sources, depending on which polyhedral model is used [3]. See figure 4.1 for a two-dimensional analogy (see also [7, 6]). The result will be a 3-sphere populated by Schwarzschild sources, and where the distance between a source and its neighbors are the same. Due to the symmetric nature of the tessellated 3-sphere, there will be a number of curves around which there exists

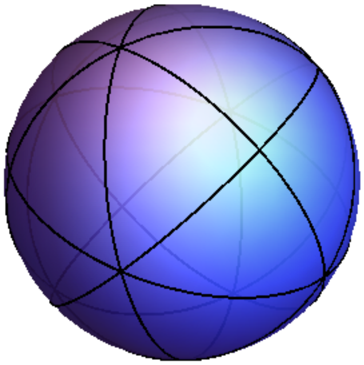

Figure 4.1: A tessellated 2-sphere provides a good analogy for its 3-sphere counterpart. Here the 2-sphere is covered by 24 cells which are isosceles triangles with angles of $\frac{\pi}{3}$ and $\frac{\pi}{2}$ radians.

discrete rotational symmetries and are therefore LRS. It is worth reminding that these models are regular.

4.2 Creating the Discrete-Irregular Model

In this thesis a model slightly different from that in [9] will be studied. As mentioned above, these models had the Schwarzschild masses regularly distributed on a 3-sphere. However, herein the model studied will be irregular, i.e. the masses will not be regularly arranged on the 3-sphere. To distinguish between the two different models, the models studied in [9] will be referred to as *regular models*, while the irregular models will be referred to as *discrete-irregular models* (abbreviated DI models), or simply as *irregular models*. The principal idea behind the DI model is similar to the regular model and will be presented below.

4.2.1 Introducing the LRS Curve

Similarly to the regular models, the DI model requires time-reversal symmetry at its initial state and an LRS curve. Time-reversal symmetry is obtained by, similarly to the regular models, place Schwarzschild masses on a 3-sphere at the moment of maximum/minimum expansion as its metric is already known and given by (3.30) together with (3.40). Thereafter an LRS curve needs to be introduced.

Analogously to the regular models, the DI model will be divided into cells. However these cells will not correspond to any tessellation of the 3-sphere, they will instead be segments resembling pieces of an orange. For instance, when cutting a two dimensional spherical object (e.g. an orange or a basket ball), as in figure 4.2, the surface of the segment formed would constitute one cell. If all segments were to of be the same size, the number of segments formed is dependent on their “equatorial width”. If we use spherical coordinates with the origin at the objects center, the segment’s boundaries would lie at particular ϕ_1- and ϕ_2-coordinates and

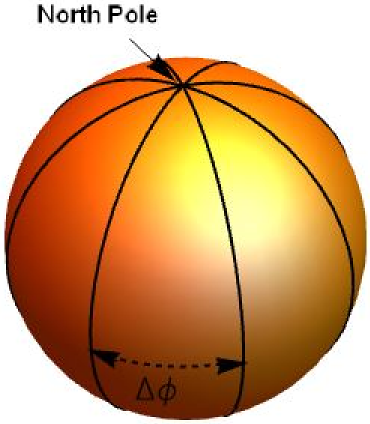

Figure 4.2: Cutting a 2-sphere into segments resembling pieces of an orange. The surface of each segment corresponds to one cell and are bounded by geodesics (black). Due to this construction all the cells touch the north and south pole. Therefore, if the cells are identical, at the poles there will be discrete rotational symmetries. The dashed line indicates the "equatorial width" $\Delta\phi$. Larger values of $\Delta\phi$ result in smaller, but more numerous, cells.

its "equatorial width" would be $\Delta\phi = \phi_2 - \phi_1$. On the 2-sphere the boundaries are geodesics passing through the sphere's poles. Each cell has two adjacent neighbors. Furthermore all cell boundaries touch the poles.

The line of reasoning for the 2-sphere is generalized for the 3-sphere. We pick an appropriate "equatorial width" $\Delta\phi$ and the place the boundaries at fixed ϕ-coordinates. However as we are now in one dimension higher than the 2-sphere case; points will become curves and curves will become surfaces. The boundaries, which are one-dimensional curves on the 2-sphere, will become spherical surfaces on the 3-sphere (this is easily realized as the 3-sphere is described by three parameters; fixing one results in a surface). In addition, the poles (points) on the 2-sphere which connects all the cells correspond to a great circle on the 3-sphere parametrized by

$$C_{LRS} = (\cos t,\, 0,\, 0,\, \sin t) \qquad \text{where } 0 \leq t < 2\pi. \tag{4.1}$$

This setup is illustrated using stereographic projection in figure 4.3.

Since all the cells share one boundary, which is the great circle C_{LRS}, this curve can be the sought after LRS curve along which we can investigate the dynamics, provided that the contents of each cell is distributed in such a manner that a discrete rotational symmetry arises around the curve.

I have chosen to distribute the matter across the cells through reflection. Suppose we have one starting cell with some arbitrary configuration of masses. The remaining cells are empty. To fill these, I simply mirror the configuration in the starting cell to the neighboring cells by using the boundary surface as the surface of reflection. Thereafter, repeat the process with the new cells to fill up any remaining empty neighbors. Performing all reflections for all cells, one will notice that we will arrive at our starting configuration. This is easiest performed

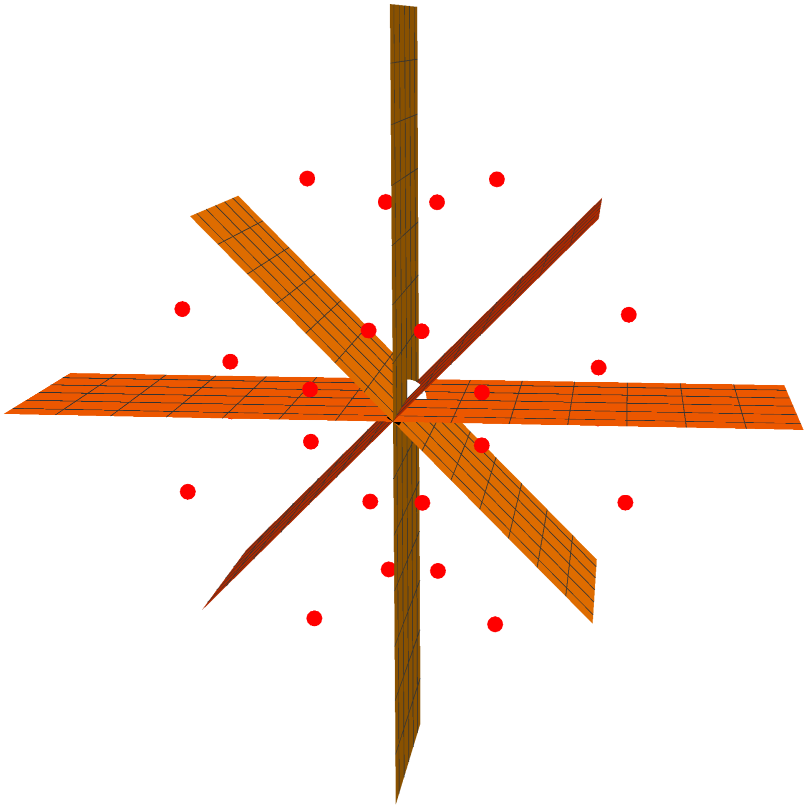

Figure 4.3: Stereographic projection of the DI model. The orange colored planes are the cell boundaries and extend all the way to infinity (where the north pole lies). Since there are four surfaces intersecting each other, $n = 4$ in equation (3.55). The large white dot in the middle shows the location of the south pole (visible at the center). The red dots are properly distributed masses (three in each cell). Notice that every cell is a mirror image of its neighbor. The LRS curve is the line where all cell boundaries intersect and stretches to infinity. On the 3-sphere, this curve is a great circle.

in the stereographic projection, since the cell boundaries are then planes in the stereographic projection. Thus every cell is a reflection of its neighbor; there is a reflection symmetry.

Furthermore there will also be discrete rotational symmetries. Reflecting one configuration, or object, once across a surface will yield its mirror image on the opposite side. If the object is chiral, i.e. the object is distinguishable from its mirror image, the image and its mirror image will not be superimposable. Therefore it is impossible to rotate the image so that it transforms into its mirror image. However, reflect the mirror image across another (or same) surface and we will obtain the mirror image of the mirror image, i.e. the original image, albeit at a (possibly) new location. The original image can be rotated so that it transforms into this new image. Neighboring cells are mirror images of each other, while the neighbor's neighbor is the original object rotated $2\Delta\phi$ around the LRS curve.

To summarize the procedure, suppose we have n intersecting surfaces resulting in $2n$ empty cells (as in figure 4.3). Each cell is equally large determined by their "equatorial width" $\Delta\phi$. Label each cell C_i, where $1 \leq i \leq 2n$. Then fill one starting cell C_1 with some configuration of Schwarzschild masses and reflect them across the cell boundaries into the neighboring cell C_2. Then repeat the procedure for C_2, reflect its contents across the cell boundary into cell C_3 and so forth, until all $2n$ cells are filled. Since neighboring cells are mirror images and the configuration is generally chiral (if not, then the curve is LRS since all the cells are the same but rotated), C_1 can not be transformed by a rotational operation into C_e, where $e = 2, 4, ..., 2n-2, 2n$. By similar reasoning, C_2 can not be transformed into C_f for any rotation, where $f = 1, 3, ..., 2n-1$. Since the mirror image of a mirror image is the original image, this implies that C_1 can be rotated into C_f while C_2 can be rotated into C_e. We therefore have a discrete rotational symmetry around the surface intersection, with the angles given by the expression (3.55), where n is the number of intersecting surfaces.

4.2.2 Distributing Masses Irregularly inside a Cell

In the previous subsection, we saw how LRS arises in the DI model. However, this was independent of how the configuration looked *inside* the starting cell. That is where irregularity can be introduced. As long as the content was properly reflected into neighboring cells, LRS would arise. The question remaining is, by what means should the masses be distributed inside the starting cell? A simple method which would generate varied irregular configurations would be through randomization.

Randomly distributing points on a sphere is deceptively tricky. For instance, on a 2-sphere picking a random coordinate from $\theta \in [0, \pi]$ and $\phi \in [0, 2\pi[$, will generate a non-uniform distribution where points cluster around the poles. That is because the surface area element $d\Omega = \sin\theta d\theta d\phi$ is dependent on θ [20]. This is also the case for the 3-sphere, where the surface volume element $dV = \sin^2\chi \sin\theta d\chi d\theta d\phi$ is dependent on χ and ϕ. Therefore a particular algorithm must be employed to generate uniform distributions, where we can expect any small area on the sphere to contain on average an equal number of points.

There are several algorithms that offers a random but uniform distribution on the 2-sphere. One is due to George Marsaglia [21][1]. First generate V_1 and V_2 independently and uniformly on $[-1, 1]$ until $S = V_1^2 + V_2^2 < 1$. Then the point (x, y, z) is uniformly distributed on the 2-sphere, where

$$x = 2V_1(1-S)^{\frac{1}{2}}, \qquad y = 2V_2(1-S)^{\frac{1}{2}}, \qquad z = 1-2S. \tag{4.2}$$

This algorithm can be generalized to the 3-sphere and is used to generate an irregular mass configuration within our starting cell. First choose two pairs of points, (V_1, V_2) and (V_3, V_4), independent and uniformly on $[-1, 1]$. Furthermore, the points must also satisfy $S_1 = V_1^2 + V_2^2 < 1$ and $S_2 = V_3^2 + V_4^2 < 1$. Then the following point is uniform on the unit 3-sphere [21, 22]:

$$w = V_4\sqrt{\frac{1-S_1}{S_2}}, \qquad x = V_1, \qquad y = V_2, \qquad z = V_3\sqrt{\frac{1-S_1}{S_2}}. \tag{4.3}$$

Unfortunately, this algorithm does not generalize to higher dimensions than three [22].

---

[1] Be aware that Marsaglia´s and mine convention when naming spheres differ. In Marsaglia's paper his 4-sphere corresponds to my 3-sphere, whilst his 3-sphere corresponds to my 2-sphere.

4.2.3 Specifications of the DI Models Studied in this Thesis

In the previous subsections, I have presented how a DI model is constructed. In this thesis however, only the time evolution of the DI model with eight (equally large) cells is studied with the different mass counts of 8, 16, 24, 120 and 600 sources (corresponding to 1, 2, 3, 15 and 75 masses per cell respectively). The reason for these specific number of masses is that it enables comparison with the regular models in [9].

The reasoning behind using eight cells is not as straight forward. Fewer cells are more desirable, since it is simpler. Thus the smallest number of cells is six (since $n \geq 3$ and corresponds to the number of intersecting cell boundaries). However it is not possible to distribute 8 and 16 sources equally among six cells and I would therefore lose two opportunities to compare with regular models. The second lowest cell count is eight, which corresponds to four intersecting surfaces. Thus the cell boundary surfaces lie at $\phi = \frac{\pi}{4}m$, where $m = 0,\ 1, ...,\ 7$.

However in this thesis, the initial conditions for a four-cell DI model will be investigated just for comparison. The dynamics for this model cannot be investigated since the curve formed by the intersection of cell boundaries is not LRS ($n = 2$ in this case).

Chapter 5

Characteristics of the Initial State

This chapter contains information about the initial hypersurface: the mass of the sources, the length of the LRS curve and the initial curvature along it.

5.1 Proper Mass

There are two concepts of mass dealt with in this thesis: *proper mass* m_p and *effective mass* $(m_i)_{\text{eff}}$. Proper mass is the object's actual mass as measured locally by an observer. Effective mass however is defined to be equal to the mass parameter, $(m_i)_{\text{eff}} := \tilde{m}_i$, and contains all the binding energies due to other objects as well as the proper mass [6]. The relationship between the two masses can be crudely depicted by $m_{\text{eff}} \approx m_p + E_b$, where E_b is the binding energy due to other objects. Since E_b is a negative quantity (recall that gravitational potential energy in Newtonian physics is negative), the effective mass is always smaller than the proper mass [23].

Calculating proper mass is tricky however. Brill and Lindquist [23] calculate the proper masses[1] in asymptotically flat space by comparing their metric with the Schwarzschild case infinitely far away from the mass under investigation. This means that, to measure proper mass of a specified object requires regions which are infinitely far away from any other mass. This is however not possible in closed spaces, such as the DI model [6], and therefore an analogy to the Brill-Lindquist method will be employed.

Suppose there is a Schwarzschild mass at the north pole $\chi = 0$ and its proper mass is desired. Then the proper mass will be defined so that the geometry of space takes the form of the transformed Schwarzschild geometry for a single black hole (see equation (3.35) with $K = m_p/2$) as $\chi \to 0$ [6, 7]

$$\lim_{\chi\to 0} \frac{\sqrt{m_p}}{2}\left(\frac{1}{\cos\frac{\chi}{2}} + \frac{1}{\sin\frac{\chi}{2}}\right) = \frac{\sqrt{m_p}}{2} + \frac{\sqrt{m_p}}{\chi} + O(\chi). \tag{5.1}$$

Now performing the same Laurent expansion but for a general conformal factor (see equation (3.40)) yields:

$$\lim_{\chi\to 0} \sum_{i=1}^{N} \frac{1}{2}\frac{\sqrt{(m_i)_{\text{eff}}}}{f_i(\chi,\theta,\phi)} = \frac{2c_1}{\chi} + c_2 + O(\chi) \tag{5.2}$$

---

[1] In Brill and Lindquist, their bare mass corresponds to my proper mass.

where c_1 and c_2 are arbitrary constants defined by expansion (5.2). By comparing the two expansions (5.1) and (5.2), the proper mass can be calculated as

$$m_p = 4c_1c_2. \tag{5.3}$$

This gives the proper mass of a source located at the north pole $\chi = 0$. It can be shown that the proper mass defined this way, corresponds to the mass at the other end of an Einstein-Rosen bridge [6, 23]. Notice that the proper mass is dependent on the position of all other masses.

To obtain the proper mass for another source, the entire coordinate system is rotated such that the source of interest lies at the north pole. This is then repeated for the remaining sources. Note that this must be performed after all sources are distributed in each cell.

Rotation can be performed by using the 4x4-rotation matrices, such as:

$$A = \begin{pmatrix} 1 & 0 & 0 & 0 \\ 0 & \cos\phi & \sin\phi & 0 \\ 0 & -\sin\phi & \cos\phi & 0 \\ 0 & 0 & 0 & 1 \end{pmatrix}$$

$$B = \begin{pmatrix} 1 & 0 & 0 & 0 \\ 0 & \cos\theta & 0 & -\sin\theta \\ 0 & 0 & 1 & 0 \\ 0 & \sin\theta & 0 & \cos\theta \end{pmatrix}$$

$$C = \begin{pmatrix} \cos\chi & 0 & 0 & \sin\chi \\ 0 & 1 & 0 & 0 \\ 0 & 0 & 1 & 0 \\ -\sin\chi & 0 & 0 & \cos\chi \end{pmatrix}$$

By operating on a source with Cartesian coordinates $X = (w,\, x,\, y,\, z)^T$, then $(1,\, 0,\, 0,\, 0)^T = CBAX$ provided that χ, ϕ and θ are the hyperspherical coordinates of X. A new expansion (in the new rotated coordinate system) is performed after each rotation. This can be time consuming for models containing many sources, however due to reflection symmetry, only the proper mass of one cell needs to be calculated. The remaining sources will have the proper mass of their corresponding source in the starting cell.

The reader might wonder, why bother with proper mass? This is a valid point, particularly since the DI metric only requires the effective mass (see the conformal factor given by equation (3.40)). The proper mass as defined here, is the mass measured by an observer *locally.* Whenever we perform experiments to measure mass, they are performed locally and therefore gravitational interaction energies can be neglected. This is also how mass is treated in the FLRW model. The mass in a small volume is measured locally and thereafter integrated over space to yield the total mass content. Therefore, the concept of proper mass corresponds well to how mass is treated in the FLRW model which allows for comparisons between the FLRW model and the DI model.

As we now have two concepts of mass, at least one of them needs to be fixed by some criteria. A model containing equally massive sources, i.e. sources with the same proper mass, would be the conceptually simpler model and is typically the first case to investigate. However, fixing the proper mass to a specific value implies that the effective mass will vary for each source.

m_p/m_{eff}
75.8
15.5

Table 5.1: The two different mass ratios found in the four-cell model containing eight sources (two sources in each cell).

Calculating the effective mass from proper mass is difficult, it is easier to fix the effective masses for all sources at one specific value and calculate the proper mass from this. In this thesis, the effective value for *all* sources is set to the value $(m_i)_{\text{eff}} = 1$ for all i. From the effective mass, the proper mass is then calculated as described earlier for each source. Thus a distribution of different proper masses is found in these models.

5.1.1 Proper Mass Distribution in the Four-Cell DI Model

In this subsection, we will take a look at how the proper mass m_p is distributed for the DI model consisting of four cells, which will be referred to as the four-cell model. Although, we do not have the tools to investigate the dynamics of the four-cell model, we can still make useful initial comparisons with the eight-cell model (the DI model consisting of eight cells). Since the choice of setting *all* effective masses $(m_i)_{\text{eff}}$ to 1 is arbitrary (we might as well have chosen the value 2, 5 or any other real number) the following figures will display the *ratio* of proper mass to effective mass, which is independent of the value of effective mass given to all sources [6] (this is only true as long as the effective mass of each source is the same).

If we start off by looking at table 5.1 which displays the ratios found among eight sources distributed in a four-cell model. Notice that only two values of proper masses are present! This is due to reflection symmetry as previously mentioned. Only two sources are placed out independently of each other. The remaining six sources are not independent, their positions are predetermined once the first two are picked due to reflection. Thus the amount of different proper mass values expected to be found is equal to the number of sources placed in the starting cell, in the case of eight sources, this is two ($sources/cells = 8/4 = 2$). Therefore, to study the mass distributions in an entire configuration in a DI model, it is sufficient to study the mass distribution in one cell. Henceforth, all mass ratios will be solely collected from one single cell.

The values provided in table 5.1 only provide the mass ratios for one random, but given, configuration. Since in this work we are interested to study several different types of randomly generated configurations, we need to see how this mass ratio varies for different configurations. This data is presented in figure 5.1 as a histogram. Here the mass ratios of 500 randomly generated 8-source configurations are presented (this amounts to 1000 mass ratios).

For 16- and 24-source configurations, there are four respectively six sources in each cell. Figure 5.2 presents the ratio for the 400 randomly generated 16-source configurations and 300 randomly generated 24-source configurations. Notice how similar these distributions are to each other.

By looking at histograms in figures 5.1, 5.2 and 5.3, one realizes there is a clear minimum ratio. This is particularly visible in figure 5.3, where the minimum ratio lies at $\sim 10^{2.2}$ for 120 sources or $\sim 10^{2.9}$ for 600 sources. The reason for this is not difficult to understand. The proper mass must be equal to or greater than the effective mass and therefore in the absence of

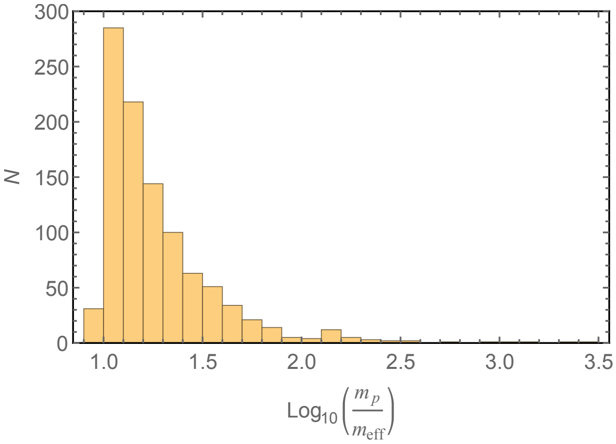

Figure 5.1: Mass ratios (four-cell DI model) for 500 randomly generated eight-source configurations.

Number of Sources	Median $\left(m_p/m_{\mathrm{eff}}\right)$	$\frac{\lvert\mathrm{LQU}-\mathrm{Median}\rvert}{\mathrm{Median}}$	$\frac{\lvert\mathrm{UQU}-\mathrm{Median}\rvert}{\mathrm{Median}}$
8	15	0.25	0.76
16	29	0.16	0.39
24	29	0.15	0.41
120	206	0.054	0.086
600	1021	0.025	0.033

Table 5.2: The median ratios for each type of four-cell configuration. As a measure of the distribution's spread (two rightmost columns), the lower and upper QU (LQU and UQU respectively) are used and calculated as indicated in the table.

interactions the proper mass equals the effective mass. Thus the effective mass sets the lower limit.

However this could only occur if all the sources were infinitely far away from each other, a scenario which is not possible in our closed model. Therefore the smallest possible proper mass is attained when one source is placed as far away from the other sources as possible. This is however a low probability event, as it requires the remaining sources to be distributed non-uniformly using a random uniform distribution. An analogy on a 2-sphere would be a configuration of N sources where $N-1$ sources are placed infinitesimally close to the north pole while the single remaining source is placed at the south pole. That single source at the south pole would acquire the lowest proper mass in an N-source configuration. Since such non-uniform distributions are unlikely to occur, such small mass ratios will be rare. In addition the sources placed infinitesimally close to each other will have their proper mass go to infinity. That is probably the case for the long trailing tail of small bars to the left in each histogram. These arise since the upper limit on the proper mass is very large and occurs when the sources are so close that their horizons overlap.

The proper mass distributions are highly skewed due to the presence of a small lower limit

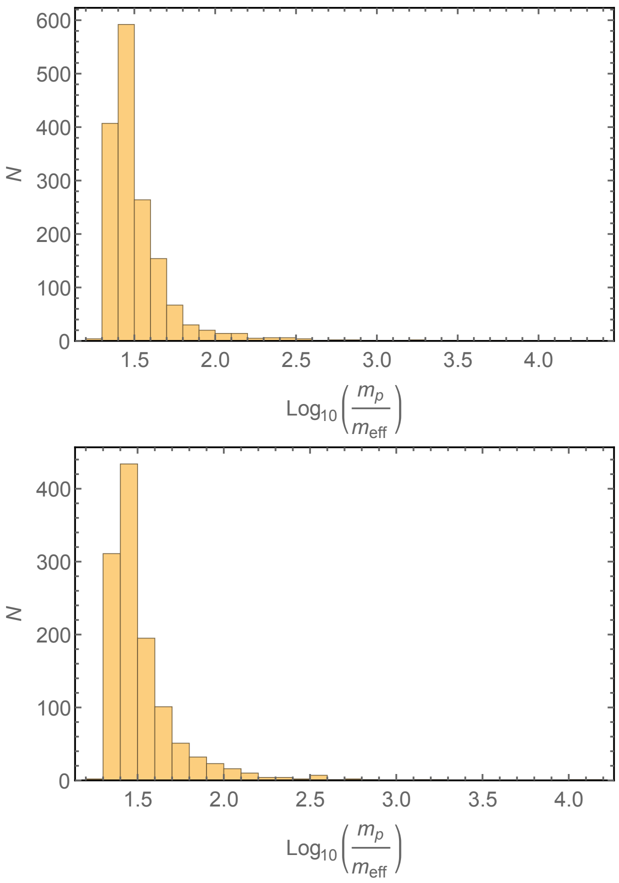

Figure 5.2: Top: mass ratios (four-cell DI model) for 400 randomly generated 16-source configurations. Bottom: mass ratios (four-cell DI model) for 300 randomly generated 24-source configurations.

on the proper mass while the upper limit is very large. Therefore using the mean and standard deviation to describe the distribution is ill-conceived as the standard deviation will be several times larger than the mean. An alternative way to represent the distribution is to use the median together with the lower and upper *quintile* (QU). The median indicates the value at which half of all the measurements yield values below the median and the remaining half yield measurements above the median. The lower QU (LQU) indicate the value at which a fifth of all measurements lie below while the upper QU (UQU) indicate the value at which 4/5th of all the measurements lie below. Thus 60% of all the measurements lie between the upper and lower QU, with the median somewhere between. These are presented in table 5.2 for the distributions in figures 5.1, 5.2 and 5.3.

From table 5.2 it is clear that the median is closer to the lower QU, indicating the asymmetry of the distributions. This is reflected in the figures 5.1, 5.2 and 5.3 by the concentration of values to the left hand side of the histograms, with some values spread out over a large range to the

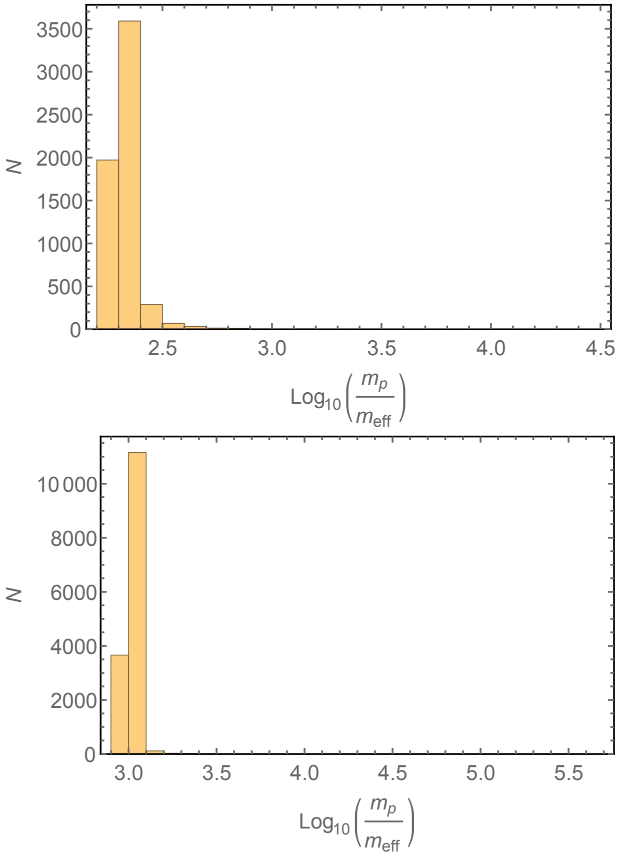

Figure 5.3: Top: mass ratios (four-cell DI model) for 200 randomly generated 120-source configurations. Maximum at $\log_{10}(m_p/m_{\text{eff}}) \sim 4.4$. Bottom: mass ratios (four-cell DI model) for 100 randomly generated 600-source configurations. Maximum at $\log_{10}(m_p/m_{\text{eff}}) \sim 5.7$.

right, thus creating the asymmetry.

Overall the distribution spread decreases as the number of sources increases, except between 16 and 24 sources which are very similar. The reason for the overall decrease in spread is maybe because the models are moving towards a more uniform case as the number of sources increases.

The values in table 5.2 are also plotted in figure 5.7 together with the ratios for the regular configurations (see [7, 6]) and the eight-cell model.

5.1.2 Proper Mass Distribution in the Eight-Cell DI Model

In this subsection, we take a look at the mass ratios for the eight-cell model. It will be treated similarly to the previous four-cell case. Figure 5.4 showcases the ratios for the different eight-cell configurations, while table 5.3 lists the median and QU.

First, we see that as the source count increases the spread decreases similarly to the four-cell case. The reason is possibly the same.

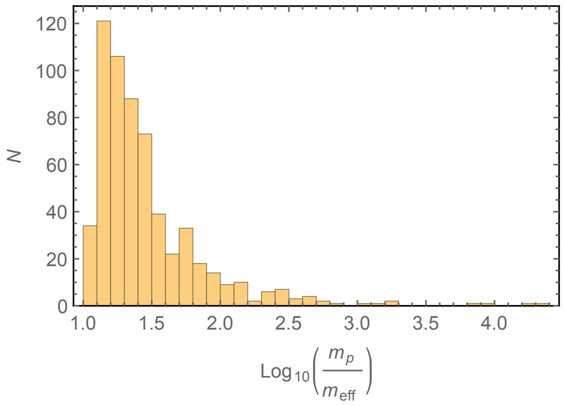

Figure 5.4: Mass ratios (eight-cell DI model) for 600 randomly generated 8-source configurations.

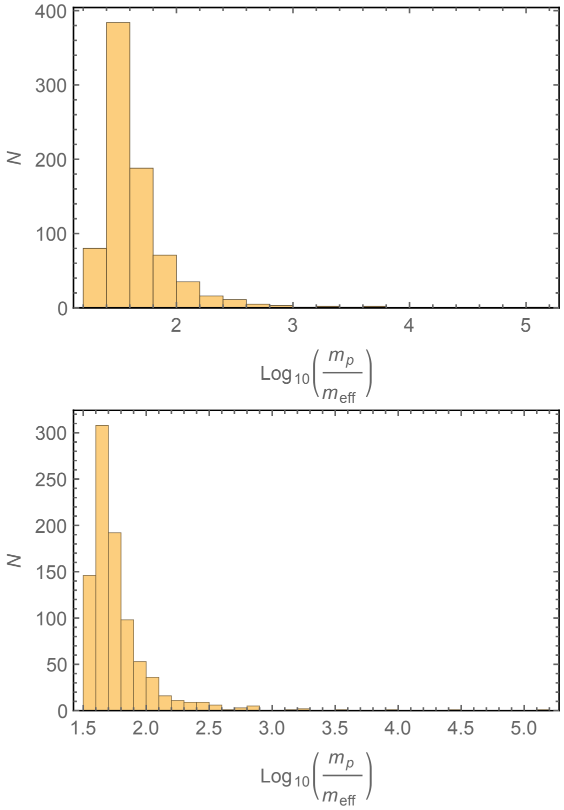

Figure 5.5: Top: mass ratios (eight-cell DI model) for 400 randomly generated 16-source configurations. Bottom: mass ratios (eight-cell DI model) for 300 randomly generated 24-source configurations.

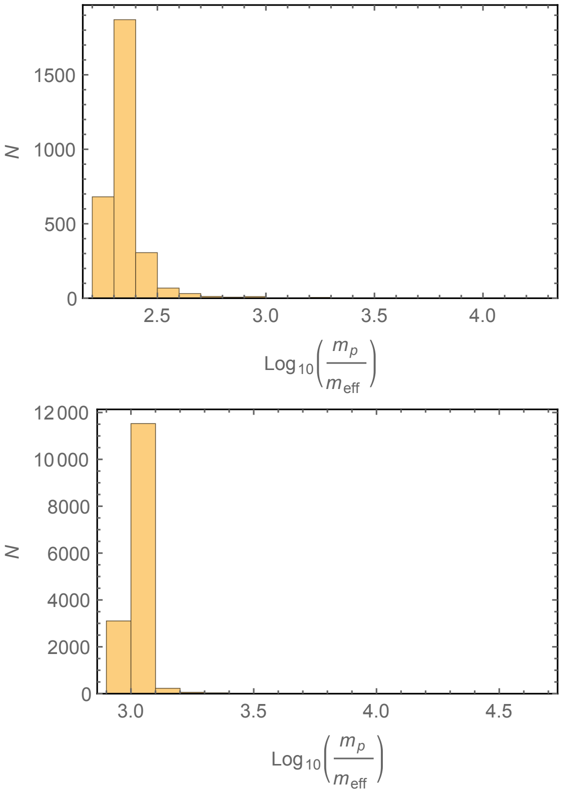

Figure 5.6: Top: mass ratios (eight-cell DI model) for 200 randomly generated 120-source configurations. Bottom: mass ratios (eight-cell DI model) for 200 randomly generated 600-source configurations.

Number of Sources	Median $\left(m_p/m_{\mathrm{eff}}\right)$	$\frac{\lvert\mathrm{LQU}-\mathrm{Median}\rvert}{\mathrm{Median}}$	$\frac{\lvert\mathrm{UQU}-\mathrm{Median}\rvert}{\mathrm{Median}}$
8	22	0.34	1.2
16	37	0.24	0.64
24	50	0.18	0.50
120	213	0.069	0.13
600	1031	0.031	0.043

Table 5.3: The median and spread for each type of eight-cell configuration.

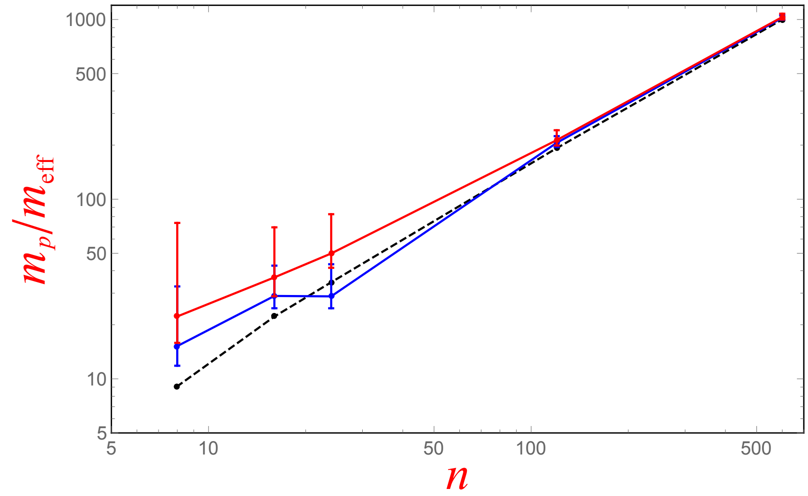

Figure 5.7: Median mass ratios plotted against the number of sources n using logarithmically scaled axes. The blue curve displays the median mass ratios for the four-cell DI model (see table 5.2), while the red curve are the corresponding values for the eight-cell DI model (see table 5.3). The error bars located above the median indicate the UQU values and the error bars below indicate the LQU values. The black dashed curve displays the regular ratios found in [6], for which, the ratio is not a median but an exact value identical for all sources.

Second, the median ratios increase for both models. This is evident from figure 5.7, where the median ratio for both the four-cell (blue) and the eight-cell (red) are plotted together with the regular models from [6] (dashed black). Initially both the four- and eight-cell models generally result in sources with mass ratios larger than the regular case. At 24 sources the four-cell median does not increase and therefore finds itself below the regular case, as indicated as a plateau on the blue curve. This is particularly odd since the effect is not present in the eight-cell model.

At 120 sources, all three curves nearly converge unto the same point (from tables 5.2, 5.3 and [6] we see a difference, but it is small). Overall, there is decrease in ratio as number of sources increases, and it is larger for lower numbers.

Surprising is that the eight-cell DI model yields mass ratios which are further away from the regular case than the four-cell one. The opposite is expected (particular when only 8 sources are present) since more cells result in more symmetry and should therefore approach the regular case.

5.2 Global Scale of the DI Model

A measurement of global scale of these models is to measure the length of some appropriate curve related to the model size. In the FLRW model, any curve can be chosen due to homogeneity and isotropy of the model. For the discrete models, this needs to be handled with care, as the length of curves will depend on its particular position. Furthermore, as each configuration is randomly generated, the length of the curve is expected to differ. In [7, 6], two measures of scale is proposed for their regular discrete models:

1. The line-element, *dl*, of a curve at positions farthest away from all masses.
2. The length of an edge of a cell.

Both suggestions identifies two different types of preferred curves in their models. As for my irregular models, the first approach is unsuitable as that curve will be different with every new randomly generated configuration. A more suitable approach would be to measure the cell edge which lies at the intersection of all the cell boundaries. In addition this curve is a great circle and LRS, described by the parameter χ and $\theta = 0$ or π. The LRS curve is therefore a suitable measurement of scale in the DI models.

5.2.1 Length of the LRS Curve

In the DI Model

The length of an arbitrary curve in spacetime is given by[13]

$$L = \int_{\lambda_0}^{\lambda_1} \left| g_{\alpha\beta} \frac{\mathrm{d}x^\alpha}{\mathrm{d}\lambda} \frac{\mathrm{d}x^\beta}{\mathrm{d}\lambda} \right|^{1/2} d\lambda \tag{5.4}$$

By using the χ as the great circle's coordinate, the length is then given by

$$L_0 = \int_0^\pi |g_{\chi\chi}|^{1/2} \, d\chi \, |_{\theta=0} + \int_0^\pi |g_{\chi\chi}|^{1/2} \, d\chi \, |_{\theta=\pi}$$

Due to symmetry however, a shorter expression which yields the same result is[2]

$$L_0 = \int_0^{2\pi} |g_{\chi\chi}|^{1/2} \, d\chi \, |_{\theta=0} \tag{5.5}$$

Since the configuration is randomized, performing this calculation several times will generate a distribution of lengths for each set number of sources and must be treated statistically. For the DI model, this means the great circle length is given by

$$L_0^{discrete} = \int_0^{2\pi} (\psi(\chi, \theta, \phi))^2 \, d\chi \, |_{\theta=0} \tag{5.6}$$

This is a simple looking expressions, however the conformal factor (and therefore, also the integral) grows rapidly in complexity as more sources are added.

---

[2] θ can also be set to π. The result is the same, only the direction in which the integration is performed is then the opposite.

In the FLRW Model

The length of the same great circle in the FLRW model requires its respective spatial line-element which is given by:

$$dl^2 = \frac{16M^2}{9\pi^2}(d\chi^2 + \sin^2\chi\, d\theta^2 + \sin^2\chi\, \sin^2\theta\, d\phi^2) \tag{5.7}$$

where M is the total amount of proper mass in the universe. This assumes that the closed space has a positive curvature, is dust filled and at maximum expansion.

This can be proved by starting from the general line element for the FLRW model

$$ds^2 = -f(t)dt^2 + a^2(t)\left(\frac{dr^2}{1-kr^2} + r^2 d\theta^2 + r^2\sin^2\theta d\phi^2\right) \tag{5.8}$$

where $f(t)$ is a free function[3], $a(t)$ is the scale factor and $k = -1, 0, +1$ depending on the curvature of the universe, whether it is hyperbolic, flat or spherical respectively.

Inserting the FLRW metric and the stress-energy tensor for a perfect fluid into the Einstein field equations

$$G^{\mu\nu} = 8\pi T^{\mu\nu} \tag{5.9}$$

we can derive the two equations governing the dynamics of the FLRW universe. The first equation is

$$2\frac{\ddot{a}}{a} + \left(\frac{\dot{a}}{a}\right)^2 + \frac{k}{a^2} = -8\pi p \tag{5.10}$$

while the second equation is known as the *Friedmann equation*

$$\frac{1}{f}\frac{\dot{a}^2}{a^2} = \frac{8\pi}{3}\rho - \frac{k}{a^2} \tag{5.11}$$

A dot represents here the derivative with respect to time t, $p = p(t)$ is the pressure and $\rho = \rho(t)$ is the energy density. Since the universe we are interested in is spherical, I will henceforth set $k = +1$.

One can already now find the scale factor at maximum expansion. Since we have time-reversal symmetry, or equivalently: maximum expansion in the spherical FLRW model, we can set $\dot{a} = 0$. The Friedmann equation is then simplified and can be solved for a:

$$a^2 = \frac{3}{8\pi\rho}. \tag{5.12}$$

Now the energy density ρ needs to be found explicitly at the moment of maximum expansion.

The density is defined as $\rho = M/V$, where M is the total mass of the model/universe and V is the volume. We can start by calculating the volume. The volume element around any arbitrary point is $|g|^{\frac{1}{2}}\mathrm{d}^n x$ where g is the metric determinant and n is the dimension of the manifold [12]. Since the spatial volume is of interest, we only need to take the spatial part of the metric (5.15) and integrate:

---

[3] This is simply a time-scaling factor, in most textbooks this is set to 1.

$$V = \int\limits_{\chi=0}^{\pi} \int\limits_{\theta=0}^{\pi} \int\limits_{\phi=0}^{2\pi} |a^6(t) \sin^4 \chi \sin^2 \theta|^{\frac{1}{2}} \, \mathrm{d}\chi \mathrm{d}\theta \mathrm{d}\phi = 2\pi^2 a^3(t). \tag{5.13}$$

Now setting $t = t_0$ in (5.13) (this gives the volume of the universe at maximum expansion) and using the definition of density together with expression (5.12) gives the scale factor in terms of total mass at maximum expansion

$$a(t_0) = \frac{4M}{3\pi}. \tag{5.14}$$

The next step is to transform the spatial part of the FLRW line element in terms of the hyperspherical coordinates of the 3-sphere. That is done through the substitution $r = \sin\chi$ for $k = +1$. Differentiating gives $dr = \cos\chi \, d\chi = \sqrt{1-r^2}\, d\chi$. Thereafter substituting $r \mapsto \sin\chi$ and its appropriate differentials into (5.8) gives the new line element

$$ds^2 = -f(t)dt^2 + a^2(t)(d\chi^2 + \sin^2\chi d\theta^2 + \sin^2\chi \sin^2\theta d\phi^2) \tag{5.15}$$

for the FLRW model. The spatial part of the line element consists of the line element for a 3-sphere multiplied by $a^2(t)$. Then inserting (5.14) into (5.15) gives the line element at maximum expansion, as was to be shown. See also [7, 6, 4].

Finally the length of the same curve in the FLRW model is given by inserting equation (5.7) into (5.5), which results in $L_0^{FLRW} = 8M/3$. Note this implies that the size of the FLRW model grows as the mass inside increases.

We can now employ these tools to measure the length of our LRS curve. These will be presented as the ratio $L_0^{discrete}/L_0^{FLRW}$, where $L_0^{discrete}$ is the length of the LRS curve in the discrete models with total proper mass M, while L_0^{FLRW} is the corresponding curve length in the FLRW model with the same total mass M. We will study this for both the four-cell and eight-cell models before comparing to the regular models of [7, 6].

5.2.2 Four-Cell Great Circle Lengths

Figure 5.8 presents the measured great circle lengths as the ratio $L_0^{discrete}/L_0^{FLRW}$. The measurements were done by measuring the total proper mass and length of the LRS curve for a randomly generated configuration and then repeat the same measurements for new random configuration. This was repeated as many times as desired. However, due to the amount of time it takes to calculate proper masses for each source, the configurations with more sources were measured fewer times. Even so, the higher source count configurations tend to have a more distinct peak in their histograms. The medians together with the lower and upper quintile for each distribution are found in table 5.4, since these distributions exhibit asymmetrical features.

Figures 5.9, 5.10 and 5.11 depicts some examples of how configurations may look like for different length ratios: one with a very small ratio, one with a ratio around the median and, finally, one with a very large ratio. These are projections of stereographic projections, the z-axis (parallel to the LRS curve) points out from the paper in these diagrams. Details of each figure is given in their respective figure text. The 120- and 600-source cases are omitted, due to the sheer number of points. The general behavior is that configurations with very small ratios have points very close to the reflection surface.

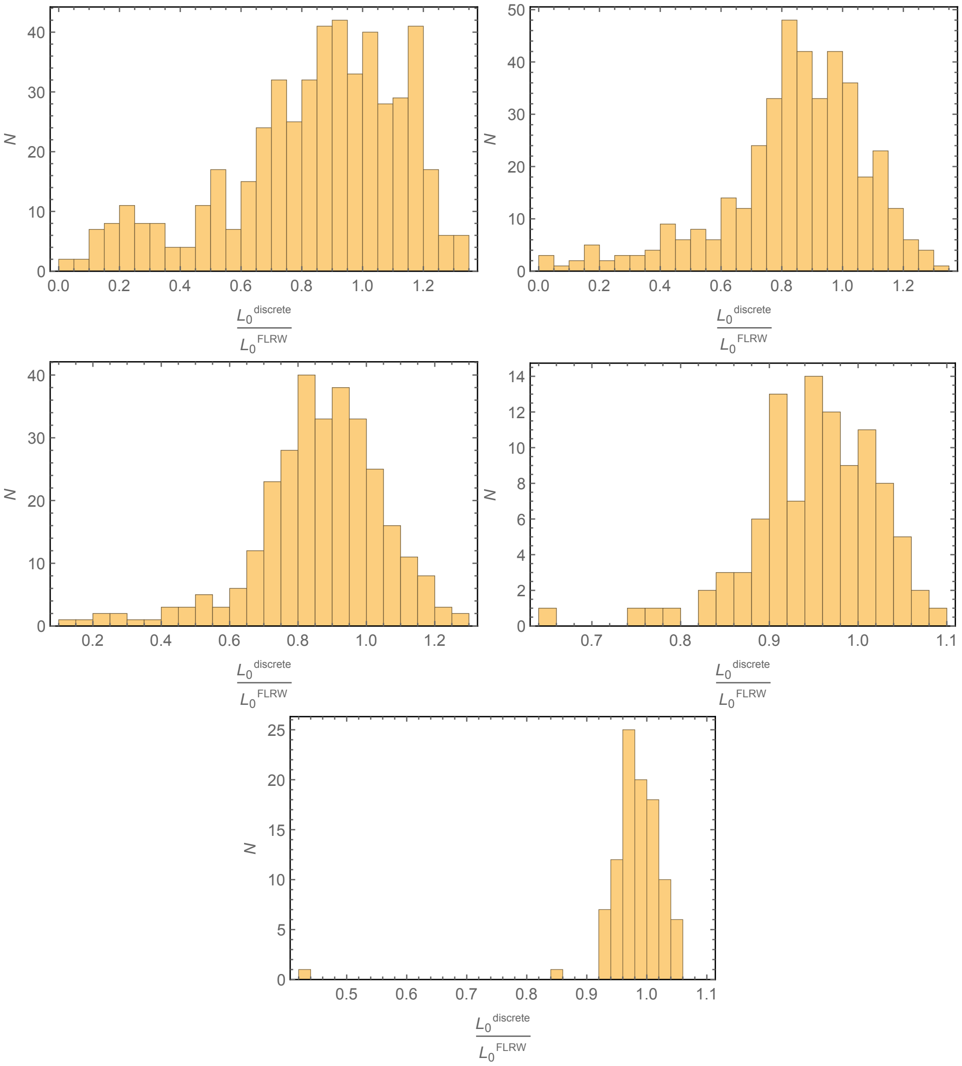

Figure 5.8: Here are the length ratios $L_0^{discrete}/L_0^{FLRW}$ presented as histograms for the four-cell DI model. Top left: length ratios for 500 randomly generated 8-source configurations. Top right: length ratios for 400 randomly generated 16-source configurations. Middle left: length ratios for 300 randomly generated 24-source configurations. Middle right: length ratios for 100 randomly generated 120-source configurations. Bottom: length ratios for 100 randomly generated 600-source configurations.

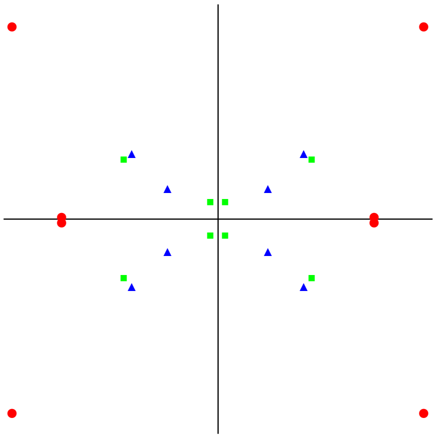

Figure 5.9: Here are three different configurations of 8 sources in a four-cell model stereographically projected. The axes are the surfaces of reflection (also known as the cell boundary). Red: Configuration with length ratio 0.274. Blue: Configuration with length ratio 0.900. Green: Configuration with length ratio 1.15.

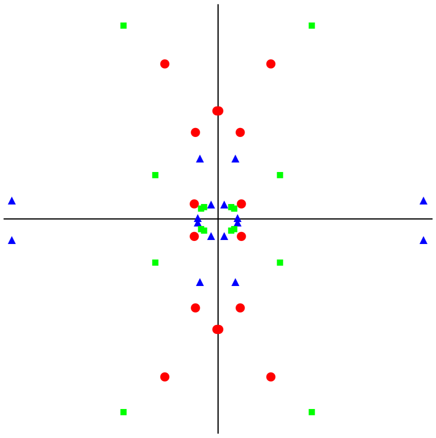

Figure 5.10: Configurations of 16 sources in a four-cell model. The axes are the surfaces of reflection. Red: Configuration with length ratio 0.413. The point on top of the y-axis is actually two points plotted very close to each other on both sides of the cell boundary. Blue: Configuration with length ratio 0.910. Green: Configuration with length ratio 1.28.

Number of Sources	Median $\left(L_0^{discrete}/L_0^{FLRW}\right)$	$\frac{\lvert \text{LQU}-\text{Median}\rvert}{\text{Median}}$	$\frac{\lvert \text{UQU}-\text{Median}\rvert}{\text{Median}}$
8	0.89	0.28	0.24
16	0.87	0.19	0.18
24	0.88	0.16	0.15
120	0.96	0.059	0.057
600	0.98	0.024	0.032

Table 5.4: Median length ratios for the four-cell DI model together with the lower and upper quintile.

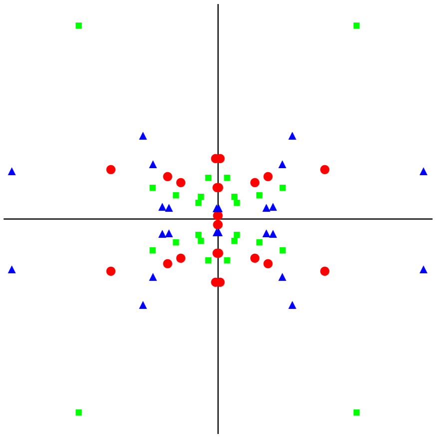

Figure 5.11: Configurations of 16 sources in a four-cell model. The axes are the surfaces of reflection. Red: Configuration with length ratio 0.411. Similarly for the two previous cases, the red points on the x-axis are actually a collection of four points, two on each side, plotted very close to each other. Blue: Configuration with length ratio 0.880. Green: Configuration with length ratio 1.29.

5.2.3 Eight-Cell Great Circle Lengths

Figure 5.12 shows the length ratios for the eight-cell. We see that the general shape is very similar to the four-cell case, except for the 8-source configuration. Because in the eight-cell model, there can only be one source per cell if there is to be 8 sources in total. This causes the model to behave radically different along the LRS curve, as will be clearly shown in section 5.3.

Similarly as for the four-cell case, we can take a look at how some of these configurations look like for certain ratios. These are presented in figures 5.13, 5.14 and 5.15. In these figures, the horizontal, vertical and diagonal axes indicate surfaces of reflection. In these figures we notice that configurations with large length ratios contain points found closest to the LRS curve (which is the point where all surfaces intersect).

Similarly to the four-cell case, configurations with small length ratios (red points) contain a couple of points found very close to the reflection surface. However unlike the four-cell case, the configurations for the eight-cell exhibit more symmetry due to the larger number of cells.

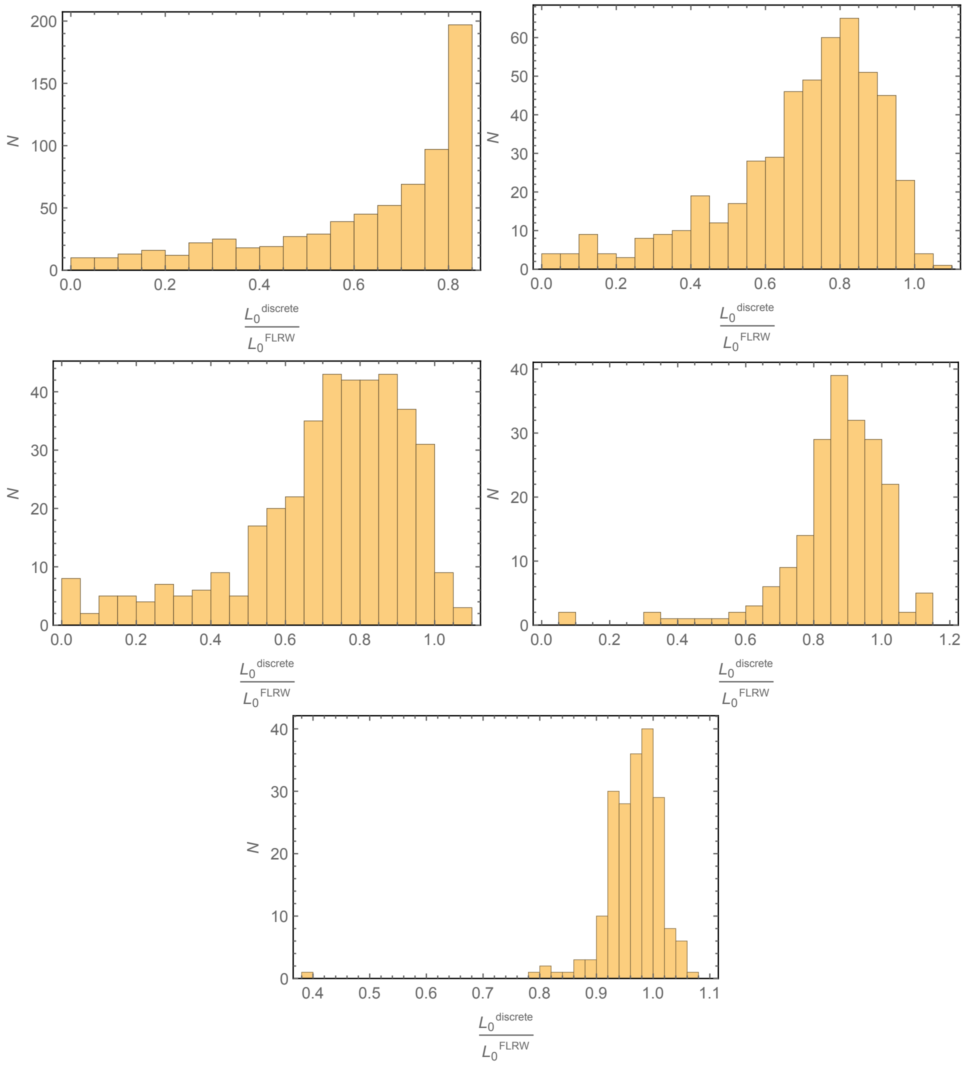

Figure 5.12: Here are the length ratios $L_0^{discrete}/L_0^{FLRW}$ for the eight-cell DI model. Top left: length ratios for 700 randomly generated 8-source configurations. Top right: length ratios for 500 randomly generated 16-source configurations. Middle left: length ratios for 400 randomly generated 24-source configurations. Middle right: length ratios for 200 randomly generated 120-source configurations. Bottom: length ratios for 200 randomly generated 600-source configurations.

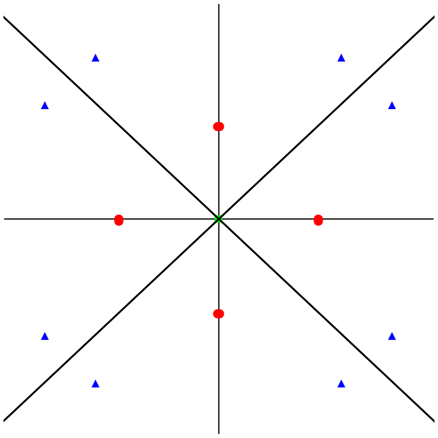

Figure 5.13: Configurations of 8 sources in a eight-cell model. The axes are the planes of reflection. Red: Configuration with length ratio 0.0784. The points are plotted very close to the surfaces, making it look like four points instead of eight. Blue: Configuration with length ratio 0.686. Green: Configuration with length ratio 1.04. These are concentrated around the LRS curve (corresponds to the origin).

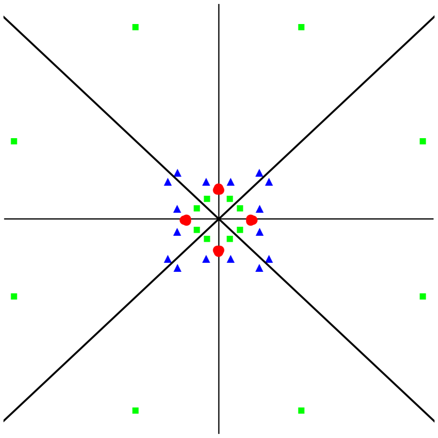

Figure 5.14: Configurations of 16 sources in a eight-cell model. The axes are the planes of reflection. Red: Configuration with length ratio 0.103. Blue: Configuration with length ratio 0.718. Green: Configuration with length ratio 1.01.

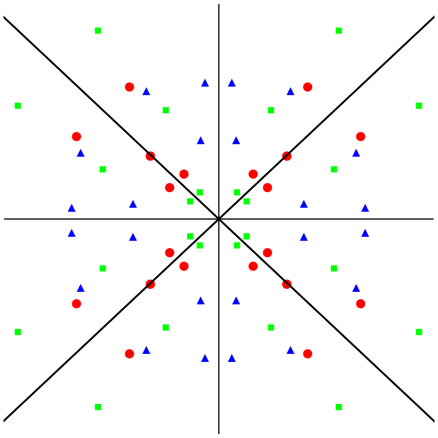

Figure 5.15: Projected configurations of 24 sources in a eight-cell model. The axes are the planes of reflection. Red: Configuration with length ratio 0.00203. Blue: Configuration with length ratio 0.736. Green: Configuration with length ratio 1.02.

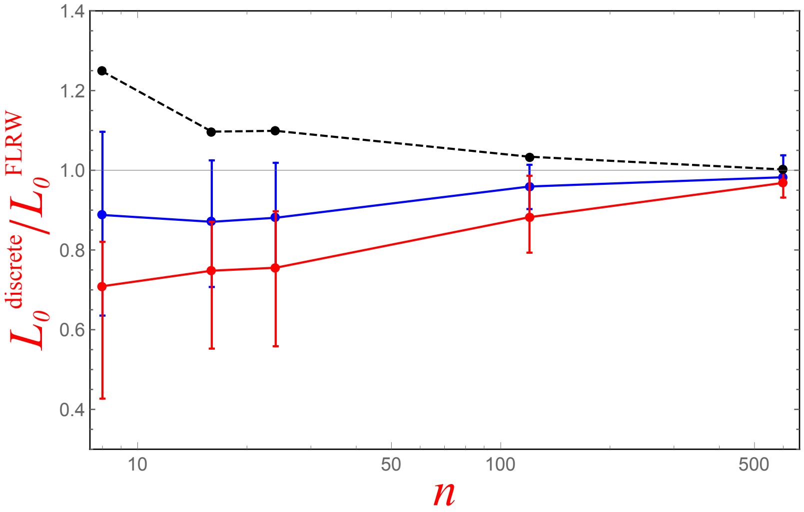

Figure 5.16: Median length ratios as a function of the number of sources n. The black curve shows the result of using regular models as in [6]. The blue and red curves depicts the result for the four-cell and eight-cell DI model respectively. The error bars indicate the location of the LQU and UQU values. The horizontal axis corresponds to the FLRW model. All models approach the FLRW model as the number of sources increases.

Number of Sources	Median $\left(L_0^{discrete}/L_0^{FLRW}\right)$	$\frac{\lvert\text{LQU}-\text{Median}\rvert}{\text{Median}}$	$\frac{\lvert\text{UQU}-\text{Median}\rvert}{\text{Median}}$
8	0.71	0.40	0.16
16	0.75	0.26	0.16
24	0.76	0.26	0.19
120	0.88	0.10	0.12
600	0.97	0.038	0.037

Table 5.5: Median length ratios for the eight-cell DI model together with the lower and upper quintile.

Before leaving these ratios entirely, we can summarize by looking at figure 5.16, which illustrates how the median length ratios of the two DI models varies with number of sources. For comparison, the length ratios for the corresponding regular configurations[4] are included as well. We see that as the number of sources increases, all models approach the FLRW model (horizontal axis at unit ratio). However, the irregular models approaches the FLRW slower than the regular model, as can be seen at $n = 600$, at which the irregular models lies further away from the FLRW limit than the regular one.

However the most striking difference is the way the irregular model approaches the FLRW limit as compared to the regular model. While the regular model ratios are always larger than 1, a majority of the irregular ratios are always smaller than 1 (the median values are always smaller than 1). Figure 5.16 provides solid evidence that the regular and irregular models are different in other ways than just a matter of configuration.

Contrary to what is expected the eight-cell model ratios are mostly smaller than the four-cell model. As is visible from the configuration figures, the eight-cell result in more symmetrical configurations. One would therefore expect that this would result in ratios closer to the isotropic FLRW than the four-cell model. However this is not the case. The cause could be related to the anisotropy of the cell.

5.3 Curvature Along the LRS Curve

Along the LRS curve the curvature is described sufficiently by the quantity E_+ (see subsection 3.3.3). In this section, I will present a few examples of how the curvature behaves along the LRS curve in the eight-cell model in its initially instantaneously static state. These will be referred to henceforth as $(E_+)_0$. Thereafter there will be some statistical investigations on the sign of $(E_+)_0$, as the sign largely predetermines the behavior with time.

An important practical note before proceeding. The initial curvature, as measured by $(E_+)_0$, is evaluated along the LRS curve where $\theta = \phi = 0$. The attentive reader might have realized there is a coordinate singularity along this curve, because the determinant of the metric (3.41) is proportional to $\sin^4\chi \sin^2\theta$, which is zero when $\theta = 0$. This prevents any useful calculations of curvature along the LRS. To avoid this, I rotated the coordinate system before performing any calculations, so the LRS curve now instead lies at $\chi = \theta = 2\pi$ and $\phi \in [0, 2\pi]$. This does not change any physics.

---

[4] I am comparing with the D2 values in [6] table V.

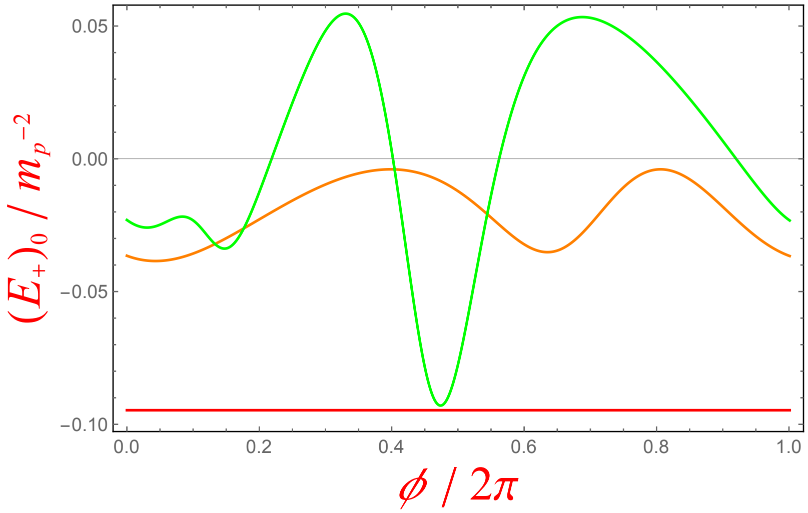

Figure 5.17: Here are the values of $(E_+)_0$ in units of m_p^{-2} (where the proper mass m_p is here the median value for for each respective configuration) along the LRS curve in the eight-cell DI model for 8 sources (bottom, red horizontal line), 16 sources (middle orange curve) and 24 sources (top green curve).

Figures 5.17 and 5.18 provide some examples of how the $(E_+)_0$ varies along the LRS curve (position is given by ϕ). We see that for 8 sources, the curvature is constant! In this regard, it is similar to the FLRW model, where E_+ is negative (since E_+ is actually the negative of $E_{\chi\chi}$, negative E_+ values corresponds to positive curvature) and constant as well along the LRS curve. For the DI model with 8 sources, the constant curvature is likely due to the topology of the 3-sphere.

For 16 and 24 sources, E_+ is dependent on the position on the LRS curve. It not uncommon that some configurations yield functions of E_+ which change sign along the LRS curve, with Riemann flat points between sign transitions (as is the case for 24-source in figure 5.17). Riemann flat points are characterized by a vanishing Riemann tensor $R_{\mu\nu\rho\sigma}$ as is indicated by the vanishing of E_+ at these said points. Furthermore, the number of local maxima (or minima) equal the number of sources in one cell in the 16- and 24-source cases. Examples are provided in figure 5.17. Meanwhile, the 120- and 600-source cases show a great deal of irregularity, with negative troughs and positive peaks.

To understand why some regions on the LRS curve result in positive $(E_+)_0$ values at all, we have to look at figure 13 in [9]. That figure displays positive $(E_+)_0$ values along the curve connecting neighboring sources and the positive maximum corresponds to the location of horizons [9]. Therefore positive values occur whenever the region lies close to the horizon of a source.

We can compare figures 5.17 and 5.18 to the regular counterparts in figures 4 and 5 in [9]. In both the irregular and regular models, there is a decrease in the magnitude of $(E_+)_0 / m_p^{-2}$ (m_p is here the median proper mass of a configuration) as the number of sources increases. The main difference is the lack of symmetry in irregular (E_+) functions and the changing sign.

As will be shown in the next chapter, the sign of $(E_+)_0$ determines the evolution. Figure

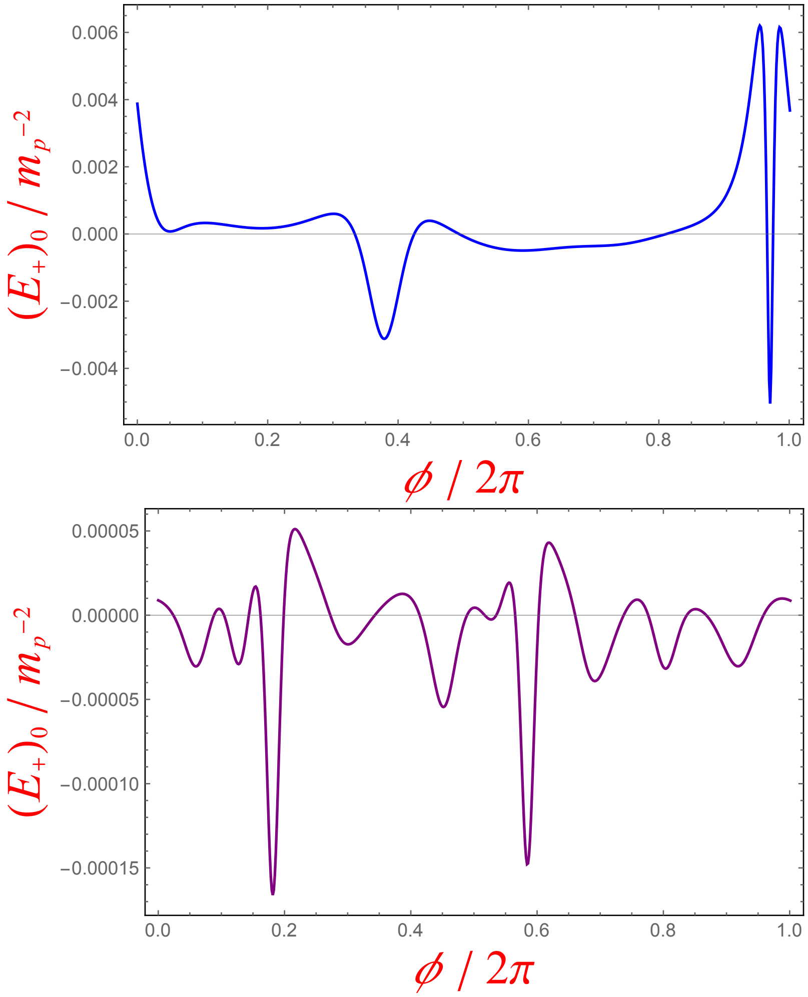

Figure 5.18: $(E_+)_0$ values in units of m_p^{-2} (where the proper mass m_p is here the median value for for each respective configuration) along the LRS curve in the eight-cell DI model for 120 sources (top, blue curve) and 600 sources (bottom, purple curve).

5.19 presents the mean $(E_+)_0$ along the LRS curve. This provides a crude insight into which sign is the dominating one. The median and QU of these distributions are plotted in figure 5.20. From these figures it is clear that the sign is mostly negative, however the magnitude of $(E_+)_0$ approaches zero as the number of sources increases. The fraction of configurations with positive values are plotted against the number of sources in figure 5.21.

Figure 5.21 is interesting as it is not monotonous. This suggests the presence of two different effects, one is more dominant for fewer sources while the other is more dominant for many sources. As mentioned earlier, the positive $(E_+)_0$-values result from the close proximity to horizons. Therefore if there are several horizons close to the LRS curve, one would typically expect more positive $(E_+)_0$-values. Furthermore if the number of sources increased, there is a larger probability that one or several masses will be close proximity to the LRS curve. Thus models containing more sources is expected to result in regions with positive $(E_+)_0$-values more frequently than models with fewer sources. This is indeed the case, visible from figure 5.21, when the sources are increased from 8 to 24. Why there are no positive values at all for 8 sources might be due to the topology of the 3-sphere, just like the constant curvature case.

However as the number of sources are increased, the size of the model (and each cell) increases as well, as is visible in figure 5.16 and by the smaller $|(E_+)|$-values in figure 5.20. As the the size increases, the probability of randomly placing a source close enough (i.e. the distance to the LRS curve and the source's horizon should be comparable) to the LRS curve will decrease. Therefore the number of regions with positive $(E_+)_0$-values should drop with more sources, unless the size of the model is still too small compared to the number of sources present.

With this analysis, we can understand the qualitative behavior of figure 5.21. Initially as we add more sources the accompanying increase in size of the model universe is too small to cause a noticeable difference. The probability that a source is placed close enough to the LRS curve is still large and growing, which results in the increase in figure 5.21. Although when 120 sources is reached, the model is now large enough that the probability of placing a source close enough to the LRS curve will no longer increase, only decrease, as the source count increases.

We can also notice this effect in figures 5.17 and 5.18. In figure 5.17, the model is small enough such that every source produces a noticeable mark in the form of peaks. However in figure 5.18 the model is so large that not every source is distinctly noticeable.

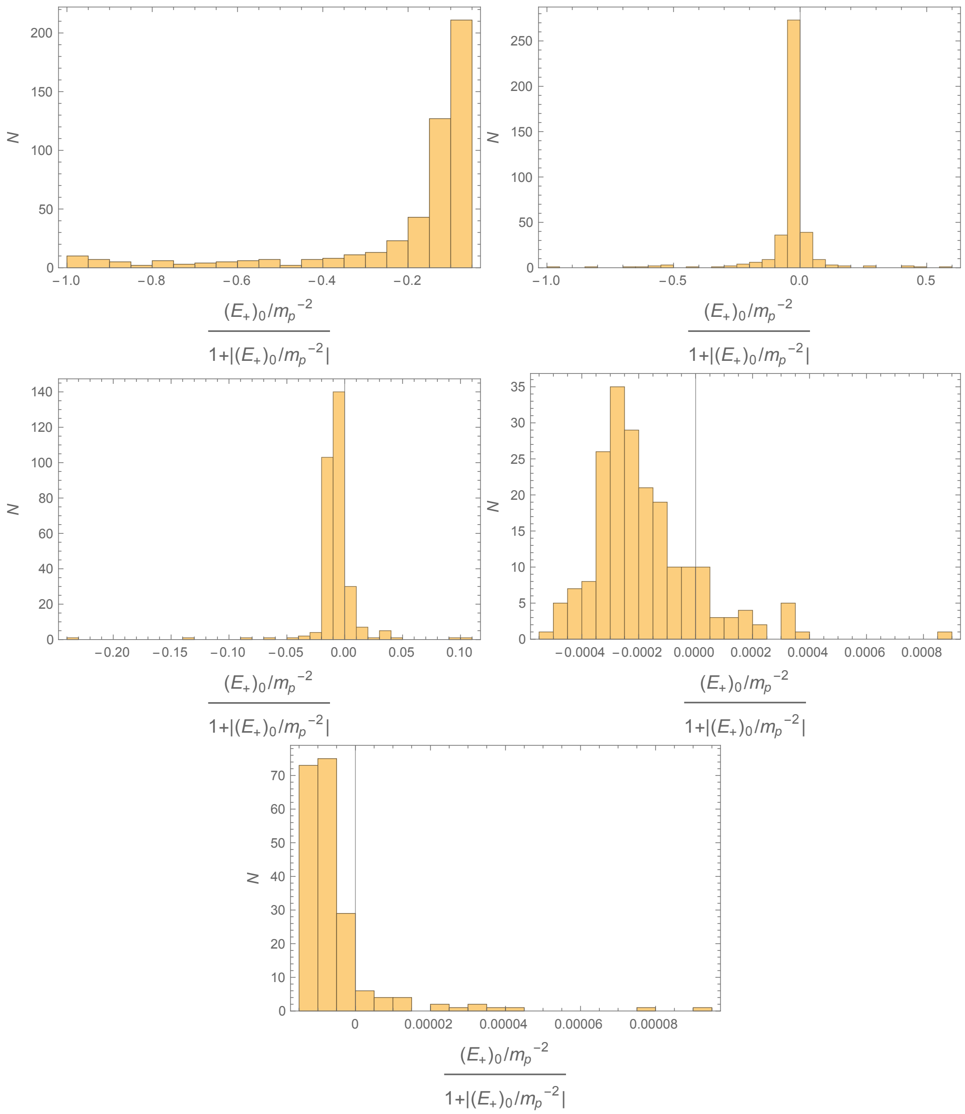

Figure 5.19: The above histograms present the mean $(E_+)_0$ along the LRS curve for different source counts. Top right: 8 sources, 500 configurations. Top left: 16 sources, 400 configurations. Middle right: 24 sources, 300 configurations. Middle right: 120 sources, 200 configurations. Bottom: 600 sources, 200 configurations.

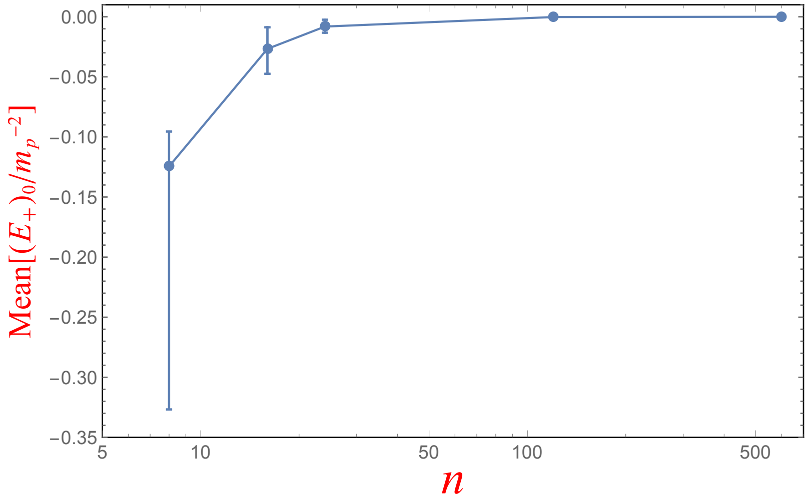

Figure 5.20: Median of distributions in figures 5.19 together with LQU and UQU values. The magnitude of $(E_+)_0/m_p^{-2}$ tends to decrease as the number of sources increases.

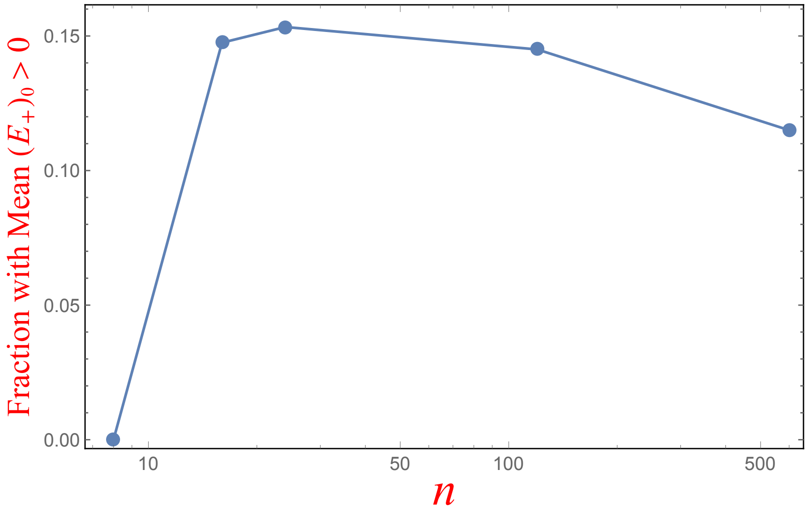

Figure 5.21: The plot depicts the percentage of cases in depicted by figures 5.19 where $(E_+)_0$ is positive. This provides with a crude measure of the sign dominance in $(E_+)_0$ along the LRS curve and how it changes with the number of sources.

Chapter 6

Characteristics of the Time-Evolved State

This chapter introduces a set of very specific equations used to calculate LRS curve length, Hubble parameter and deceleration parameter as a function of time. Afterwards the measurements are presented for each quantity.

6.1 Final Set of Equations

In this section, the final set of equations required in order to the study the dynamics of our model will be presented. We start from where we left off in subsection 3.3.3. Most of this material comes from [9], unless otherwise stated.

The length of our LRS curve in the DI model is given by equation (5.5), or more specifically by equation (5.6). To determine how this length evolves with time requires information about the metric component $g_{\chi\chi}$ at all possible times and at every point along the curve. This length would then by given by (see also section 5.2):

$$l(t) = \int_{\chi_1}^{\chi_2} \sqrt{g_{\chi\chi}}\, \mathrm{d}\chi. \tag{6.1}$$

What remains is to illuminate how $g_{\chi\chi}$ varies with time. We can start by looking at equation (2.27) and remind ourselves that since $\dot{u} = 0$, we have $\theta_{\mu\nu} = \nabla_\mu u_\nu = u_\nu{,}_\mu - \Gamma^\rho_{\nu\mu} u_\rho$. In addition, due to our synchronous coordinate system, u^μ is hypersurface orthogonal and therefore will only have a time component, i.e. $u_\mu = -\partial_\mu t$, where t is the time-coordinate as usual. Therefore, by explicitly evaluating the Christoffel symbol, one obtains for $\theta_{\chi\chi}$

$$\theta_{\chi\chi} = \partial_\chi u_\chi - \Gamma^\rho_{\chi\chi} u_\rho = -\frac{1}{2} g^{tt} (2 g_{t\chi}{,}_\chi - g_{\chi\chi}{,}_t)\, u_t = \frac{1}{2} g_{\chi\chi}{,}_t$$

$$\therefore \theta_{\chi\chi} = \frac{1}{2} \dot{g}_{\chi\chi} \tag{6.2}$$

where an over-head dot now indicates covariant differentiation in the direction of u^μ (see equation (2.20)). Thus equation (6.2) answers the question of how the metric component $g_{\chi\chi}$ changes with time.

However, we still require (6.2) in terms of orthonormal frame components. The relationship between $\theta_{\chi\chi}$ and its corresponding orthonormal frame tensors is given by (see equation (2.35)) $\theta_{\chi\chi} = e^\alpha_\chi e^\beta_\chi \theta_{\alpha\beta}$. Since both $\mathbf{e}_1$ and $\mathbf{e}_\chi$ are always parallel to the LRS curve[1] the spatial part of the line-element along the LRS curve is

$$(dx^1)^2 = g_{\chi\chi} d\chi^2$$

and from this it is clear that $e^1_\chi = \frac{\partial x^1}{\partial \chi} = \sqrt{g_{\chi\chi}}$ which in turn implies:

$$\theta_{\chi\chi} = g_{\chi\chi}\theta_{11}. \tag{6.3}$$

It then follows by combining the two equations (6.2) and (6.3) that

$$\theta_{11} = \frac{1}{2}\frac{\partial}{\partial t}(\ln g_{\chi\chi}). \tag{6.4}$$

This equation is easily solved provided that we introduce the time dependent variable $a_{||}(t)$ implicitly defined by the relation

$$\frac{\dot{a}_{||}}{a_{||}} = \frac{\partial}{\partial t}(\ln a_{||}) := \theta_{11}. \tag{6.5}$$

Equating (6.4) with (6.5) and then integrating on both sides yields the expression $Ca_{||} = \sqrt{g_{\chi\chi}}$ where C is an integration constant. We can set C to $C = \sqrt{(g_{\chi\chi})_0}$ where $(g_{\chi\chi})_0$ is the value of $g_{\chi\chi}$ when $a_{||} = 1$. The length can now be expressed as

$$l(t) = a_{||}(t)\int\limits_{\chi_1}^{\chi_2} \sqrt{(g_{\chi\chi})_0}\,\mathrm{d}\chi, \tag{6.6}$$

$a_{||}(t)$ is therefore the scale factor along the LRS curve.

The quantities $\mathcal{H}_\perp$ and $\mathcal{H}_{||}$ are the rates of expansion and can therefore be expressed as $\mathcal{H}_\perp = \dot{a}_\perp/a_\perp$ and $\mathcal{H}_{||} = \dot{a}_{||}/a_{||}$. Inserting these into equations (3.85), (3.86) and (3.87) provides us with the three expressions

$$\frac{\ddot{a}_{||}}{a_{||}} = \frac{2}{3}E_+ \tag{6.7}$$

$$\frac{\ddot{a}_\perp}{a_\perp} = -\frac{1}{3}E_+ \tag{6.8}$$

$$\dot{E}_+ + 3\frac{\dot{a}_\perp}{a_\perp}E_+ = 0 \tag{6.9}$$

where $a_\perp(t)$ is implicitly defined by

---

[1] $\mathbf{e}_1$ is parallel to the LRS curve by definition. $\mathbf{e}_\chi$ is parallel to the LRS curve due to the DI model's construction.

$$\frac{\dot{a}_\perp}{a_\perp} = \frac{\partial}{\partial t}(\ln a_\perp) := \theta_{22}. \tag{6.10}$$

We can now proceed by looking at equation (6.9). Collecting E_+ and $a_\perp$ together with their respective derivatives on opposite sides of the equality sign and thereafter integrating on both sides with respect to time provides the expression of how E_+ depends on $a_\perp$:

$$E_+ = \frac{(E_+)_0}{a_\perp^3} \tag{6.11}$$

Here $(E_+)_0$ is an integration constant and defined as the value of E_+ when $a_\perp = 1$.

We still need an explicit expression of how the scale factor depends on time. These are obtained from the remaining two differential equations (6.7) and (6.8). The expression for $a_\perp$ is obtained from equation (6.8) through multiplying both sides by $\dot{a}_\perp$ and then integrating once, results in the expression

$$\frac{\dot{a}_\perp^2}{a_\perp^2} = \frac{2}{3}\frac{(E_+)_0}{a_\perp^3} - \frac{k}{a_\perp^2} \tag{6.12}$$

where k is an integration constant.

For a moment we can turn our attention to equations (6.8) and (6.9). These equations are invariant under rescaling of $a_\perp$, i.e. performing the substitutions $a_\perp \mapsto \lambda a_\perp$, $\dot{a}_\perp \mapsto \lambda \dot{a}_\perp$ and $\ddot{a}_\perp \mapsto \lambda \ddot{a}_\perp$ in equations (6.8) and (6.9) leaves them unchanged, where λ is an arbitrary constant. However, performing the same rescaling in equation (6.12) provides us with an interesting possibility. If we set $a_\perp = 1$, the option arises in which we can always arrange λ such that $\dot{a}_\perp = 0$ on the initial hypersurface (since λ is an arbitrary constant). I will assume that we do so from now on: $\dot{a}_\perp = 0$ when $a_\perp = 1$. This further implies that quantities with subscript 0 are also valid when $\dot{a}_\perp = 0$ and correspond to their respective values on the initial hypersurface (on the initial hypersurface $\Theta = \sigma_+ = 0$ and so $\theta_{22} = 0$). Thus $(E_+)_0$ is E_+ evaluated on the initial time-symmetric hypersurface. We see also from equation (6.12) that under these circumstances $k = 2(E_+)_0/3$. This will also be assumed from now on due to the scale invariance of $a_\perp$.

The differential equation that needs to be solved is

$$\dot{a}_\perp^2 = \frac{2}{3}(E_+)_0(\frac{1}{a_\perp} - 1). \tag{6.13}$$

The solutions can be divided into three cases; depending on the sign of $(E_+)_0$, and are presented below.

6.1.1 Evolution when $(E_+)_0 = 0$

Setting $(E_+)_0 = 0$ in equations (6.7) and (6.13) implies that $\ddot{a}_{||} = 0$ and $\dot{a}_\perp = 0$ respectively. Since $\Theta = \sigma_+ = 0$ on the initial hypersurface, from (6.5), $\dot{a}_{||} = 0$ as well. This all amounts to

$$a_{||} = 1 \tag{6.14}$$

$$a_\perp = 1 \tag{6.15}$$

and therefore any points which are initially Riemann flat (corresponding to $(E_+)_0 = 0$), will remain Riemann flat throughout time.

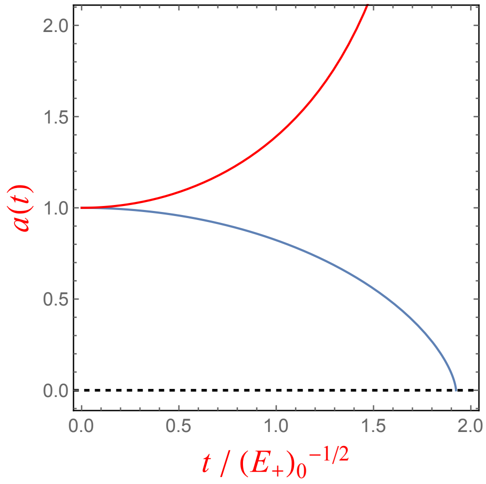

Figure 6.1: Above are the scale factors $a_\perp(t)$ (blue curve) and $a_{||}(t)$ (red curve) for $(E_+)_0 > 0$. The dashed black line shows where the scale factor is zero. $a_{||}(t)$ continues to infinity.

6.1.2 Evolution when $(E_+)_0 > 0$

When $(E_+)_0 > 0$, the solution to (6.13) can be expressed in parametric form as

$$a_\perp = \cos^2\eta \tag{6.16}$$

$$t - t_0 = \frac{1}{\sqrt{\frac{2}{3}(E_+)_0}}\left(\eta + \frac{1}{2}\sin(2\eta)\right) \tag{6.17}$$

where $-\frac{\pi}{2} < \eta < \frac{\pi}{2}$ and t_0 is the resulting integration constant. It is defined so that $t - t_0 = 0$ on the initial hypersurface. η is known as *conformal time* or *arc-parameter time*. It is defined as the arc, in radians, a photon covers in time dt traveling on a hypersurface of radius $a(t)$ [4, 2]

$$d\eta = \frac{dt}{a(t)} \tag{6.18}$$

Inserting this result into equation (6.7) provides us with the scale factor along the LRS curve. By exploiting scale invariance, similarly to the $a_\perp$ case, to set $\dot{a}_{||} = 0$ when $a_{||} = 1$ results in

$$a_{||} = \frac{1}{2}(3 - \cos^2\eta + 3\eta\tan\eta) \tag{6.19}$$

6.1.3 Evolution when $(E_+)_0 < 0$

When $(E_+)_0 < 0$ the solutions are obtained analogously as the previous case. The solution for both scale factors along the LRS curve in this case are given by

$$a_\perp = \cosh^2\eta \tag{6.20}$$

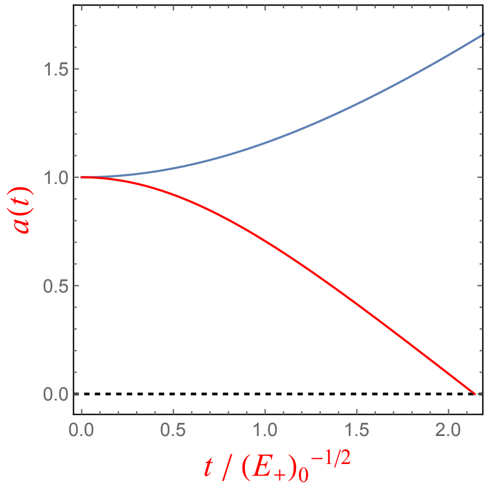

Figure 6.2: Above are the scale factors $a_\perp(t)$ (blue curve) and $a_{||}(t)$ (red curve) for $(E_+)_0 < 0$. The dashed black line shows where the scale factor is zero.

$$a_{||} = \frac{1}{2}(3 - \cosh^2\eta - 3\eta\tanh\eta) \tag{6.21}$$

where

$$t - t_0 = \frac{1}{\sqrt{-\frac{2}{3}(E_+)_0}}\left(\eta + \frac{1}{2}\sinh(2\eta)\right). \tag{6.22}$$

Once again t_0 is a constant of integration defined so that $t - t_0 = 0$ on the initial hypersurface.

6.2 Curvature Evolution

By using the equations provided in the previous section, we can observe how E_+ in figure 5.17 evolves as time progresses. Here and the following sections, increasing times means that we are moving away from our initial hypersurface which lies at $t = t_0 = 0$. The result is presented as spacetime diagrams in figure 6.3. In these diagrams, white regions are singularities and are separated from the rest of the colored diagram by solid or dashed black lines. These indicate the two types of singularities present, *viz.* curvature singularities and coordinate singularities respectively, appearing on the LRS curve. As mentioned in subsection 2.1.1, when the certain conditions are fulfilled we can expect coordinate singularities to arise sometime. Time is scaled by the configuration's *median* proper mass.

The dashed black lines surround boundaries which are due to coordinate singularities. This can be understood by looking at equation (6.8). For $E_+ < 0$ (notice that the coordinate singularities, as indicated by the dotted black line in figure 6.3, only occur in regions where $E_+ < 0$), it follows that $\ddot{a}_\perp > 0$, and therefore $a_\perp$ always increases as time progresses ($a_\perp$ is initially 1 and always positive). As $a_\perp$ always increases, $\dot{a}_\perp > 0$ which, by equation (6.9), implies that $\dot{E}_+/E_+ < 0$. Therefore if $E_+ < 0$, as time progresses, E_+ will approach zero and remain

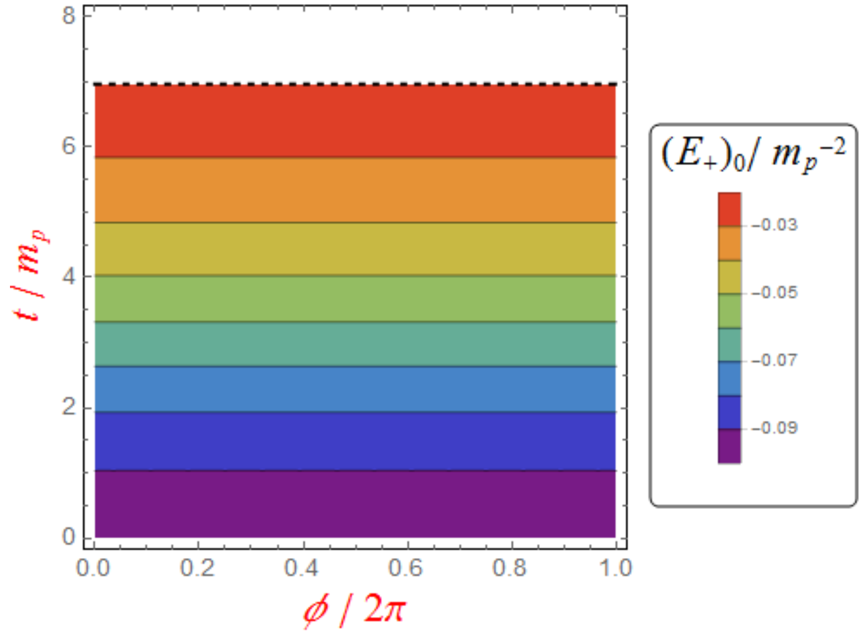

Figure 6.3: Spacetime diagrams of the value of E_+ along the LRS curve for the eight-cell model containing 8 sources. Contours are added for clarity. The accompanying color scales indicate the value of E_+. The dashed black line indicate coordinate singularities. Time t and E_+ are scaled by the configuration's proper mass m_p.

finite. Thus areas bounded by the dashed black line do not correspond to physical singularities, but due to coordinate singularities [9].

The opposite is true for areas bounded by the solid black line. These occur in regions where $E_+ > 0$ and, from equation (6.8), this implies that $\ddot{a}_\perp < 0$. As $a_\perp$ is initially $(a_\perp)_0 = 1$ and should be positive, a negative second derivative means that $a_\perp$ will decrease, i.e. $\dot{a}_\perp < 0$, until the value zero. By equation (6.9), we see that this implies $\dot{E}_+/E_+ > 0$. Therefore E_+ will increase infinitely in these regions and correspond therefore to curvature singularities [9].

In figures 6.3-6.5, we see how the sign of E_+ on the initial hypersurface determines the time evolution. Negative regions will approach flat space until a coordinate singularity occurs while positive regions will evolve into curvature singularities. Regions with larger E_+ magnitude tend to reach singularities first. For 8 sources, curvature is constant along the LRS and remains constant throughout time. The 120 and 600 source cases are omitted as these diagrams are difficult to plot neatly. The principles are the same as for the lower source counts however.

Beyond physical curvature singularities there is nothing and provides a definite limit of how long our model can be observed along the entire LRS curve. Beyond coordinate singularities however, spacetime still exists and continues to evolve. These regions are though inaccessible without altering/changing the coordinate system. Consequentially the coordinate singularities will also impair any further measurement along the LRS curve.

Therefore the first appearance of any singularity along the LRS will set a limit for how long

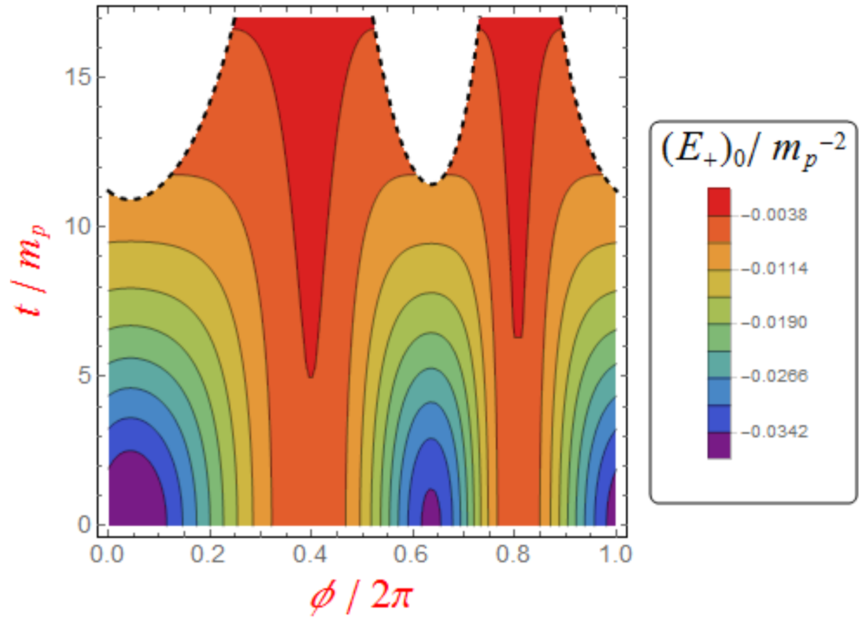

Figure 6.4: Spacetime diagrams of the value of E_+ along the LRS curve for the eight-cell model containing 16 sources. The accompanying color scales indicate the value of E_+. The dashed black line indicate coordinate singularities. Contours are shown for clarity. Time t and E_+ are scaled by the configuration's median proper mass m_p

we can perform measurements along the LRS curve. Since this will depend on the particular configuration of the model, a distributions of times are expected even when the number of sources are the same. Figures 6.6 and 6.7 shows a collection of histograms of the time it takes for the two types of singularities to arise somewhere along the LRS curve scaled by the *median* proper mass of the system. Tables 6.1 and 6.2 complement figures.

Figure 6.8 plots the median time scaled by total proper mass against the number of sources. The error bars indicate as usual the lower and upper quintile. There we see that time increases with the number of sources. The possible interpretation is that the universe our model depicts, grows with larger sources. This is also consistent with figure 5.16. Furthermore we see how the FLRW and DI models deviate from each other as the source count increases.

Notice also that coordinate singularities occur in general before curvature singularities. Thus if we had changed coordinate system, observations could have been performed for a little longer in some cases.

6.3 Length Evolution of LRS Curve

By using equation (6.6), we can observe how the length of the LRS curve changes with time. Although singularities will arise at some point, at which the curvature along the entire LRS is no longer entirely known. Therefore length measurements cease as soon as these singularities arises. The results are depicted in figures 6.9-6.13. The lengths are scaled by the length of the

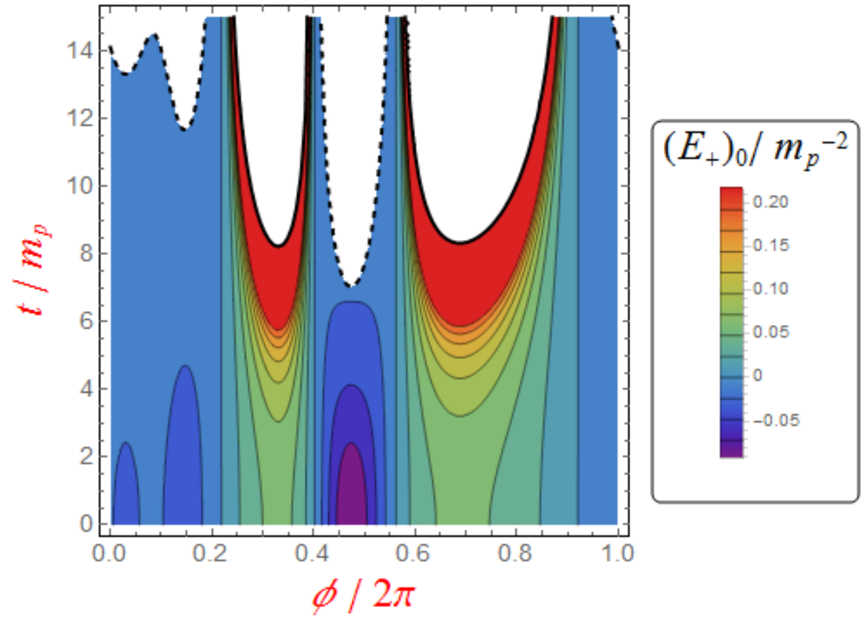

Figure 6.5: Spacetime diagrams of the value of E_+ along the LRS curve for the eight-cell model containing 24 sources. The accompanying color scales indicate the value of E_+. Red regions indicate values at or above the scale. The thick black lines (solid and dashed) indicate singularities (coordinate and curvature singularities respectively). Contours are shown for clarity. Time t and E_+ are scaled by the configuration's proper mass m_p

Number of Sources	Median $\left(t/m_p\right)$	$\frac{\lvert\text{LQU}-\text{Median}\rvert}{\text{Median}}$	$\frac{\lvert\text{UQU}-\text{Median}\rvert}{\text{Median}}$
8	6.1	0.32	0.14
16	8.7	0.33	0.23
24	12.4	0.19	0.18
120	39.1	0.29	0.34
600	98.4	0.43	0.48

Table 6.1: Table displaying the median time it takes for the first coordinate singularity to appear. See distributions 6.6

Number of Sources	Median $\left(t/m_p\right)$	$\frac{\lvert\text{LQU}-\text{Median}\rvert}{\text{Median}}$	$\frac{\lvert\text{UQU}-\text{Median}\rvert}{\text{Median}}$
16	11.7	0.48	0.74
24	15.9	0.33	0.64
120	64.0	0.32	0.47
600	181.4	0.46	0.50

Table 6.2: Table displaying the median time it takes for the first curvature singularity to appear. See distributions 6.7

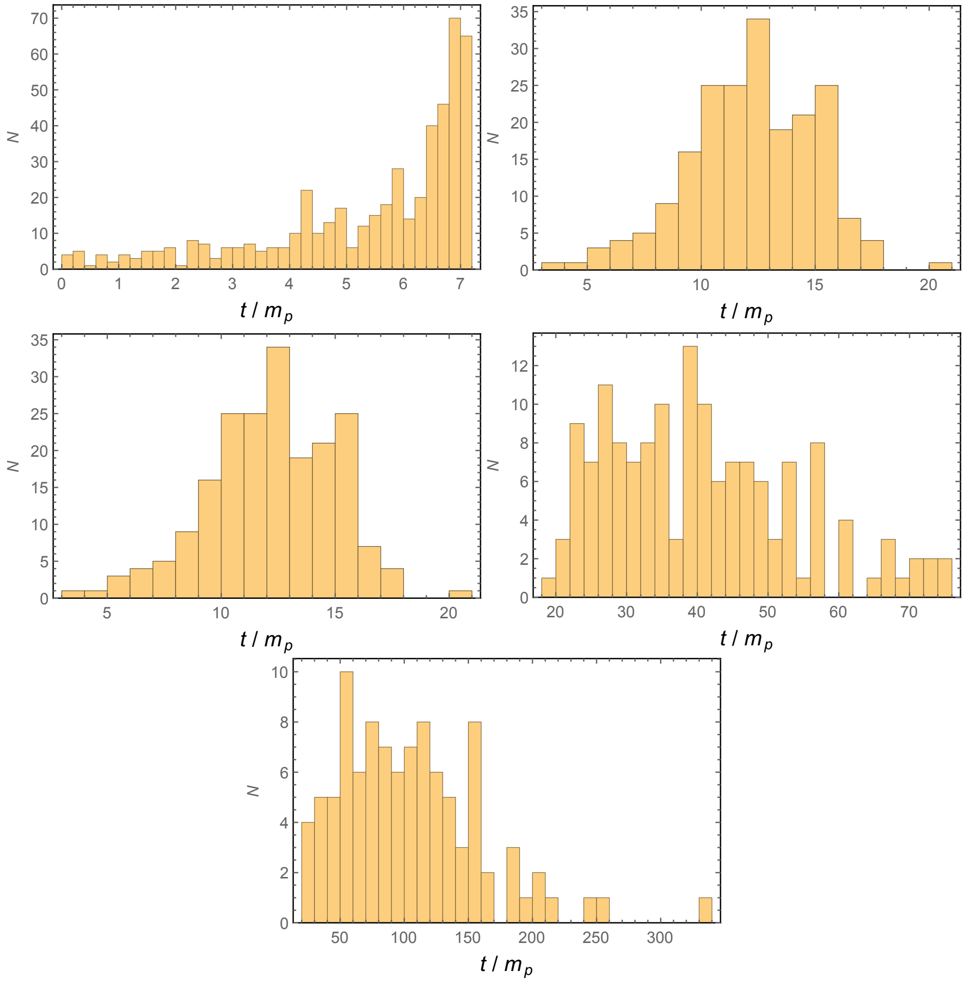

Figure 6.6: Statistics of when the first coordinate singularity arises somewhere along the LRS curve. The time is scaled by each configuration's respective median proper mass. Top left: 8 sources, 500 observed configurations. Top right: 16 sources, 250 observed configurations. Middle left: 24 sources, 200 observed configurations. Middle right: 120 sources, 150 observed configurations. Bottom: 600 sources, 100 observed configurations.

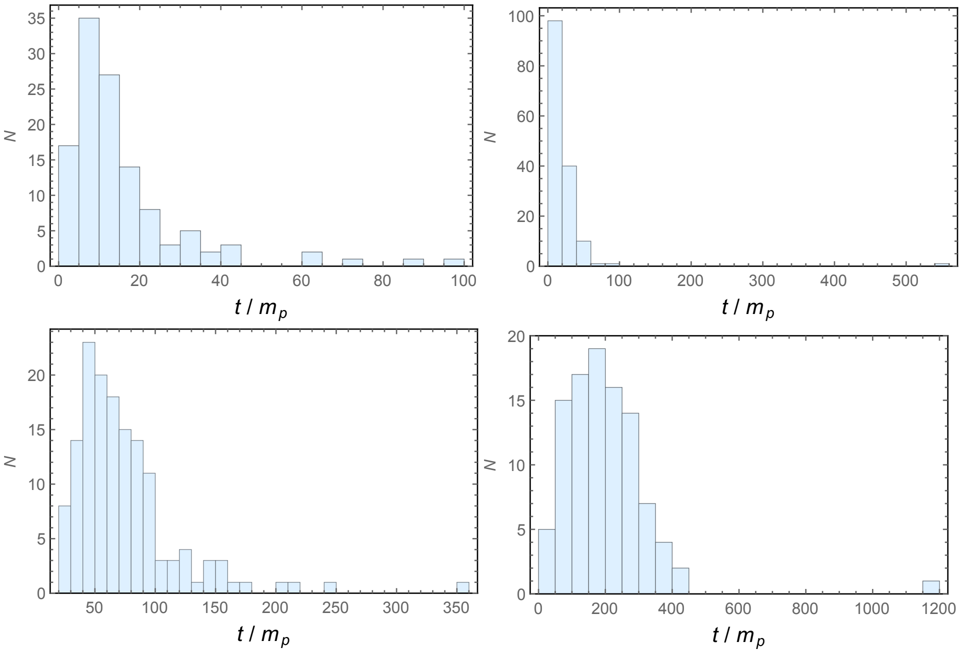

Figure 6.7: Statistics of when the first curvature singularity arises somewhere along the LRS curve. The time is scaled by each configuration's respective median proper mass. Remember that not all configurations will yield a curvature singularity (at least a real singularity which does not lie beyond a coordinate singularity) since it requires $(E_+)_0 > 0$. Top left: 16 sources, 119 configurations. Top right: 24 sources, 151 configurations. Bottom left: 120 sources, 146 configurations. Bottom right: 600 sources, 100 configurations.

same curve in the FLRW on the *initial hypersurface* with the same total proper mass. Time is scaled by the total proper mass M_p.

Figure 6.9 depicts the 8 source case. As mentioned earlier, this case is unique since the curvature is constant along the LRS curve due to the presence of only one source per cell. In the figure we can see a clear correlation between the initial length and time taken until a singularity appears; longer initial lengths (or larger universes) result in longer times. Another interesting feature is that none of the curves present intersect. Overall, all curves follow the same qualitative behavior, namely the length of the LRS curves decrease with time, although the lengths differ remarkably from the FLRW and regular (dark blue) case.

The 16 source case is dramatically different from the 8 source case as can be seen from figure 6.10, since the curvature is no longer constant along the LRS curve in the 16 source model. From the figure, we can divide the behavior of the curves into two broad categories. The first category are the curves which behave qualitatively similarly to the FLRW curve and the regular case, i.e. the LRS length decreases with time. The other category contains curves which increase at some point in time. This is very interesting as it means that for some configurations, the universe expands around the LRS. One can also see a few cases where the curves initially follow the FLRW case closely.

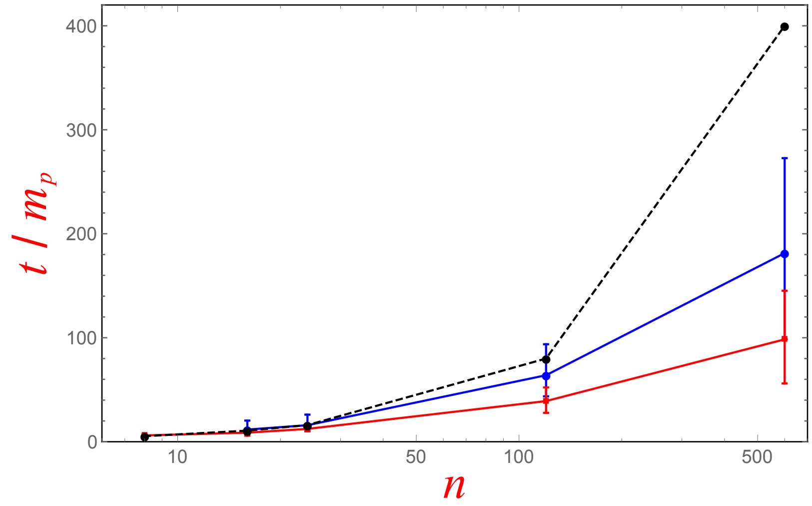

Figure 6.8: Median time, scaled by the median proper mass m_p, until the first singular point arises along the LRS curve as a function of sources. Blue curve is the median time for the appearance of the first curvature singularity. Red curve is for coordinate singularities. The dashed line is the time it takes for singularities to arise in the spherical FLRW model.

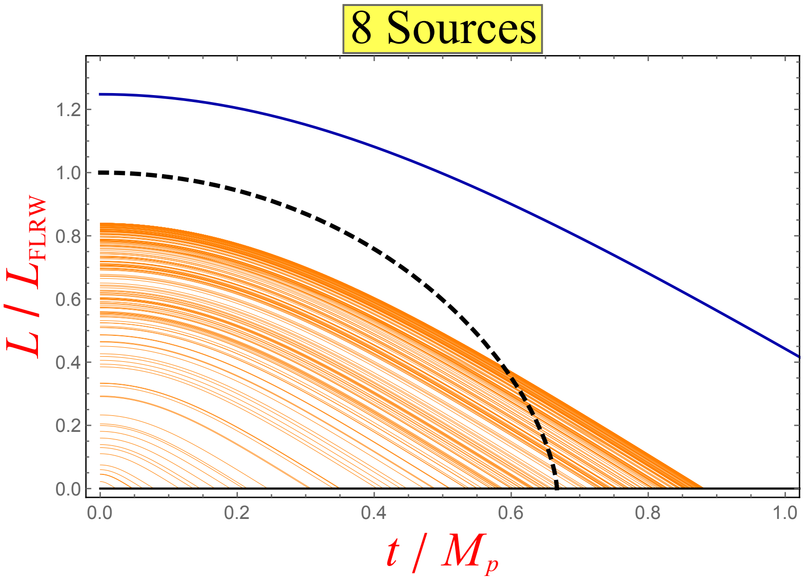

Figure 6.9: LRS length evolution for 200 randomly generated configurations containing 8 sources. Plot above depicts how the length of the LRS curve changes with time (the initial hypersurface lies at $t = 0$) and each orange line depicts the length of an LRS curve in one configuration with 8 sources. The dark blue line depicts the regular 8 source case (see [9] for details). The dashed black line depicts the FLRW case.

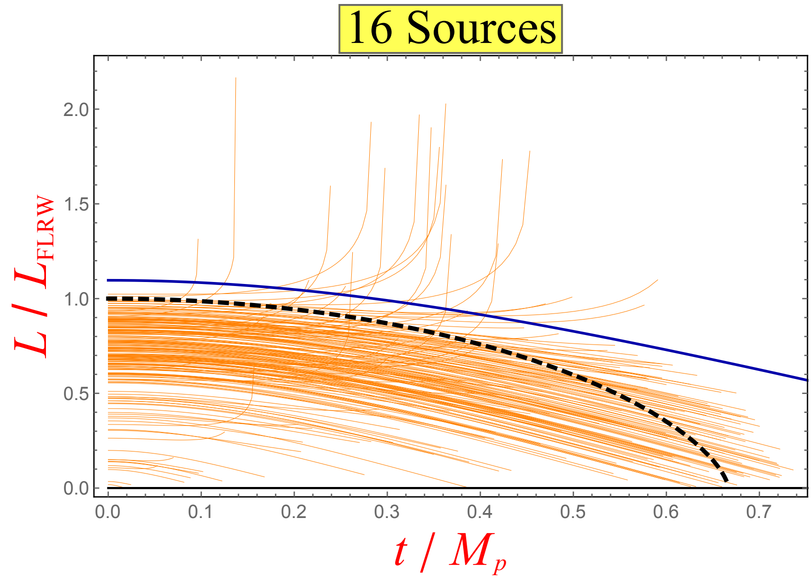

Figure 6.10: LRS length evolution for 200 randomly generated configurations containing 16 sources. Plot above depicts how the length of the LRS curve changes with time (the initial hypersurface lies at $t = 0$) and each orange line depicts the length of an LRS curve in one configuration with 16 sources. The dark blue line depicts the regular 16 source case (see [9] for details). The dashed black line depicts the FLRW case.

In the 24 source model, figure 6.11, there are once again two qualitatively different behaviors exhibited by the curves: either the curves are constantly decreasing or increases at some later point in time. In addition there are a few curves which initially follow the regular 120 model. Similar conclusions can also be drawn from figures 6.12 and 6.13. An overall pattern is that the initial starting values become more concentrated around the FLRW case, which is consistent with figure 5.16.

6.4 Hubble Rates and Deceleration Parameters

Analogously to FLRW cosmology, we can define the quantities Hubble rate and deceleration parameter, respectively as

$$\mathcal{H}_L := \frac{L}{\dot{L}} \tag{6.23}$$

$$q_L := -\frac{\ddot{L}L}{\dot{L}^2} \tag{6.24}$$

where L are the lengths provided in figures 6.9-6.13. The spatially closed FLRW solution are also presented for reference [9]. We will take a brief look at them one at a time. The Hubble

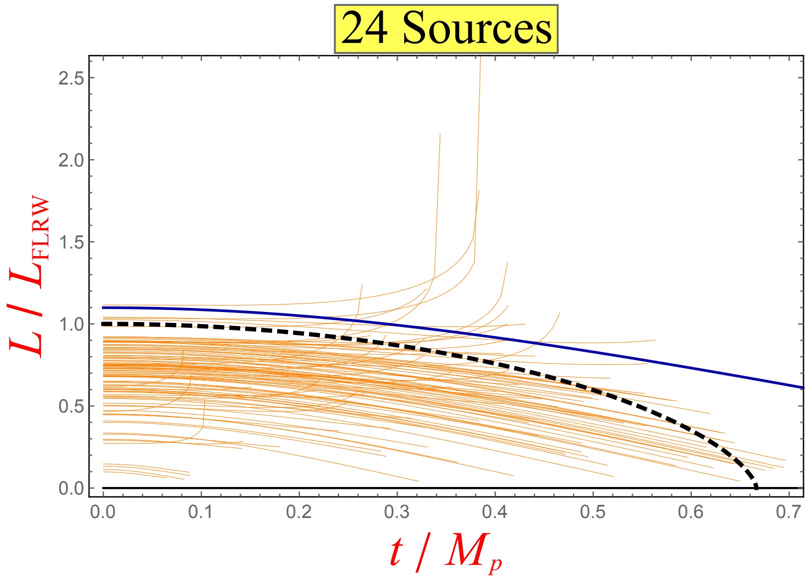

Figure 6.11: LRS length evolution for 100 randomly generated configurations containing 24 sources. Each orange line depicts the length of an LRS curve in one configuration with 24 sources. The dark blue line depicts the regular 24 source case (see [9] for details). The dashed black line depicts the FLRW case.

rate and time are scaled by the total proper mass M_p. The deceleration parameter is already dimensionless.

The result for 8 sources is perhaps not very exciting. Since the curvature is constant along the LRS, it should behave in a similar manner to the FLRW model. As is seen from figure 6.14, both models behave qualitatively the same: all Hubble rate starts at zero before decreasing toward infinite negative values and all deceleration parameters starts at positive infinity before settling down at zero. For the Hubble rate, initially at least, there are a few curves which even behave quantitatively similarly to the FLRW model. This is not the case for the deceleration parameter, as is visible from the inlay.

The situation is much more interesting with 16 sources, since now the curvature is no longer constant along the LRS curve and we can therefore expect radically different behavior from the FLRW. As seen from figure 6.15, this is most certainly the case. For the Hubble rate, some curves initially behave quantitatively the same as the FLRW model. Thereafter their behavior can radically deviate. Some curves yield increasing Hubble rates. These curves have a positive second derivative (second derivative of the Hubble rate w.r.t. time). The other curves will still yield decreasing Hubble rate as time progresses. These have negative second derivatives and are qualitatively similar to the FLRW model. All curves end up in either category. Some curves yield always positive Hubble parameters, meaning that the LRS curve is expanding.

In figure 6.15 the curves describing the deceleration parameter can be broadly divided into two categories as well. The curves which starts at negative infinity and the curves which start at positive infinity. The second category is more qualitatively similar to the FLRW model.

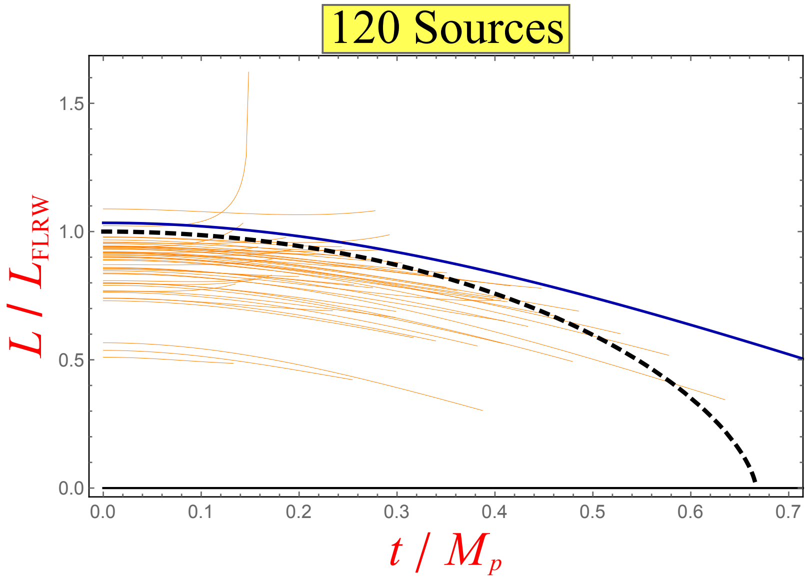

Figure 6.12: LRS length evolution for 50 randomly generated configurations containing 120 sources. Each orange line depicts the length of an LRS curve in one configuration with 120 sources. The dark blue line depicts the regular 120 source case (see [9] for details). The dashed black line depicts the FLRW case.

The presence of negative deceleration values means that for some configurations the LRS curve length is accelerating!

Similar analysis can be made for the remaining figures 6.16, 6.17 and 6.18. Looking at them all together one can notice the overall pattern that as the number of sources increases, a larger portion of curves describing the Hubble rate have a positive second derivative. This is also the case for the regular models. Looking at figure 11 in [9], the 600-cell curve has a small but noticeable positive second derivative. Therefore this pattern seems to be linked to the number of sources.

What is most striking of these plots however, is the presence of negative deceleration parameters. In standard FLRW cosmology, this would require the presence of exotic matter such as dark energy [4]. Using equation (5.10) to remove the curvature k term from the Friedmann equation (5.11) results in the expression

$$-\frac{\ddot{a}}{a} = \frac{4\pi}{3}(\rho + 3p).$$

This expression can be further modified if we use the *equation of state* $p = \omega\rho$, where ω is some real valued constant,

$$-\frac{\ddot{a}}{a} = \frac{4\pi}{3}(1 + 3\omega)\rho. \tag{6.25}$$

Here the acceleration of the scale factor is expressed in terms of the energy density content of the universe.

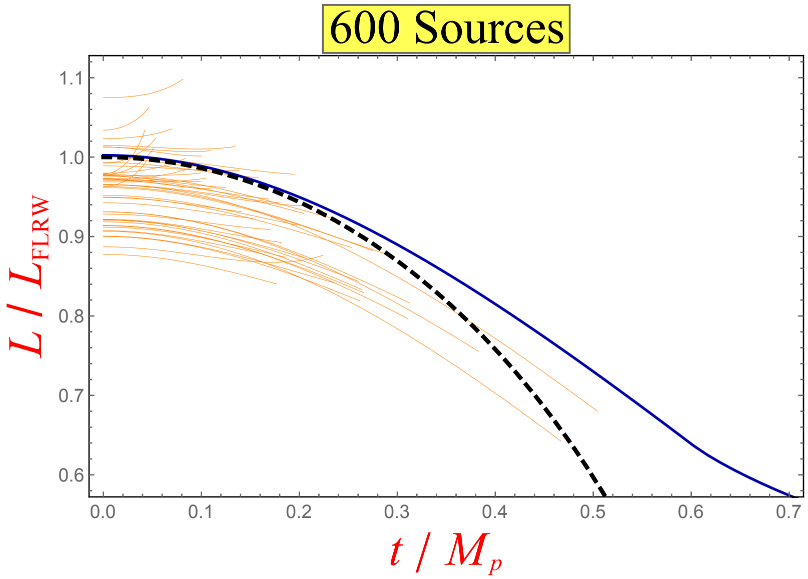

Figure 6.13: LRS length evolution for 50 randomly generated configurations containing 600 sources. Each orange line depicts the length of an LRS curve in one configuration with 600 sources. The dark blue line depicts the regular 600 source case (see [9] for details). The dashed black line depicts the FLRW case.

Since a and ρ are always positive, the sign of $\ddot{a}$ is then determined by the factor $(1+3\omega)$. Together with the definition of the deceleration parameter q_L (6.24), we can conclude that q_L must have the same sign as the factor $(1+3\omega)$. This places constraints on ω for different signs of q_L:

1. $q_L \geq 0 \iff \omega \geq -\frac{1}{3}$
2. $q_L < 0 \iff \omega < -\frac{1}{3}$

The first case is satisfied by ordinary matter and radiation since these have $\omega \sim 0$ and $\omega \sim \frac{1}{3}$ respectively. The second case requires something such as dark energy with $\omega \sim -1$.

However in the DI models, a negative and positive deceleration parameter is found in models containing ordinary matter. What distinguishes one case from the other is merely how the matter is distributed.

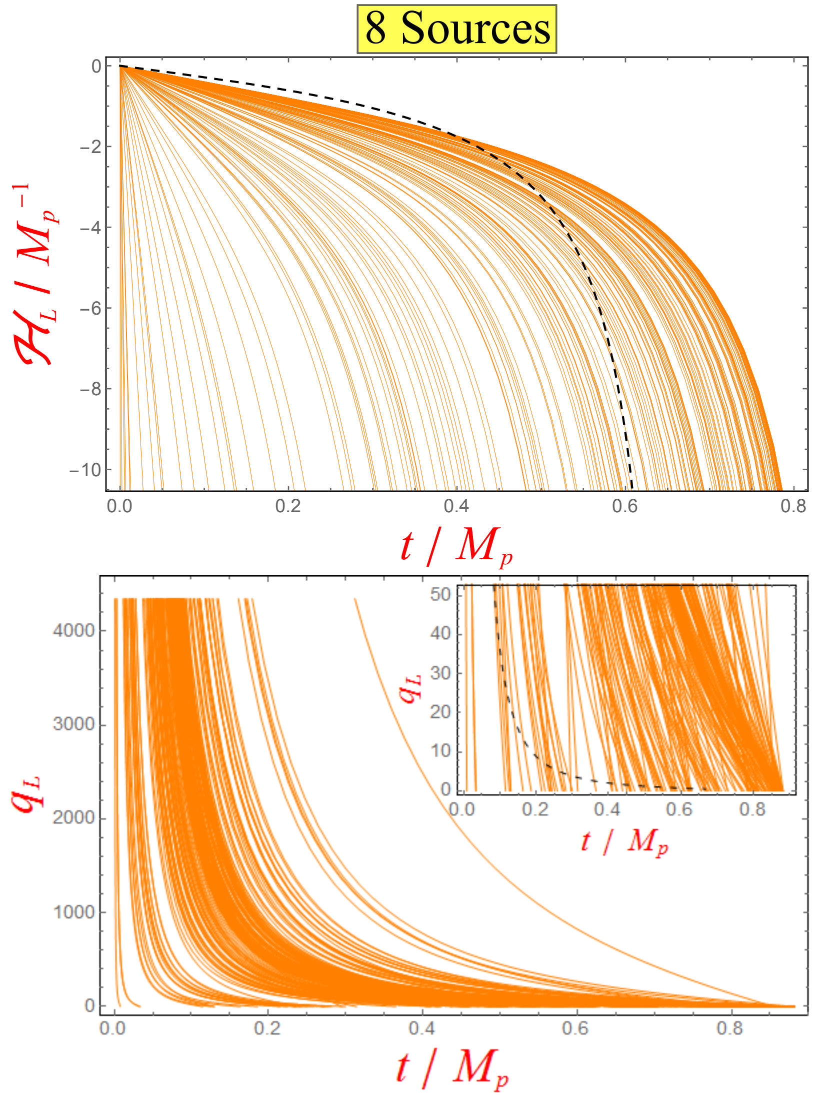

Figure 6.14: Above graphics depict the Hubble parameter (top) and the associated deceleration parameter (bottom) for 8 sources (200 different configurations measured). The black dashed line depicts the FLRW model (shown as an inlay for the deceleration parameter).

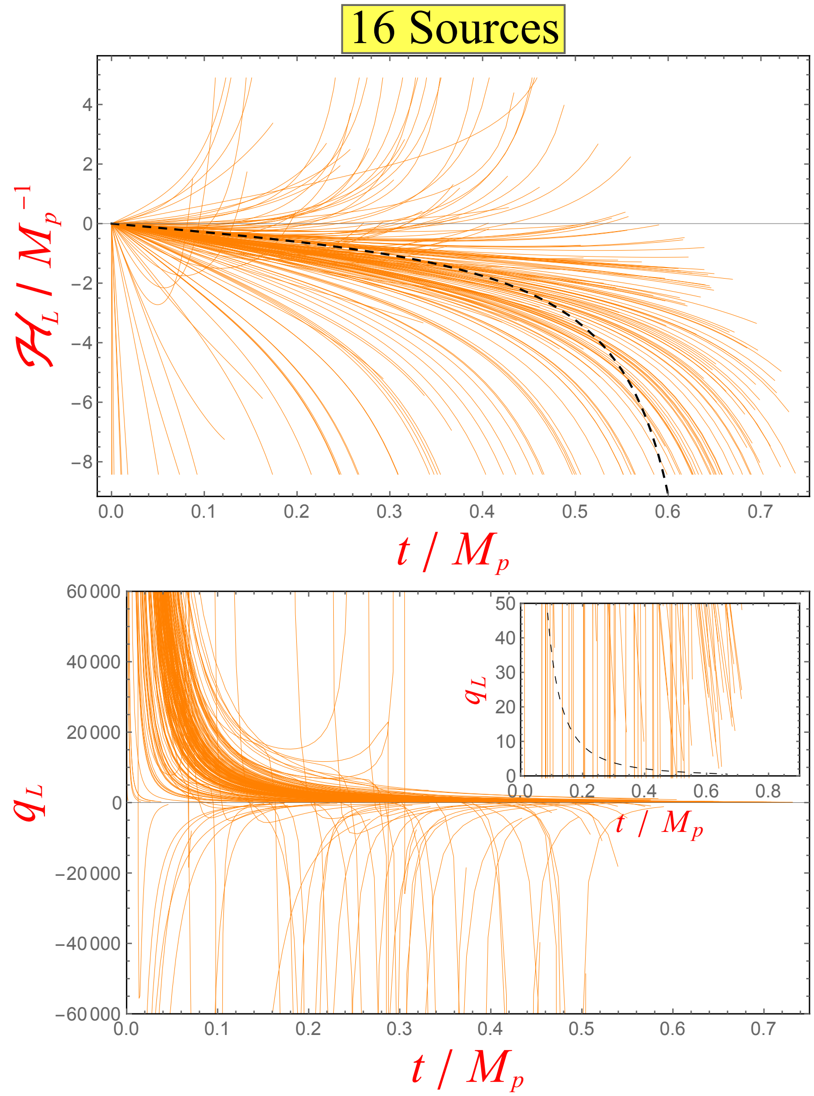

Figure 6.15: Above graphics depict the Hubble parameter (top) and the associated deceleration parameter (bottom) for 16 sources (200 different configurations measured). The black dashed line depicts the FLRW model (shown as an inlay for the deceleration parameter).

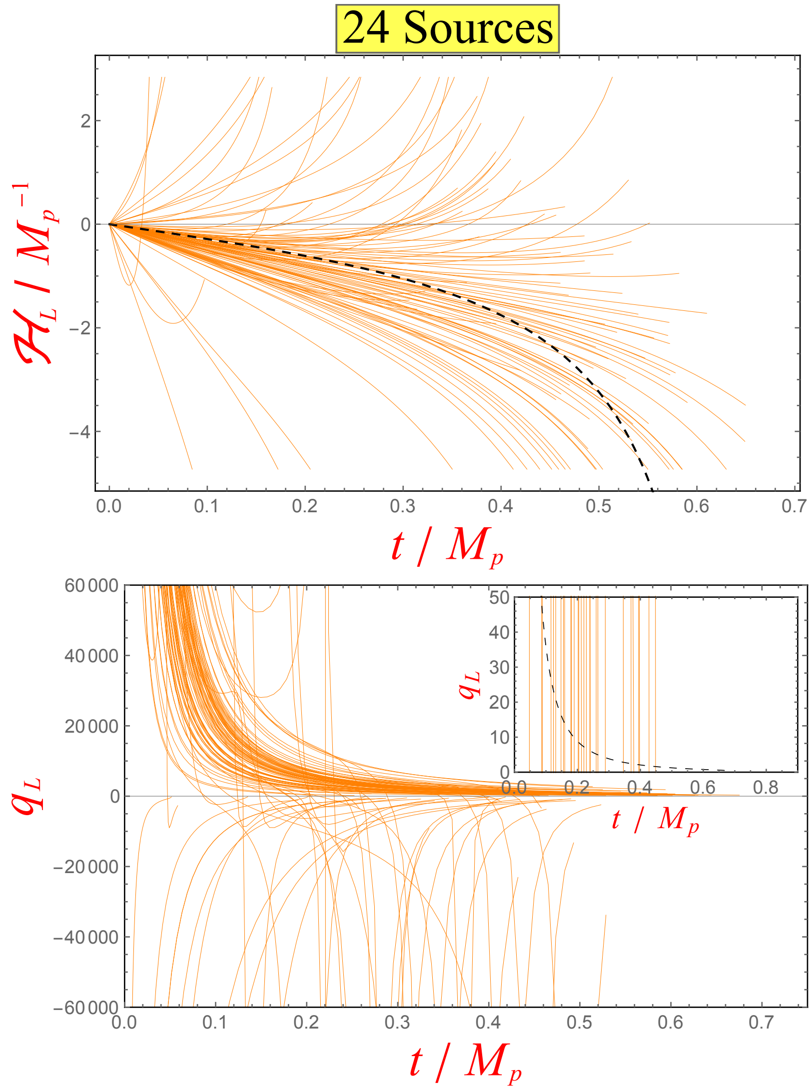

Figure 6.16: Above graphics depict the Hubble parameter (top) and the associated deceleration parameter (bottom) for 24 sources (100 different configurations measured). The black dashed line depicts the FLRW model (shown as an inlay for the deceleration parameter).

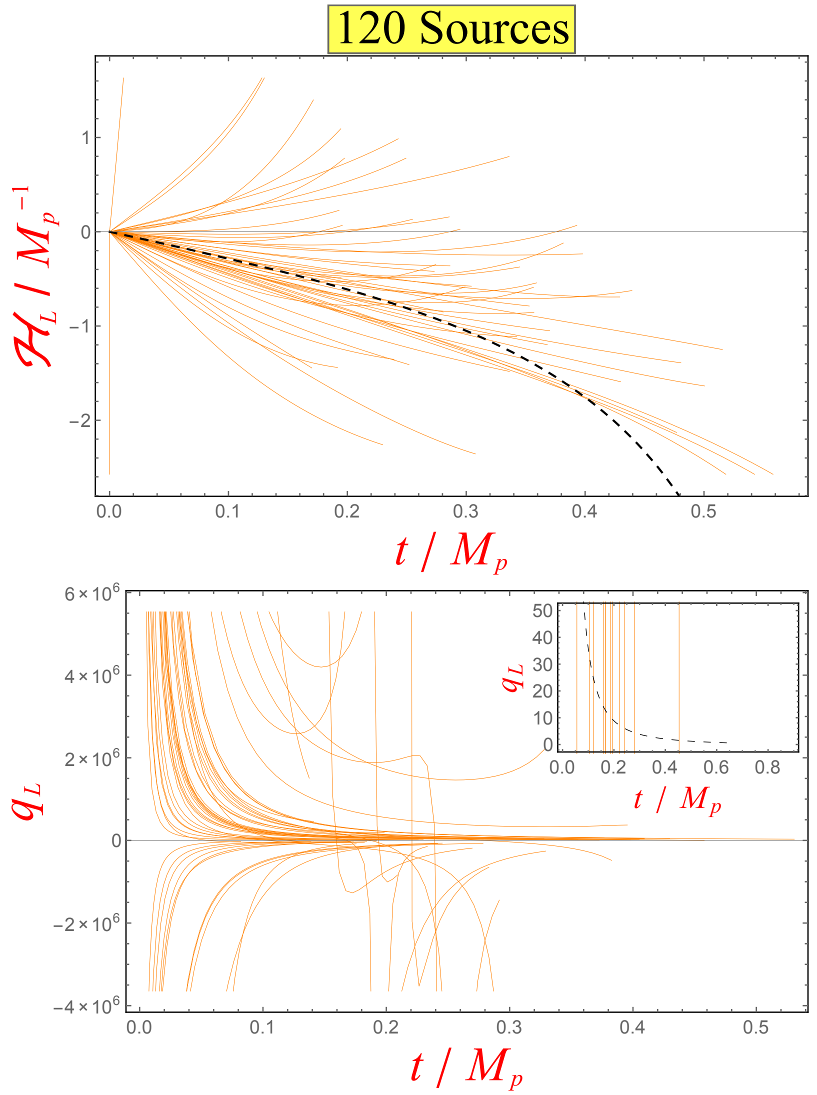

Figure 6.17: Above graphics depict the Hubble parameter (top) and the associated deceleration parameter (bottom) for 120 sources (50 different configurations measured). The black dashed line depicts the FLRW model (shown as an inlay for the deceleration parameter).

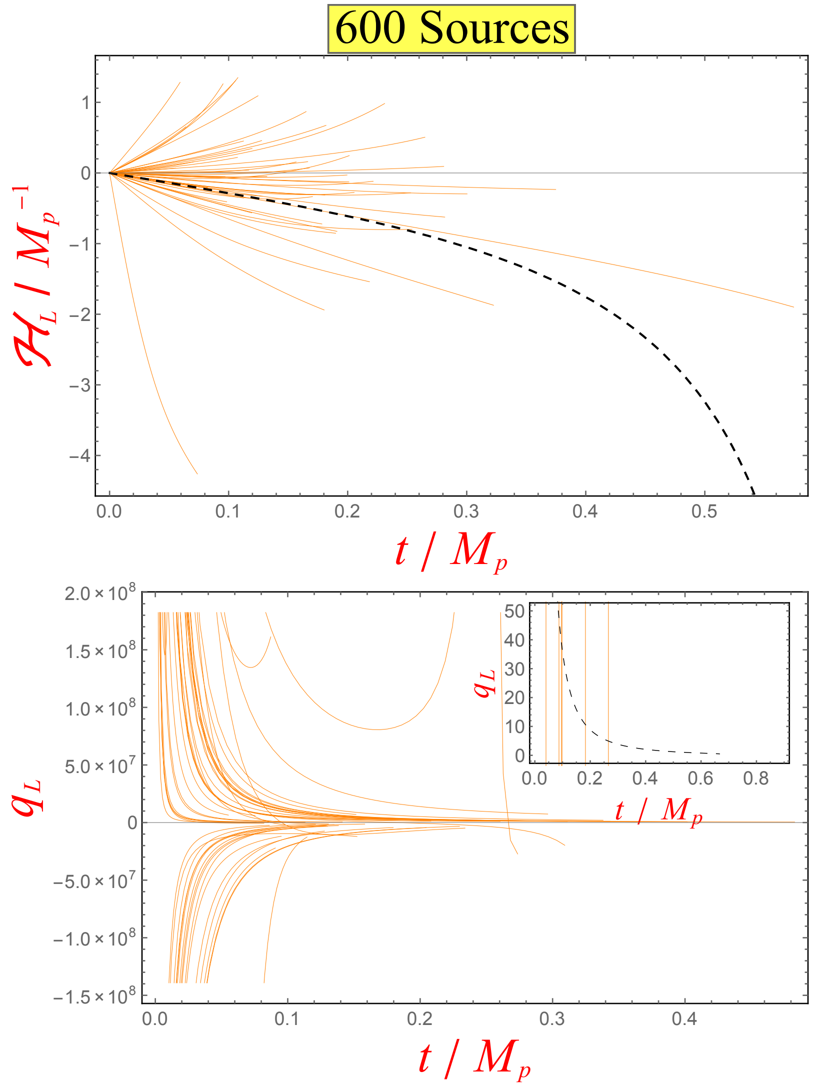

Figure 6.18: Above graphics depict the Hubble parameter (top) and the associated deceleration parameter (bottom) for 600 sources. The black dashed line depicts the FLRW model (shown as an inlay for the deceleration parameter).

Chapter 7

Conclusion

In this thesis the dynamics of discrete irregular (DI models) cosmologies are investigated. The DI model consists of Schwarzschild masses randomly distributed inside vacuum cells which tessellate a 3-sphere. By enforcing that the content of each cell must be reflection symmetric, one can design a model with a high degree of irregularity but at the same time contain a LRS curve. Along this curve the Einstein field equations can be integrated exactly. The curvature, length, Hubble rate and deceleration parameter along the LRS curve is then measured as a function of time.

We have seen that the models give rise to a lot of variety in the initial conditions. The initial LRS curve length, proper mass distribution of the sources and initial curvature greatly varies, even for models containing the same number of sources. The models also exhibit unique characteristics compared to their regular counterparts. However as the number of sources increases; the LRS length and the proper mass approach the homogenous and isotropic FLRW model as expected.

When the DI models are observed as time develops, interesting traits appear. The models behave only similarly to the FLRW model initially. After a brief time period, the behavior can radically change. For many configurations, the length of the LRS curve accelerates! In FLRW cosmology this requires exotic matter, while in the DI model there is only ordinary matter present in the shape of discrete sources in different configurations. This suggests that inhomogeneities have an influence on large-scale geometry.

To obtain more conclusive evidence, the DI models need to be more thoroughly investigated by looking at individual configurations. The aim would then be to determine what traits in the configurations would result in a contraction or expansion. This would be greatly simplified if one could manipulate the proper masses more directly, for instance by setting the proper mass constant and equal for all sources and allow the effective mass to vary instead.

Another avenue to pursue would be to introduce more realism into the models. However one issue needs to be clarified first; it is related to the number of cells in the DI model. Comparisons between the four-cell and eight-cell DI model indicate that the four-cell model approaches the FLRW model better. To ascertain this, one would have to investigate DI models with more cells and see whether fewer cells approach the FLRW model better. Furthermore, the time evolution for the four-cell and other cell counts needs to be performed and compared. Thereafter the cell count which produces the more realistic initial conditions could be chosen, determined by observations.

Further realism can thereafter be introduced by implementing structure. In our present universe, matter is rarely found alone but cluster together to form vast structures. Implementing structure in each individual cell is perhaps the best method of approach and could yield interesting results.

Another question these models raise is, what happens to the masses with time? The method herein allow only for measurements of dynamics along the LRS curve, everywhere else requires more cumbersome mathematics and numerical approaches. It would be interesting to see how the source configurations changes with time, and how would this affect the proper mass?

Acknowledgments

This marks the end of a very long journey lasting about five years - a highly rewarding and challenging journey. Even if this thesis took only a fifth of that time to write, many of the past skills acquired have been put to use herein. Thus I consider this thesis to be the culmination of my five years of studies at Stockholm University. Writing this was difficult, yet rewarding; I am very proud of what it turned into. In addition, like most journeys, I have had the honor to meet incredible teachers and students along the way. I would like to extend my gratitude to all of them. More specifically, this thesis could not have come to pass without the aid of certain people. I wish to mention a few of them here.

I am first and foremost very grateful toward my teacher and supervisor Kjell Rosquist for all his effort, support and patience. None of this would have come to pass without him.

I would also like to thank Timothy Clifton for sending some of his data for use by me. Tensor calculations were performed using RGTC software for Mathematica and therefore I would like to thank the author of the software as well.

On a personal level I would like to extend my gratitude toward my family and friends for their constant avid support and encouragement!

Bibliography

[1] *A Dictionary of Physics*, 5th ed., edited by J. Daintith, Oxford University Press (2005).

[2] C. W. Misner, K. S. Thorne, and J. A. Wheeler, *Gravitation*, W. H. Freeman and Company (1973).

[3] R. W. Lindquist, and J. A. Wheeler, *Rev. Mod. Phys.* **29**, 432 (1957); **31**, 839(E) (1957).

[4] L. Bergström and A. Goobar, *Cosmology and Particle Astrophysics*, 2nd ed., Praxis Publishing, Ltd (2006).

[5] P. Coles and F. Lucchin, *Cosmology - The Origin and Evolution of Cosmic Structure*, 2nd ed., John Wiley & Sons, Ltd (2002).

[6] T. Clifton, K. Rosquist, and R. Tavakol, *Phys. Rev. D.* **86**, 043506 (2012).

[7] H. Engström, *Properties of Mass Distributions for Discrete Cosmology*, Master Thesis, Stockholm University, Stockholm (2013).

[8] E. Bentivegna and M. Korzyński, *Class. Quant. Grav.* **29**, 165007 (2012).

[9] T. Clifton, D. Gregoris, K. Rosquist, and R. Tavakol, *J. Cosmol. Astropart. Phys.*, **11**, 010, (2013).

[10] L. D. Landau, and E. M. Lifshitz, *The Classical Theory of Fields* - vol. 2, 4th ed., Butterworth-Heinemann (1975).

[11] H. van Elst, and C. Uggla, *Class. Quant. Grav.* **14**, 2673 (1997).

[12] E. Poisson, *A Relativist's Toolkit*, Cambridge University Press (2004).

[13] B. Schutz, *A First Course in General Relativity*, 2nd ed., Cambridge University Press (2009).

[14] J. Plebanski, and A. Krasinski, *Introduction to General Relativity and Cosmology*, Cambridge University Press (2006).

[15] D. Hilbert, and S. Cohn-Vossen, *Geometry and the Imagination*, 2nd ed., Chelsea Publishing Company (1990).

[16] S. W. Hawking, and G. F. R. Ellis, *The Large Scale Structure of Space-Time*, Cambridge University Press (1973).

[17] R. Maartens, and B. A. Bassett, *Class. Quant. Grav.* **15**, 705-717 (1998).

[18] G. F. R. Ellis, *J. Math. Phys.* **8**, 1171 (1967).

[19] P. Szekeres, *A Course in Modern Mathematical Physics - Groups, Hilbert Space and DIfferential Geometry*, Cambridge University Press (2004).

[20] E. W. Weisstein, "Sphere Point Picking", *MathWorld - A Wolfram Web Resource*, http://mathworld.wolfram.com/SpherePointPicking.html (accessed October 26, 2014).

[21] G. Marsaglia, *Ann. Math. Statist.* **43**, No. 2, 645-646 (1972).

[22] E. W. Weisstein, "Hypersphere Point Picking", *MathWorld - A Wolfram Web Resource*, http://mathworld.wolfram.com/HyperspherePointPicking.html (accessed February 15, 2014).

[23] D. R. Brill, and R. W. Lindquist, *Phys. Rev.* **131**, 471 (1963).